INTEGRAL EQUATIONS IN COMPUTATIONAL ELECTROMAGNETICS: FORMULATIONS, PROPERTIES AND ISOGEOMETRIC ANALYSIS

By

Jie Li

A DISSERTATION

Submitted to
Michigan State University
in partial fulfillment of the requirements
for the degree of

Electrical Engineering – Doctor of Philosophy

2018

ABSTRACT

INTEGRAL EQUATIONS IN COMPUTATIONAL ELECTROMAGNETICS: FORMULATIONS, PROPERTIES AND ISOGEOMETRIC ANALYSIS

By

Jie Li

Computational electromagnetics (CEM) provides numerical methods to simulate electromagnetic waves interacting with its environment. Boundary integral equation (BIE) based methods, that solve the Maxwell's equations in the homogeneous or piecewise homogeneous medium, are both efficient and accurate, especially for scattering and radiation problems. Development and analysis electromagnetic BIEs has been a very active topic in CEM research. Indeed, there are still many open problems that need to be addressed or further studied. A short and important list includes (1) closed-form or quasi-analytical solutions to time-domain integral equations, (2) catastrophic cancellations at low frequencies, (3) ill-conditioning due to high mesh density, multi-scale discretization, and growing electrical size, and (4) lack of flexibility due to re-meshing when increasing number of forward numerical simulations are involved in the electromagnetic design process. This dissertation will address those several aspects of boundary integral equations in computational electromagnetics.

The first contribution of the dissertation is to construct quasi-analytical solutions to time-dependent boundary integral equations using a direct approach. Direct inverse Fourier transform of the time-harmonic solutions is not stable due to the non-existence of the inverse Fourier transform of spherical Hankel functions. Using new addition theorems for the time-domain Green's function and dyadic Green's functions, time-domain integral equations governing transient scattering problems of spherical objects are solved directly and stably for the first time. Additional, the direct time-dependent solutions, together with the newly proposed time-domain dyadic Green's functions, can enrich the time-domain spherical multipole theory.

The second contribution is to create a novel method of moments (MoM) framework to solve electromagnetic boundary integral equation on subdivision surfaces. The aim is to avoid the meshing and re-meshing stages to accelerate the design process when the geometry needs to be updated. Two schemes to construct basis functions on the subdivision surface have been explored. One is to use the div-conforming basis function, and the other one is to create a rigorous iso-geometric approach based on the subdivision basis function with better smoothness properties. This new framework provides us better accuracy, more stability and high flexibility.

The third contribution is a new stable integral equation formulation to avoid catastrophic cancellations due to low-frequency breakdown or dense-mesh breakdown. Many of the conventional integral equations and their associated post-processing operations suffer from numerical catastrophic cancellations, which can lead to ill-conditioning of the linear systems or serious accuracy problems. Examples includes low-frequency breakdown and dense mesh breakdown. Another instability may come from nontrivial null spaces of involving integral operators that might be related with spurious resonance or topology breakdown. This dissertation presents several sets of new boundary integral equations and studies their analytical properties. The first proposed formulation leads to the scalar boundary integral equations where only scalar unknowns are involved. Besides the requirements of gaining more stability and better conditioning in the resulting linear systems, multi-physics simulation is another driving force for new formulations. Scalar and vector potentials (rather than electromagnetic field) based formulation have been studied for this purpose.

Those new contributions focus on different stages of boundary integral equations in an almost independent manner, e.g. isogeometric analysis framework can be used to solve different boundary integral equations, and the time-dependent solutions to integral equations from different formulations can be achieved through the same methodology proposed.

To my family

ACKNOWLEDGEMENTS

First, I would like to give sincere thanks to my advisor Prof. Shanker Balasubramaniam for the continuous guidance, encouragement and financial support. Working with such a great advisor and researcher has always been amazing and rewarding. Without those many fruitful discussions with him, the work in the thesis would not be possible.

Next, I thank Profs. Rothwell, Piermarocchi and Albrecht for serving in my committee. I must also give my thanks to the faculty members in the electomagnetics research group at MSU for developing great EM courses and creating such a flexible research environment. Special thanks should also go to Profs. Piermarocchi and Tong for collaborations on projects during the PhD study.

I owe thanks to group members. I want to thank Dr. Dault for the collaboration and exciting discussions on many topics and ideas. I also appreciate the opportunity to work with Drs. Nair, Meierbachtol, Baczewski and Pray in the same lab. With a special mention of my current graduate fellows Steve Hughey, Connor Glosser, Zane Crawford, Scott O'Connor, Luke Baumann and Abdel Alsnayyan, I'm so thankful to them for support and help in many aspects. Those delightful conversations and fruitful discussions have been always valuable to my graduate life and research. I also thank Xin Fu, Beibei Liu and Rundong Zhao for collaborations on topics in the thesis.

I would like to give my appreciation to lots of people who have supported and helped me in the past 5 years. They are Yiqun Yang, Pedro Nariyoshi, Xiaofeng Zhao, Bin Fan, Shichen Zhang, Qianwei Jiang and Sichao Wang, followed by many others in the MSU community and a long list of family friends in the Greater Lansing area.

Finally, I thank my family for understanding and love. Without the support and encouragement from my parents and sister, I wouldn't be where I am today. Special thanks go to my wife for her sacrifices and continuous love. I feel so grateful to have her with me for these years and to have our remarkable daughters Sophia and Mila.

TABLE OF CONTENTS

LIST O	F TABLES	X
LIST O	F FIGURES	xi
CHAP7 1.1 1.2	Maxwell's Equations and Boundary Conditions Overview of Computational Electromagnetics 1.2.1 Time-domain and Frequency-domain Methods 1.2.2 Differential and Integral Equation-based Methods Topics that are Studied in this Dissertation	1 1 2 3 4 6
2.1 2.2 2.3 2.4 2.5 2.6 2.7	Introduction Problem Statement Formulation 2.3.1 Natural Spatial basis: Vector spherical harmonics 2.3.2 Spherical expansion of Time-domain Dyadic Green's function 2.3.3 Volterra Integral kernels and Reduced Time-domain Integral Equations Time-dependent Debye-Mie series solution Eigen-spectrum analysis of the MOT system Numerical Examples Conclusion	8 8 11 12 13 17 19 21 23 27
3.1 3.2 3.3 3.4 3.5	TER 3 NUMERICAL SOLUTIONS ON HIGHER ORDER GEOMETRY REPRESENTATIONS	32 32 33 37 37 38 38 39
4.1 4.2 4.3	TER 4 ISO-GEOMETRIC ANALYSIS ENHANCED METHOD OF MO-MENTS	41 44 46 46 52 54 55

4.4	Numerical Examples	57
	4.4.1 Accuracy of IGA-MoM	57
	4.4.2 Scattering from Structures at Regular Frequency	58
	4.4.3 Conditioning of iso-geometric System at Low-frequency	60
	4.4.4 Examples with Multi-scale Mesh	61
4.5	Conclusion	61
CHAPT	FER 5 SCALAR INTEGRAL EQUATIONS FOR ELECTROMAGNETICS .	. 73
5.1	Introduction	73
5.2	Formulation	76
	5.2.1 Problem Statement	76
	5.2.2 Charge based Representation	76
	5.2.3 Scalar Electric Field Integral Equation	78
	5.2.4 Scalar Magnetic Field Integral Equation	79
	5.2.5 Combined Integral Equation	80
5.3	Method of Moments Solution Procedure	81
	5.3.1 Iso-geometric Analysis on Subdivision Surface	81
	5.3.2 Scalar Basis Function and Linear System Setup	82
	5.3.3 System Solution	85
5.4	Numerical Examples	85
0.1	5.4.1 Spectral Properties	86
	5.4.2 Numerical Test	89
5.5	Conclusion	91
0.0	Conclusion	51
CHAPT	TER 6 DECOUPLED POTENTIAL BASED FORMULATIONS	94
6.1	Introduction	94
6.2	preliminaries	96
6.3	Representations of the Decoupled Potential	98
	6.3.1 Scalar and Vector Potentials	98
	6.3.2 Representation of Scattering Potential	100
6.4	Decoupled Boundary Conditions	101
	6.4.1 Decoupled Boundary Conditions for the PEC case	101
	6.4.2 Decoupled Boundary Conditions for Dielectric Case	
6.5	Formulation of Decoupled Potential Integral Equations	105
0.0	6.5.1 Scalar Potential Integral Equation (SPIE)	105
	6.5.2 Vector Potential Integral Equation (VPIE)	107
6.6	Analytical Properties	111
0.0	6.6.1 Stability Properties of SPIE	112
	6.6.2 Stability Properties of VPIE	112
6.7	Perfectly Electrical Conductor Case	114
6.8	Numerical Results	
		116
6.9	Conclusion and Future Work	120
APPEN	NDICES	122
	PENDIX A SPHERICAL EXPANSIONS	199

APPENDIX B	BOUNDARY INTEGRAL OPERATORS	126
BIBLIOGRAPHY		127

LIST OF TABLES

Table 4.1:	Rel.	L_2 error	in the r	econstructed	l surface	currents	density	 	 58

LIST OF FIGURES

Figure 2.1:	Time-domain coefficients for mode Ψ^1_3	24
Figure 2.2:	Time-domain coefficients for mode Φ^1_3	25
Figure 2.3:	Frequency-domain coefficients for modes Ψ^1_3 and Φ^1_3 , compared to two curves (denoted by FD-Mie-psi and FD-Mie-phi respectively) with frequency domain Mie seires approach.	26
Figure 2.4:	Time-domain coefficients for mode Ψ^1_{30}	27
Figure 2.5:	Time-domain coefficients for mode Φ^1_{30}	28
Figure 2.6:	Frequency-domain coefficients for mode Ψ^1_{30} and mode Φ^1_{30} , compared to two curves (denoted by FD-Mie-psi and FD-Mie-phi respectively) with frequency domain Mie seires approach.	29
Figure 2.7:	Late-time stability	30
Figure 2.8:	Eigenvalues of MOT system of (a) kernel 1, (b) kernel 2, (c) kernel 3 and (d) kernel 4	31
Figure 3.1:	Irregular vertex and triangle (a) An irregular triangle (vertex 1 is valence-7), (b)subdivision once	34
Figure 3.2:	Local averaging during refinement	35
Figure 3.3:	Subdivision surface (a) primal mesh , (b) one subdivision, (c) two subdivisions and (d) three subdivisions	36
Figure 3.4:	The parameter domain within an irregular triangle is recursively partitioned into an infinite number of subdomains	37
Figure 3.5:	Convergence of the relative error in far field for the sphere	39
Figure 3.6:	Convergence of the relative error in far field for the torus	40
Figure 4.1:	Scalar basis function associated with a vertex with valence of 8. (a) Basis function, (b) Surface Laplacian of the basis function	48

Figure 4.2:	Basis function associated with a vertex with valence of 8. (a) non-solenoidal type, (b) solenoidal type	51
Figure 4.3:	Magnitude of surface currents density on the sphere: (a) real part and (b) imaginary part	63
Figure 4.4:	Radar cross section of the sphere $(\phi = 0 \text{ cut}) \dots \dots \dots \dots$	64
Figure 4.5:	Pointwise relative error (a) real part, (b) imaginary part with 20484 DoFs	65
Figure 4.6:	Magnitude of surface current density on the truncated cone: (a) real part and (b) imaginary part	66
Figure 4.7:	Radar cross section of the truncated cone ($\phi = 0$ cut)	66
Figure 4.8:	Magnitude of surface current density on the composite structure: (a) real part and (b) imaginary part	67
Figure 4.9:	Radar cross section of the composite structure ($\phi = 90$ cut)	67
Figure 4.10:	Magnitude of surface current density on the air plane model: (a) real part and (b) imaginary part	68
Figure 4.11:	Radar cross section of the air plane model ($\phi = 90$ cut)	69
Figure 4.12:	Condition number at different frequencies	69
Figure 4.13:	Number of GMRES iterations to converge to a tolerance of 1.0×10^{-6} .	70
Figure 4.14:	Number of GMRES iterations to converge to a tolerance of 1.0×10^{-10} .	70
Figure 4.15:	Comparison of RCS data obtained at 1Hz with analytical solutions	71
Figure 4.16:	Multiscale control mesh: (a) the whole mesh and (b) locally refined region	71
Figure 4.17:	Convergence of the iterative solver	72
Figure 5.1:	The support of the scalar basis: two ring of a valence-5 vertex	83
Figure 5.2:	Scalar basis associated with a vertex	84
Figure 5.3:	Condition number versus frequency	87
Figure 5.4:	Eigen-condition number versus frequency	87

Figure 5.5:	Eigenvalues of the system of (a) scalar EFIE, (b) scalar MFIE and (c) scalar CFIE with $\alpha = 0.5/\eta$	88
Figure 5.6:	Singular values of the system of the scalar EFIE, the scalar MFIE and the scalar CFIE with $\alpha=0.5/\eta$	89
Figure 5.7:	Radar cross sections of the sphere	90
Figure 5.8:	Residual of GMRES Iterations, 600Mhz	91
Figure 5.9:	A plane model: real part of the magnitude of the surface current density	92
Figure 5.10:	Residual of GMRES iterations at different frequencies	93
Figure 6.1:	Real and imaginary parts of eigenvalues at 1 Hz	117
Figure 6.2:	Real and imaginary parts of eigenvalues at $1 \times 10^7 \text{ Hz}$	117
Figure 6.3:	Condition number of VPIE formulation versus frequency	118
Figure 6.4:	Condition number of Müller formulation versus frequency	118
Figure 6.5:	Real part of the coefficients for Ψ^1_{30} mode in the tangential component of the electric field	119
Figure 6.6:	Real part of the coefficients for Φ^1_{30} mode in the tangential component of the electric field	119

CHAPTER 1

INTRODUCTION

1.1 Maxwell's Equations and Boundary Conditions

Electromagnetic waves have been very useful in electrical engineering, playing a significant role in improving people's lives, industry technologies and even scientific research. Applications of electromagnetics include communication, radar detection, remote sensing, bio-medical imaging, lithography and so on, covering a wide range of civil and military activities. Engineering with electromagnetic fields involves design and evaluation of complex systems, where modeling interactions between the system and electromagnetic waves is an inevitable step. The electromagnetic theory has developed significantly after the publication of Maxwell's equations. To model the electromagnetic behaviors of devices or systems, Maxwell equations have to solved.

In the three-dimensional space, time-dependent electromagnetic fields satisfy Maxwell's equations,

$$\nabla \times \mathbf{E} = -\frac{\partial \mathbf{B}}{\partial t}$$

$$\nabla \times \mathbf{H} = \mathbf{J} + \frac{\partial \mathbf{D}}{\partial t}$$

$$\nabla \cdot \mathbf{D} = \rho$$

$$\nabla \cdot \mathbf{B} = 0$$
(1.1)

where \mathbf{E} and \mathbf{H} denote electric and magnetic fields respectively; \mathbf{D} and \mathbf{B} denote electric flux and magnetic flux respectively. In Maxwell's equations, electric current density \mathbf{J} and electric charge density \mathbf{J} can be considered as sources distributed in the whole space.

In the presence of material discontinuity, the following boundary conditions, regarding

the field and flux on both sides of the interface, have to be in play.

$$\mathbf{n}_{21} \times (\mathbf{E}_1 - \mathbf{E}_2) = 0$$

$$\mathbf{n}_{21} \times (\mathbf{H}_1 - \mathbf{H}_2) = \mathbf{J}_s$$

$$\mathbf{n}_{21} \cdot (\mathbf{D}_1 - \mathbf{D}_2) = \rho_s$$

$$\mathbf{n}_{21} \cdot (\mathbf{B}_1 - \mathbf{B}_2) = 0$$

$$(1.2)$$

where \mathbf{n}_{21} represents the unit vector normal to the interface, pointing from medium 2 to medium 1, and \mathbf{J}_s and ρ_s denote the surface current density and charge density, representing source terms on the interface of discontinuity. It's noted that they are not the only way to introduce the exciting source, and another possible source could be the incident wave that is distributed in the whole space. The latter is very common in scattering analysis.

After taking Fourier transform on both sides of (1.1), Maxwell's equations in frequency domain can be written as follows.

$$\nabla \times \mathbf{E} = -j\omega \mathbf{B}$$

$$\nabla \times \mathbf{H} = \mathbf{J} + j\omega \mathbf{D}$$

$$\nabla \cdot \mathbf{D} = \rho$$

$$\nabla \cdot \mathbf{B} = 0$$
(1.3)

where the time-harmonic factor $e^{j\omega t}$ is assumed.

For linear medium, especially in narrow-band problems, the frequency-domain or timeharmonic description allows easier discretization, with only spatial variation to be considered at each frequency. This dissertation will mainly work on time-harmonic problems except Chapter 2 where time-dependent problems are solved.

1.2 Overview of Computational Electromagnetics

In modern electrical engineering where the electromagnetic system is involved, computational modeling is almost one inevitable step simply because it's usually more efficient and cost-effective to carry out the evaluation task with the help of high-speed processors.

Electromagnetic modeling is becoming one important component in the computer-aided engineering (CAE) for designing and manufacturing either consumer or industry products. That drives the research of solving Maxwell's equation in a fast computational manner, rather than the experimental measurement approach. The subject of computational electromagnetics is to study how to solve Maxwell's equations, given the characterization of materials, boundary conditions and the excitation information. Depending on the characteristics (geometry, material and excitation) of the problem, there are various approaches available to solve Maxwell's equations.

1.2.1 Time-domain and Frequency-domain Methods

In most real-life electromagnetic problems, solutions to Maxwell's equations are time-dependent. Therefore it seems very natural to solve the equations directly in the time domain. However, for large amount of linear problems, the time-dependent descriptions can be transformed into the frequency domain, where the time-harmonic response is to be sought. That's the reason why two versions of Maxwell's equations given earlier are commonly used.

Time-domain methods discretize the governing equations both temporally and spatially, in a more first-principle sense. Therefore the unknowns are both time and spatial dependent, usually resulting more unknowns than their frequency-domain counterparts. In linear problems, if the studied system's parameters are well characterized for its time-dependence, time-domain methods can produce the transient response which usually contains wide-band information. Time-dependent simulations can be employed for multi-physics problems as well, where non-linearity might show up when governing equations for two physics laws are coupled.

On the other hand, the frequency-domain simulation is the preferable choice for characterizing the frequency-domain response in a narrow-band scenario. One major assumption for this type of methods is that the material parameters can be determined for the interested frequency. In frequency-domain methods, the time-harmonic factor is also implicitly

assumed on both sides of the equation, therefore no temporal discretization is involved at all in the solving process.

It is straightforward that all the full-wave (including both analytical and numerical approaches) and asymptotic methods have both frequency-domain and time-domain versions. Similarly, both differential and integral equation-based methods can be designed in either frequency or time domain.

1.2.2 Differential and Integral Equation-based Methods

In full-wave electromagnetic simulations, one can choose to solve either the original set of coupled Maxwell's equations or the second order curl-curl equation. Typical numerical methods include finite-difference method (FDM) and finite element method (FEM). Methods like FDM and FEM, no matter in time or frequency domain, can be classified as differential equation (DE)-based methods. These methods have the following advantages.

- 1. DE-based methods are more suitable to model very generalized problems, like those with non-uniform materials.
- 2. The resulting discretized linear system is sparse, and the numerical implementation is much easier.
- 3. Significant progress has been made on many theoretical aspects of DE-based methods, such as linear system solver, convergence and error analysis.

Those features usually enable DE-based methods the first choice when modelling tasks are planned. That also explains the fact that commercial codes implementing DE-based methods are available.

On the other hand, disadvantages of DE based methods are listed as follows.

1. Artificial absorbing boundary condition has to be applied to truncate the open domain problem.

- 2. The differential operator is numerically approximated which caused the phenomenon of the numerical dispersion.
- 3. Volume mesh is involved, which explains why they're not very efficient for some scattering problems.

Compared to the fact that DE-based methods discretize the equation in the volume, another type of methods based on boundary integral equations (BIE) only involve discretization on the interfaces between two types of materials. The reduction in the dimensionality usually decreases the number of unknowns for problems have different materials. More importantly, BIE-based methods don't suffer from the numerical dispersion error or need artificial absorbing boundaries. In electromagnetics, classical formulations for BIE include electric field integral equation (EFIE), magnetic field integral equation (MFIE) and their linear combination (combined field integral equation, CFIE). The numerical method to solve those boundary integral equations is called method of moments (MoM), which can be implemented in both time and frequency domain. Surface integral equation has lots of applications in scattering and radiation analysis, where the target domain is piece-wise homogeneous in terms of material properties. Additionally, integral equation can be also used in hybrid methods to model even more complicated systems, or to achieve better performance. Though some people would argue otherwise, the integral equation is more involved than its differential equation counterpart in modeling electromagnetics. Because of the aforementioned reasons, study on integral equations by the community has been always intensive in the past several decades.

It's worth noting that this section by no means serves the goal of giving detailed review on computational electromagnetics. More information on the progress made in the community can be found in the journal of *IEEE transactions on Antennas and Propagation* and similar periodicals. This dissertation will focus on the boundary integral equations. In the next section, main topics and contributions of this dissertation will be briefly introduced.

1.3 Topics that are Studied in this Dissertation

This dissertation will focus on most of the research results during my PhD study. Several important aspects of boundary integral equations are covered, including (1) quasi-analytical time-dependent solutions of scattering and propagation in spherical domains, (2) a novel discretization framework for boundary integral equations that supports efficient design-throughanalysis process, and (3) new formulations for boundary integral equations and their properties.

Chapter 2 presents the progress on the direct time-dependent spherical harmonics analysis in electromagnetics. More than one century ago, analytical time-harmonic solution to scattering problem of spherical objects was first studied. Similar procedure leading to closed-form full wave results in time-domain hasn't been successful for a long time even the frequency-domain Mie series approach was widely used. A detailed review on this topic in the history was given in [1]. With the newly derived closed spherical expansion form of time-domain dyadic Green's functions, direct time-domain modeling of electromagnetic scattering or radiation in the spherical domain is made possible in a quasi-analytical manner. The procedure will be introduced in this chapter, which was published in [2]. The method has been applied for both acoustics and electromagnetics involving different boundary conditions [1–3].

Chapters 3 and 4 are devoted to the development of new numerical discretization schemes of boundary integral equations. In Chapter 3, the subdivision surface, a very good geometry representation scheme in computer graphics, is presented and directly used to construct the method of moments. Div-conforming basis functions are used, which can achieve superconvergence in the far field. Chapter 4 presents a new framework to discretize the electromagnetic integral equations. The iso-geometric analysis framework, which was first proposed to flexibly aid the computer-aided engineering process in structure mechanics, is fully extended and implemented for electromagnetic scattering analysis with the help of subdivision surfaces. This study on iso-geometric analysis on electromagnetic integral equations has not been done before. Materials in Chapter 3 and 4 have been published in [4,5].

In Chapters 5 and 6, two types of new boundary integral equations are formulated to improve the stability. Chapter 5 studies scalar electromagnetic integral equations based on the idea of applying the Helmholtz decomposition and introducing charge densities as the only unknowns. Iso-geometric discretization is implemented without introducing any low-frequency breakdown. Furthermore, the scalar magnetic field integral equation (sMFIE) is even free from the dense-mesh breakdown due to the fact that it is the second kind integral equation. Then in Chapter 6, a totally different formulation of boundary integral equations is presented. The new formulation is based on decoupled scalar and vector potentials, and in another words, the new formulation gives one integral equation for the scalar potential and another one for the vector potential. The work in Chapter 6 extends the existing decoupled potential formulation for perfect electric conductors to dielectric objects, using a direct approach (vs. indirect approach) where the unknowns have the physical meaning. Analytical properties of the resulting integral equations are studied for the spherical object. Numerical examples are given to illustrate the stability for low frequency and high resolution modes (corresponding to dense discretization).

It is worth noting that each subsequent chapter is very independent from each other, because each chapter corresponds to one paper and it has its own detailed literature review, formulation and section of numerical examples. The notation in each chapter also follows its own convention, with quite a few cross references (if any) without even breaking its completeness.

CHAPTER 2

ANALYTICAL SOLUTIONS TO INTEGRAL EQUATIONS

2.1 Introduction

Debye-Mie series solution [6,7] is one of the most useful tools in time-harmonic analysis of electromagnetic (EM) scattering, and has found in extensive use in both optics and electromagnetics [8,9]. Their applications range from fields as diverse as light scattering from small particles [10], to combustion [11], to analysis of antennas [12,13], to weather [14], to validation and calibration computational and measurement setups, to photonics [15], to biological applications [16].

However, analytical solutions to scattering from a sphere only exist in the Fourier domain. Equivalent literature for transient analysis is very sparse. While it is indeed possible to obtain transient scattering response via Fourier transforms, the challenge of obtaining a stable direct transient solution has remained unsolved for several decades. While attempts to arrive at a solution have been made via explicit Fourier transforms [17] of Bessel and Hankel functions, these approaches are highly oscillatory and therefore, unstable. Aside from an intellectual challenge, the development of methods to solve for scattering from sphere can find applications in a number of areas; from scattering from collection of particles to study of non-linear response of gain particles [18], to imaging [19], to dielectric resonator antennas [20], and so on.

While direct time-domain Mie series like solutions for scattering do not exist, there has been extensive interest in developing multipole theory for representations of radiated fields due to spatially bounded sources. Time domain multipole theory has found applications in both acoustics as well as electromagnetics [21–26], with applications that range from radiation due to volumetric sources [27], to near field scanning [28], to near-to-far field transforms [29]. However, multipole representations require higher order derivatives in time.

As a result, there is a paucity of numerical data and the treatment is largely theoretical. This comment does not apply to fast solvers that use a Whittaker representation of the radiated field [30], and there are substantial numerical results in both acoustics [31] and electromagentics [32].

However, compared with the volume of literature on representation of transient fields due to quiescent sources, research on transient scattering analysis using spherical harmonics is somewhat limited. The methods investigated thus far fall into two categories; (i) using inverse Fourier/Laplace transforms of Bessel and Hankel functions within a mode matching framework, and (ii) using a novel representation of the retarded potential Green's function. The first time-domain Mie algorithms were presented for the scalar Helmholtz equation in [17]. It is evident from the work that obtaining a stable algorithm is difficult as the inverse Fourier transform of the spherical Hankel function is a Gagenbauer polynomial that grows as a function of time. The inverse Fourier transform in the work has to be understood in the convolution sense because the actual inverse Fourier transform doesn't exist. A more recent paper examined the causes of instability, errors in the extent literature, and presented a recursive convolution approach that is stable for both late time and high order harmonics for scalar fields [33]. Extension of classical Fourier methods to electromagnetic fields is significantly more complicated [34], and given the instability for scalar fields, it is not clear that this will be stable for vector fields. It is possible that the method developed in [33] may be extended to the vector case. The second method for solving scattering from spheres was developed before [33], but took an entirely different approach [3]. The underlying thesis of this approach was to utilize the fact that if the trace of quantities of interest were to be represented in terms of tesseral harmonics, then the solution of an integral equation composed of these trace quantities would yield the Mie solution. This statement can be readily proven in the frequency domain [35], and the proofs arise from a spherical harmonic representation of the Green's function. In time domain, this would translate to a representation of the retarded potential Green's functions, which would bring us back the original set of difficulties. In [3], we proposed a novel representation of the Green's function that obviates these difficulties, and produces stable and convergent results.

The work presented herein would follow in the vein of [3] and leverage time domain integral equation (TDIE) methods to develop a quasi-analytical solution to time dependent EM scattering from a sphere. The approach presented is based on vector spherical harmonics expansion for the time-dependent dyadic Green's function (to be more specific, its tangential trace) of both electric and magnetic field types, and integrated the results presented in [3]. The use of tesseral harmonics for representing the spatial variation of the trace quantities on the surface of the sphere permits (i) a mesh free solution and (ii) analytical evaluation of the integral required for the TDIE, leaving only a Volterra integral in time. The specific contributions of the chapter are as follows: We

- present a stable spherical expansion for time domain dyadic Green's functions of both electric and magnetic types.
- present a spatially mesh-less and singularity-free integral equations for EM scattering from spherical objects
- develop a set of reduced 1-D Volterra integral kernels that are solved with a higher order Galerkin scheme
- present several results demonstrating the accuracy, convergence and stability of the proposed methods.

The remainder of the chapter is organized as follows. Section 2.2 describes the problem to be solved and gives the integral equation with time-domain dyadic Green's function. Section 2.3 derives the vector spherical harmonic expansion for the tangential trace of the time-dependent dyadic Green's function. Section 2.4 gives a brief approach to solve the reduced integral equation to obtain the time-dependent spherical multipoles. Section 2.6 presents a number of results that validate the accuracy, convergence and stability of the presented

method. Finally, we summarize our contribution and outline future research directions in Section 2.7.

2.2 Problem Statement

Consider a perfectly electrically conducting spherical object that occupies a volume $D_1 \subset \mathbb{R}^3$ residing in a homogeneous background medium occupying $D_0 = \mathbb{R}^3 \backslash D_1$, characterized by permittivity ϵ_0 and permeability μ_0 . The boundary of the scatterer is denoted using $\Omega_1 = \partial D_1$, and is equipped with an outward pointing normal $\hat{n}(\mathbf{r})$ and a radius of r = a. On the interface Ω_1 , the tangential electric field vanishes.

The electric field integral equation (EFIE) and magnetic field integral equation (MFIE), their linear combination, can be used to solve the electric current on the surface Ω_1 (usually with spatial meshing). The EFIE and MFIE are usually written as follows, respectively.

$$\mathbf{n} \times \mathbf{n} \times \mathcal{L}(\mathbf{J}(\mathbf{r},t)) = \mathbf{n} \times \mathbf{n} \times \mathbf{E}^{i}(\mathbf{r},t)$$
 (2.1)

$$\mathbf{J}(\mathbf{r},t) + \hat{n} \times \mathcal{K}(\mathbf{J}(\mathbf{r},t)) = \hat{n} \times \mathbf{H}^{i}(\mathbf{r},t)$$
(2.2)

where operators $\mathcal{L}(\cdot)$ and $\mathcal{K}(\cdot)$ are spatial-temporal (four-dimensional) operators associated with dyadic Green's function.

$$\mathcal{L}(\mathbf{X}(\mathbf{r},t)) = \mu \partial_t \int_{S'} \tilde{\mathbf{G}}_{e0}(\mathbf{r},\mathbf{r}') \otimes \mathbf{X}(\mathbf{r},t) dS'$$
(2.3)

$$\mathcal{K}(\mathbf{X}(\mathbf{r},t)) = -\int_{S'} \tilde{\mathbf{G}}_{m0}(\mathbf{r},\mathbf{r}') \otimes \mathbf{X}(\mathbf{r},t) dS'$$
(2.4)

In the above definitions, $\tilde{\mathbf{G}}_{e0}$ and $\tilde{\mathbf{G}}_{m0}$, respectively, denote dyadic Green's functions of electric type and magnetic type in free space. The solutions to the above equations are typically effected using a discrete representation of the scatterer, representing the current using appropriate spatial and temporal basis on this discrete geometric representation and finally, creating a set of linear equations using testing procedures in both space and time. But if the scatterer is spherical/canonical, one can take advantage of the geometry. This is done easily in the frequency domain. In what follows, its transient analogue is presented. First, the

time-dependent Dyadic Green's functions (to be more specific, their tangential traces) are first expanded using vector spherical harmonics. And then the TD-EFIE and TD-MFIE are reduced into a simple Volterra integral equations without any spatial meshing and singularity in the integral kernels. It permits mode-by-mode solutions for coefficients of time-domain Debye-Mie series.

2.3 Formulation

2.3.1 Natural Spatial basis: Vector spherical harmonics

On a sphere, vector spherical harmonics (VSH) form a natural basis set to represent the spatial variation of the current [36,37]. Their relations to spherical harmonics are given as

$$\Psi_n^m(\hat{r}) = \Psi_n^m(\theta, \phi) = \frac{r}{\sqrt{n(n+1)}} \nabla^t Y_n^m(\theta, \phi)$$
 (2.5)

$$\mathbf{\Phi}_n^m(\hat{r}) = \mathbf{\Phi}_n^m(\theta, \phi) = \frac{1}{\sqrt{n(n+1)}} \bar{r} \times \nabla^t Y_n^m(\theta, \phi)$$
 (2.6)

where

$$Y_n^m(\theta, \phi) = \sqrt{\frac{2n+1}{4\pi} \frac{(n-m)!}{(n+m)!}} P_n^m(\cos \theta) e^{jm\phi}$$
 (2.7)

In the above equations, P_n^m is the associated Legendre function of degree n and order m of the mode. VSHs comprise a complete and orthogonal tangential basis set. Therefore, the current on the sphere can be written as

$$\mathbf{J}(\mathbf{r},t) = \sum_{n,m} J_{nm}^{1}(t) \mathbf{\Psi}_{n}^{m}(\theta,\phi) + J_{nm}^{2}(t) \mathbf{\Phi}_{n}^{m}(\theta,\phi)$$
 (2.8)

Given the coefficients of both modes, one can get the scattered electric and magnetic fields using

$$\mathbf{E}^{s}(\mathbf{r},t) = -\mathcal{L}(\mathbf{J}(\mathbf{r}',t)) \tag{2.9}$$

$$\mathbf{H}^{s}(\mathbf{r},t) = -\mathcal{K}(\mathbf{J}(\mathbf{r}',t)) \tag{2.10}$$

The basis here used is different from the basis used as in time-harmonic Debye-Mie series, where the field, rather than the current, is represented using the vector spherical wave

functions (VSWF) with radial dependence [12]. However, we use VSWF next to derive the expansions for the time-dependent dyadic Green's functions in time-domain integral equations.

2.3.2 Spherical expansion of Time-domain Dyadic Green's function

The time-domain dyadic Green's function of electric type is the solution to the following wave equation

$$\nabla \times \nabla \times \tilde{\mathbf{G}}_{e0}(\mathbf{r}, \mathbf{r}', t) - \frac{\partial_t^2}{c^2} \tilde{\mathbf{G}}_{e0}(\mathbf{r}, \mathbf{r}', t) = \tilde{\mathcal{I}}\delta(\mathbf{r} - \mathbf{r}')\delta(t)$$
 (2.11)

and its dyadic form is notionally written as

$$\tilde{\mathbf{G}}_{e0}(\mathbf{r}, \mathbf{r}', t) = (\tilde{I} - c^2 \partial_t^{-2} \nabla \nabla) \frac{\delta(t - \frac{r - r'}{c})}{4\pi R}$$
(2.12)

where ∂_t^{-2} stands for a two-fold integral with respect to time, \tilde{I} is the idempotent, and $\frac{\delta(t-\frac{R}{c})}{4\pi R}$ is retarded potential. As shown later, ∂_t^{-2} is not evaluated explicitly. To glean more insight into the analysis, we start with the frequency domain counterpart of the dyadic Green's function:

$$\tilde{\mathbf{G}}_{e0}(\mathbf{r}, \mathbf{r}', \omega) = \left[\tilde{\mathcal{I}} + \frac{1}{k^2} \nabla \nabla\right] G_0(\mathbf{r}, \mathbf{r}', \omega)$$
(2.13)

where k and ω denote the wavenumber and the angular frequency, respectively. The representation of the dyadic Green's function in spherical coordinates is well known, has been used extensively [35], and reads as

$$\tilde{\mathbf{G}}_{e0}(\mathbf{r}, \mathbf{r}', \omega) = jk \sum_{n,m} \left[\mathbf{N}_{nm}^{(4)}(\mathbf{r}, k) \mathbf{N}_{nm}^{(1)*}(\mathbf{r}', k) + \mathbf{M}_{nm}^{(4)}(\mathbf{r}, k) \mathbf{M}_{nm}^{(1)*}(\mathbf{r}', k) \right]$$

$$(2.14)$$

for $|\mathbf{r}| > |\mathbf{r}'|$. In the above equations, $\mathbf{N}_{nm}^{(p)}(k, \mathbf{r})$ and $\mathbf{M}_{nm}^{(p)}(k, \mathbf{r})$ are the TM^r and TE^r vector spherical wave functions (VSWF) of degree n and order m, respectively. In what follows, we use $r = |\mathbf{r}|$ and $r' = |\mathbf{r}'|$. The explicit expressions for $\mathbf{N}_{nm}^{(m)}(k, \mathbf{r})$ and $\mathbf{M}_{nm}^{(p)}(k, \mathbf{r})$ can be found in the appendix in terms of spherical Bessel $z_n^{(1)}(kr')$ or spherical Hankel functions

 $z_n^{(4)}(kr)$. As one can see from (2.14), the expansion is in terms of angular dependent wave function (angular dependence is integrated with radial dependence at this moment), rather than the vector spherical harmonics. Furthermore, the frequency dependence is sprinkled throughout, and as a result taking an inverse Fourier transform is difficult. In order to fully exploit the orthogonality of VSHs as well as make the expressions more amenable to taking an inverse Fourier transform, it is necessary to recast the Green's function in terms of its tangential trace. This can be effected via the following: Taking the tangential trace of the dyadic Green's function via

$$\tilde{\mathbf{G}}_{e0}^{tt}(\mathbf{r}, \mathbf{r}', \omega) = \hat{r} \times \hat{r} \times \tilde{\mathbf{G}}_{e0}(\mathbf{r}, \mathbf{r}', \omega) \times \hat{r}' \times \hat{r}'$$
(2.15)

yields

$$\tilde{\mathbf{G}}_{e0}^{tt}(\mathbf{r}, \mathbf{r}', \omega) = jk\hat{r} \times \hat{r} \times \sum_{n,m} \left[\mathbf{N}_{nm}^{(4)}(k, \mathbf{r}) \mathbf{N}_{nm}^{(1)*}(k, \mathbf{r}') + \mathbf{M}_{nm}^{(4)}(k, \mathbf{r}) \mathbf{M}_{nm}^{(1)*}(k, \mathbf{r}') \right] \times \hat{r}' \times \hat{r}'$$

$$= jk \sum_{n,m} \left[\frac{\left[krz_n^{(4)}(kr) \right]'}{kr} \frac{\left[kr'z_n^{(1)*}(kr') \right]'}{kr'} \mathbf{\Psi}_{nm}(\hat{r}) \mathbf{\Psi}_{nm}(\hat{r}') + z_n^{(4)}(kr)z_n^{(1)*}(kr') \mathbf{\Phi}_{nm}(\hat{r}) \mathbf{\Phi}_{nm}(\hat{r}') \right]$$
(2.16)

It can be shown that the trace of the Green's function has the following properties when operating on the tangential field X that is defined on a spherical surface:

$$\tilde{\mathbf{G}}_{e0}^{tt}(\mathbf{r}, \mathbf{r}', \omega) \cdot \mathbf{X}(\mathbf{r}') = -\tilde{\mathbf{G}}_{e0}(\mathbf{r}, \mathbf{r}', \omega) \cdot \mathbf{X}(\mathbf{r}')$$
(2.17a)

$$\mathbf{X}(\mathbf{r}) \cdot \tilde{\mathbf{G}}_{e0}^{tt}(\mathbf{r}, \mathbf{r}', \omega) = -\mathbf{X}(\mathbf{r}) \cdot \tilde{\mathbf{G}}_{e0}(\mathbf{r}, \mathbf{r}', \omega)$$
(2.17b)

As a result of these properties, one can use $\tilde{\mathbf{G}}_{e0}^{tt}(\mathbf{r}, \mathbf{r}', \omega)$ instead of $\tilde{\mathbf{G}}_{e0}(\mathbf{r}, \mathbf{r}', \omega)$. This property is valid in both frequency and time domain. As is evident from (2.16), $\tilde{\mathbf{G}}_{e0}^{tt}(\mathbf{r}, \mathbf{r}', \omega)$ is expressed purely in terms of VSHs, and consequently one can exploit the orthogonality of these functions as well as take its inverse Fourier transform. The resulting expressions for

the dyadic Green's function can be written as

$$\tilde{\mathbf{G}}_{e0}^{tt}(\mathbf{r}, \mathbf{r}', t) =
\sum_{n,m} \left[\mathcal{F}^{-1} \left[jk \frac{\left[kr z_{n}^{(4)}(kr) \right]'}{kr} \frac{\left[kr' z_{n}^{(1)*}(kr') \right]'}{kr'} \right] \boldsymbol{\Psi}_{nm}(\hat{r}) \boldsymbol{\Psi}_{nm}(\hat{r}')
+ \mathcal{F}^{-1} \left[jk z_{n}^{(4)}(kr) z_{n}^{(1)*}(kr') \right] \boldsymbol{\Phi}_{nm}(\hat{r}) \boldsymbol{\Phi}_{nm}(\hat{r}') \right]
= \sum_{n,m} \left[I_{n}^{1} \boldsymbol{\Psi}_{nm}(\hat{r}) \boldsymbol{\Psi}_{nm}(\hat{r}') + I_{n}^{2} \boldsymbol{\Phi}_{nm}(\hat{r}) \boldsymbol{\Phi}_{nm}(\hat{r}') \right]$$
(2.18)

It can be shown that I_n^1 in (2.18) can be rewritten as

$$I_n^1 = \frac{c^2 \partial_t^{-2}}{rr'} \partial_r \partial_{r'} \left[rr' \mathcal{F}^{-1} \left[jk z_n^{(4)}(kr) z_n^{(1)*}(kr') \right] \right]$$

$$= \frac{c^2 \partial_t^{-2}}{rr'} \partial_r \partial_{r'} \left[rr' I_n^2 \right]$$
(2.19)

As is evident from (2.18) and (2.19), one needs to obtain the explicit expression for only I_n^2 in order to evaluate an expression of transient electric dyadic Green's function. As is well known, the approach of using the inverse Fourier transforms of spherical Bessel and Hankel functions and then evaluating their convolution is unstable, because the inverse Fourier transform of spherical Hankel function doesn't exist. In the next section, we present an overview of a method that was recently developed to address this very problem [3], and then use this to recover expressions for both the trace of the electric and magnetic dyadic Green's functions.

The starting point for deriving an expression that approximates I_2 or provides an alternative representation arises from examining the representation for the Green's function for the Helmholtz equation, viz.,

$$\frac{\exp\left[-jkR\right]}{4\pi R} = -jk \sum_{n,m} z_n^{(4)}(kr) z_n^{(1)}(kr') Y_n^m(\hat{r}) Y_n^{m*}(\hat{r}')
\frac{\delta(t - R/c)}{4\pi R} = \sum_{n,m} \mathcal{F}^{-1}[-jk z_n^{(4)}(kr) z_n^{(1)}(kr')] Y_n^m(\hat{r}) Y_n^{m*}(\hat{r}')$$
(2.20)

While this is the well known classical representation, an alternate representation may be derived using

$$f(x) = \sum_{n} a_n P_n(x); \quad a_n = \frac{2n+1}{2} \int_{-1}^{1} dx \ f(x) P_n(x)$$
 (2.21)

where $P_n(x)$ is the Legendre function of nth order. Using $x = \cos \gamma = (r^2 + r'^2 - R^2)/(2rr')$ where γ denotes the angle between the points \mathbf{r} and \mathbf{r}' or equivalently $R = \sqrt{r^2 + r'^2 - 2rr'x}$, and $f(x) = \exp[-jkR]/(4\pi R)$, it is trivial to show that

$$\frac{\exp[-jkR]}{4\pi R} = \sum_{n=0}^{\infty} \frac{2n+1}{8\pi r r'} \int_{|r-r'|}^{r+r'} \exp[-jkR] P_n(x) dR$$
 (2.22)

The inverse Fourier transform to the above expression yields

$$\frac{\delta(t - R/c)}{4\pi R} = \sum_{n=0}^{\infty} \frac{(2n+1)c}{8\pi r r'} P_n \left(\frac{\xi}{2rr'}\right) \mathcal{P}_{\alpha\beta}(t) P_n(x)$$

$$= \sum_{n,m} \frac{c}{2\pi r r'} P_n \left(\frac{\xi}{2rr'}\right) \mathcal{P}_{\alpha\beta}(t) Y_n^m(\hat{r}) Y_n^{*m}(\hat{r}')$$
(2.23)

where $\xi = r^2 + r'^2 - c^2 t^2$, $\mathcal{P}_{\alpha\beta}(t)$ is a pulse function (the value is 1 when $t \in [\alpha, \beta]$, and zero otherwise) with $\alpha = |r - r'|/c$ and $\beta = (r + r')/c$. In obtaining these expressions, we have used the addition theorem for Legendre polynomials. Comparing (2.23) to (2.20), it is apparent that I_n^2 takes the form

$$\mathcal{F}^{-1} \left[-jkz_n^{(4)}(kr)z_n^{(1)*}(kr') \right]$$

$$= \frac{c}{2rr'} P_n \left(\frac{\xi}{2rr'} \right) P_{\alpha\beta}(t) \equiv K_n^{(0)}(r, r', t)$$
(2.24)

Using (2.24) together with (2.19), one can obtain the dyadic Green's function of the electric type as follows:

$$\tilde{\mathbf{G}}_{e0}^{tt}(\mathbf{r}, \mathbf{r}', t) = -\sum_{n,m} \left[K_n^{(0)}(r, r', t) \mathbf{\Phi}_{nm}(\hat{r}) \mathbf{\Phi}_{nm}(\hat{r}') + \frac{c^2 \partial_t^{-2}}{rr'} \partial_r \partial_{r'} \left[rr' K_n^{(0)}(r, r', t) \right] \mathbf{\Psi}_{nm}(\hat{r}) \mathbf{\Psi}_{nm}(\hat{r}') \right]$$
(2.25)

Likewise, a similar procedure leads to the representation of the dyadic Green's function of the magnetic field.

$$\tilde{\mathbf{G}}_{m0}^{tt}(\mathbf{r}, \mathbf{r}', t) = \sum_{n,m} \left[\frac{\partial_{r'}}{r'} \left[r' K_n^{(0)}(r, r', t) \right] \boldsymbol{\Psi}_{nm}(\hat{r}) \boldsymbol{\Psi}_{nm}^*(\hat{r}') \right] \\
- \frac{\partial_r}{r} \left[r K_n^{(0)}(r, r', t) \right] \boldsymbol{\Phi}_{nm}(\hat{r}) \boldsymbol{\Phi}_{nm}^*(\hat{r}') \right]$$
(2.26)

Whereas the above expressions are different from those that are used conventionally, their scalar analogues have proven to be both robust (in terms of stability) and accurate.

2.3.3 Volterra Integral kernels and Reduced Time-domain Integral Equations

The expressions for the Green's functions (or its tangential trace) depend only on VSHs, and thanks to (2.16) they can be used instead of the dyadic Green's functions in the expressions for the EFIE and the MFIE. Specifically, it can be shown that by replacing the dyadic Green's function with its tangential trace, one can get the following integral operators;

$$\mathcal{L}^{tt}(\mathbf{X}(\mathbf{r},t)) = -\mu \partial_t \int_{S'} \tilde{\mathbf{G}}_{e0}^{tt}(\mathbf{r},\mathbf{r}') \otimes \mathbf{X}(\mathbf{r},t) dS'$$
(2.27)

$$\mathcal{K}^{tt}(\mathbf{X}(\mathbf{r},t)) = -\int_{S'} \tilde{\mathbf{G}}_{m0}^{tt}(\mathbf{r},\mathbf{r}') \otimes \mathbf{X}(\mathbf{r},t) dS'$$
(2.28)

The above two operators are effectively equivalent to those in (2.1) and (2.2), but permit the choice of vector spherical harmonics as basis functions for the unknown current densities. Using the above equations together with Galerkin testing (that exploits the orthogonality of the VSHs) results in a set of one-dimensional Volterra equations. For the TD-EFIE, we obtain the following.

$$\langle \Psi_{nm}^{*}(\hat{r}), \mathcal{L}(\Psi_{n'm'}(\hat{r}')) \rangle = \langle \Psi_{nm}^{*}(\hat{r}), \mathcal{L}^{tt}(\Psi_{n'm'}(\hat{r}')) \rangle$$

$$= -\frac{\mu c^{2} \partial_{t}^{-1}}{rr'} \partial_{r} \partial_{r'} \left[rr' K_{n}^{(0)}(r, r', t) \right] \delta_{nn'} \delta_{mm'}$$

$$\equiv K_{n}^{(1)}(r, r', t) \delta_{nn'} \delta_{mm'}$$
(2.29a)

$$\langle \Phi_{nm}^{*}(\hat{r}), \mathcal{L}(\Phi_{n'm'}(\hat{r}')) \rangle = \langle \Phi_{nm}^{*}(\hat{r}), \mathcal{L}^{tt}(\Phi_{n'm'}(\hat{r}')) \rangle$$

$$= -\frac{\mu \partial_{t}}{c} \left[K_{n}^{(0)}(r, r', t) \right] \delta_{nn'} \delta_{mm'}$$

$$\equiv K_{n}^{(2)}(r, r', t) \delta_{nn'} \delta_{mm'}$$
(2.29b)

where the functions $K_n^{(1)}$ and $K_n^{(2)}$ are the one-dimensional Volterra integral kernels for Ψ_{nm} and Φ_{nm} , respectively. The off-diagonal elements $\langle \Psi_{nm}^*, \mathcal{L}^{tt}(\Psi_{n'm'}) \rangle$ and $\langle \Phi_{nm}^*, \mathcal{L}^{tt}(\Phi_{n'm'}) \rangle$ are identically zero. These equations can then be used to obtain the requisite Volterra integral equations for each of the two modes as

$$K_n^{(1)}(r, r', t) \otimes J_{nm}^1(t) = \langle \mathbf{\Psi}_{nm}^*(\hat{r}), \mathbf{n} \times \mathbf{n} \times \mathbf{E}^i(\mathbf{r}, t) \rangle$$

$$\equiv f_{nm}^1(t)$$
(2.30a)

$$K_n^{(2)}(r, r', t) \otimes J_{nm}^2(t) = \langle \mathbf{\Phi}_{nm}^*(\hat{r}), \mathbf{n} \times \mathbf{n} \times \mathbf{E}^i(\mathbf{r}, t) \rangle$$

$$\equiv f_{nm}^2(t)$$
(2.30b)

In the above equations, the right-hand-sides are the projection of $\hat{n} \times \mathbf{n} \times \mathbf{E}^{i}(\mathbf{r}, t)$ onto the two VSH basis sets.

A similar procedure can be followed to derive the necessary equations for the TD-MFIE. The Volterra integral kernels $K_n^{(3)}$ and $K_n^{(4)}$ can be defined as follows.

$$<\Psi_{nm}^{*}(\hat{r}), \mathcal{K}(\Psi_{n'm'}(\hat{r}'))> = <\Psi_{nm}^{*}(\hat{r}), \mathcal{K}^{tt}(\Psi_{n'm'}(\hat{r}'))>$$

$$= -\frac{\partial_{r'}}{r'} \left[r' K_{n}^{(0)}(r, r', t) \right]$$

$$\equiv K_{n}^{(3)}(r, r', t) \delta_{nn'} \delta_{mm'}$$
(2.31a)

$$<\Phi_{nm}^{*}(\hat{r}), \mathcal{K}(\Phi_{n'm'}(\hat{r}'))> = <\Phi_{nm}^{*}(\hat{r}), \mathcal{K}^{tt}(\Phi_{n'm'}(\hat{r}'))>$$

$$= \frac{\partial_{r}}{r} \left[rK_{n}^{(0)}(r, r', t) \right]$$

$$\equiv K_{n}^{(4)}(r, r', t)\delta_{nn'}\delta_{mm'}$$
(2.31b)

Using these kernels, the resulting Volterra equations for the TD-MFIE are

$$J_{nm}^{1}(t) + K_{n}^{(3)}(r, r', t) \otimes J_{nm}^{1}(t)$$

$$= \langle \mathbf{\Psi}_{nm}^{*}(\hat{r}), \mathbf{n} \times \mathbf{H}^{i}(\mathbf{r}, t) \rangle \equiv f_{nm}^{3}(t)$$
(2.32a)

$$J_{nm}^{2}(t) + K_{n}^{(4)}(r, r', t) \otimes J_{nm}^{2}(t)$$

$$= \langle \mathbf{\Phi}_{nm}^{*}(\hat{r}), \mathbf{n} \times \mathbf{H}^{i}(\mathbf{r}, t) \rangle \equiv f_{nm}^{4}(t)$$
(2.32b)

Equations (2.30a), (2.30b), (2.32a) and (2.32b) constitute four equations that yield independent coefficients for the current on the surface of the sphere. In some sense, they can be considered a VSH transform of the integral operator. If necessary, one can combine the requisite integrals to form an effective time domain combined field solution as well. That said, it should be noted that the solution to scattering from a sphere has been reduced to solving these two equations that are uncoupled. In what follows, we shall provide a method for solving these equations numerically.

2.4 Time-dependent Debye-Mie series solution

Analytic solution to the above Volterra equations do not exist. As a result, numerical solution to these equations rely on discrete representation of $J_{nm}^1(t)$ and $J_{nm}^2(t)$. Note that, in this section, subscript (nm) for currents, coefficient vectors, right-hand-side vectors and system matrix representations is suppressed. The approach that we follow is to partition the time axis uniformly, and represent basis and test function whose support reside on each time step. The basis functions can be any set of polynomials [38,39], however, we choose Legendre polynomials with support over the time step. This is in contrast to traditional methods [32] wherein basis functions were based on backward looking Lagrange polynomials that span multiple time steps. However, as was shown in [38], using higher order polynomials within a time step results in higher order convergence. Specifically, our representation

$$J^{\xi}(t_i + \tau \Delta_t) = \sum_{j=0}^{N_p} J_{ij}^{\xi} \Pi_i P_j(2\tau - 1); \qquad \tau \in [0, 1)$$
 (2.33)

where $\Pi_i = 1$ for $t \in [t_i, t_{i+1})$, $P_j(\cdot)$ is a Legendre polynomial, $\xi = 1, 2$, and $i = 1 \cdots N_t$ where N_t is the total number of time steps. Using Galerkin testing results in the marching-on-in-time system. In stating the requisite equations, we use a block matrix representation that is indexed by time step as opposed to unknowns, viz.,

$$\mathcal{Z}_0^{\nu} \mathcal{I}_q^{\xi} = \mathcal{V}_q^{\nu} - \sum_{j=j_0}^{q-1} \mathcal{Z}_{q-j}^{\nu} \mathcal{I}_j^{\xi}; \qquad \nu = 1, 2, 3, \text{ or } 4$$
 (2.34)

where $j_0 = max(0, q - N_k)$, q is the time step index ranging from 0 to total number of steps N_t , and N_k is the length of the discrete kernel. Here, $\mathcal{I}_j^{\xi} = \left[J_{j1}^{\xi}, \cdots, J_{jN_p}^{\xi}\right]^T$ are current coefficients for those polynomials associated with time step j. In a similar fashion, \mathcal{Z}_j^{ν} and \mathcal{V}_j^{ν} (the one-index subscript denotes the discretization in time) are ,respectively, discrete system and right-hand-side term at jth time step. At any given time t, the right-hand-side vector can be written as

$$\mathcal{V}_{q}^{\nu} = \left[\left\langle \Pi_{q} P_{1}(\cdot), f^{\nu}(\cdot) \right\rangle, \cdots, \left\langle \Pi_{q} P_{N_{p}}(\cdot), f^{\nu}(\cdot) \right\rangle \right]^{T}$$
(2.35)

and the element of the system matrix can be written as

$$\mathcal{Z}_{pi,qj}^{\nu} = \langle \Pi_p P_i(\cdot), K_n^{(\nu)}(\cdot) \otimes \Pi_q P_j(\cdot) \rangle$$
 (2.36)

In the expressions for vector and matrix elements, the two-index and four-index subscripts denote the discretization in space.

In the above equations, the temporal dependencies of the function follows from their explicit definitions earlier in the Section. It should be noted that $K_n^{(1)}$ has an infinite tail, very similar to that encountered while evaluating the contribution of the scalar potential in regular TD-EFIE [38]. As in [32, 40], introduction of an auxiliary charge ameliorates the computational complexity from $\mathcal{O}(N_t^2)$ to $\mathcal{O}(N_t)$. Introducing an auxiliary charge the MOT system for $K_n^{(1)}$ can be written as

$$\mathcal{Z}_0^I \mathcal{I}_q^1 = \mathcal{V}_q^1 - \sum_{j=j_0}^{q-1} \mathcal{Z}_{q-j}^I \mathcal{I}_j^1 - \mathcal{C}_{j-1}$$
 (2.37)

where $j_0 = max(0, q - N_k)$, N_k is the length of the non-constant part of the discrete kernel $K_n^{(1)}$. The auxiliary charge coefficient is chosen as

$$C_j = C_{j-1} + \sum_{k=k_0}^{j} \mathcal{Z}_{j-k}^{I} \mathcal{I}_k$$
 (2.38)

where $k_0 = \min(0, j - N_k)$. The elements of the modified system (\mathcal{Z}^I) are defined as follows.

$$\mathcal{Z}_k^I = \mathcal{Z}_k^1 - \mathcal{Z}_{k-1}^1 \tag{2.39}$$

Equations (2.34) and (2.37) can be solved for the coefficients in every time step, and of course for each harmonic. On another brief note regarding discretization of these equation; since both testing and source basis functions are pulse functions that are multiplied by a higher order polynomial, it can be shown that the inner product in (2.36) can be equivalently written as a convolution of the kernel $K_n^{(\nu)}$ with an interpolatory polynomial that is higher order with support from $(-\Delta_t, \Delta_t)$ and tested by a delta function. The resulting matrix elements are smooth, well behaved, and causal. More importantly, they do not require anterpolation unlike that used in [3,41]. In what follows, we briefly describe the eigenspectrum analysis [40,42] of the kernels presented for sample harmonics.

2.5 Eigen-spectrum analysis of the MOT system

Analysis of instability of direct Fourier inversion can be attributed to rapid growth of coefficients as elucidated in [33], which also provides a method to overcome this rapid growth. By contrast, this approach results in Volterra integral equations whose kernels, when convolved and tested with temporal basis function, are sufficiently smooth (other than at isolated points that are handled analytically). As alluded to in a series of papers by Brunner (see [39], and refs therein) on using DG like methods for Volterra equations, the smoothness of the resulting kernels assures stability. Next, we examine the stability of the MOT system developed earlier by analyzing the eigen-spectrum of the marching system for different harmonics. We note that this section is provided purely for completeness; the equations provided below are similar to those presented in [40,42] by comparing the similarity of the kernels analyzed herein to those presented in these papers. Specifically, for equations involving $K_n^{(1)}$, the MOT can be rewritten in the following matrix system form

$$\begin{bmatrix} \underline{A}_{11} & \underline{0} \\ \underline{0} & \underline{\mathbb{I}} \end{bmatrix} \underline{I}_{j+1} = \underline{F}_{j+1} - \begin{bmatrix} \underline{B}_{11} & \underline{B}_{12} \\ \underline{B}_{21} & \underline{B}_{21} \end{bmatrix} \underline{I}_{j},$$
(2.40)

where $\underline{I}_j = [I_j^T, \cdots, J_{j-N_k}^T, C_{j-1}^T, \cdots, C_{j-1-N_k}^T]^T$, $\underline{F}_j = [I_j^T, 0, \cdots, 0, 0, \cdots, 0]^T$ (here the superscript T denotes transpose) and $\underline{\mathbb{I}}$ is the identity matrix. The elements in other matrices

can be computed as follows.

$$\underline{B}_{11} = \begin{bmatrix} \begin{bmatrix} \mathcal{Z}_1^I \end{bmatrix} & \begin{bmatrix} \mathcal{Z}_2^I \end{bmatrix} & \dots & \begin{bmatrix} \mathcal{Z}_{N_k}^I \end{bmatrix} \\ \begin{bmatrix} \mathbb{I} \end{bmatrix} & 0 & & \dots \\ 0 & \begin{bmatrix} \mathbb{I} \end{bmatrix} & & \dots \\ & & & & \\ & \ddots & & & \\ & \ddots & & & \\ & \dots & & & \end{bmatrix}, \qquad (2.41b)$$

$$\underline{B}_{21} = \begin{bmatrix} \begin{bmatrix} \mathcal{Z}_{1}^{I} \end{bmatrix} & \begin{bmatrix} \mathcal{Z}_{2}^{I} \end{bmatrix} & \dots & \begin{bmatrix} \mathcal{Z}_{N_{k}}^{I} \end{bmatrix} \\ 0 & 0 & & \dots \\ & & & & \\ & & & & \\ & & & & \\ & & & & \\ & & & & \\ & & & & \\ & & & & \\ & & & & \\ & & & & \\ & & & & \\ & & & & \\ & & \\ & &$$

For systems involving other kernels, the corresponding set of equations are

$$\underline{A}\ \underline{I}_{j} = \underline{F}_{j} - \underline{B}\ \underline{I}_{j-1} \tag{2.42}$$

where $\underline{I}_j = [I_j^T, \dots, J_{j-N_k}^T]^T$, $\underline{F}_j = [I_j^T, 0, \dots, 0]^T$. Compared to the updating equations for the first kernel, only current vectors are considered, and the elements of the matrices A and B can be similarly obtained by changing the corresponding kernels in \underline{A}_{11} and \underline{B}_{11} .

To obtain stability of the marching system, eigen-spectrum analysis should be done for matrix $\underline{A}^{-1}\underline{B}$. And in next section, the results of this analysis are presented for different kernels and harmonics.

2.6 Numerical Examples

The contribution of this work lies in deriving quasi-analytic transient Debye-Mie series via time-domain integral equation and its marching on in time solution. Hence, we provide several examples of using TD-EFIE and TD-MFIE to test the accuracy of the method and to demonstrate the stability of the MOT algorithm. However, to understand the computational complexity of the method, assume that the maximum wavenumber to be modeled is κmax and the radius of the sphere is a. Then the number of degrees of freedom for classical tesselation scales as $N_s = \mathcal{O}(\kappa_{max}^2 a^2)$, and the order of harmonics required $N_h = \mathcal{O}(\kappa_{max} a)$. It follows that the cost of traditional solution scales as $\mathcal{O}(N_t N_s^2)$ and that using the method presented here is $\mathcal{O}(N_t N_h^2)$, where N_t is the number of time steps used in the simulation. In what follows, comparison for a single mode is presented as opposed to their sum. The problem studied here is scattering by a perfectly electrically conducting (PEC) sphere of radius a = 1m. The incident field is a plane wave with a modulated Gaussian profile

$$\mathbf{E}^{i}(\mathbf{r},t) = \hat{x}\cos(2\pi f_{0}t)e^{-(t-\bar{r}\cdot\hat{k}/c-t_{p})^{2}/2\sigma^{2}}$$
(2.43)

where $\hat{k}=\hat{z}$ is the direction of propagation, f_0 is center frequency. In the expression, $\sigma=3/(2\pi B)$ and $t_p=40\sigma$, where B denotes the bandwidth. In all the numerical examples of this section, center frequency of $f_0=0.4 {\rm GHz}$ and bandwidth of $B=0.3 {\rm GHz}$ are chosen.

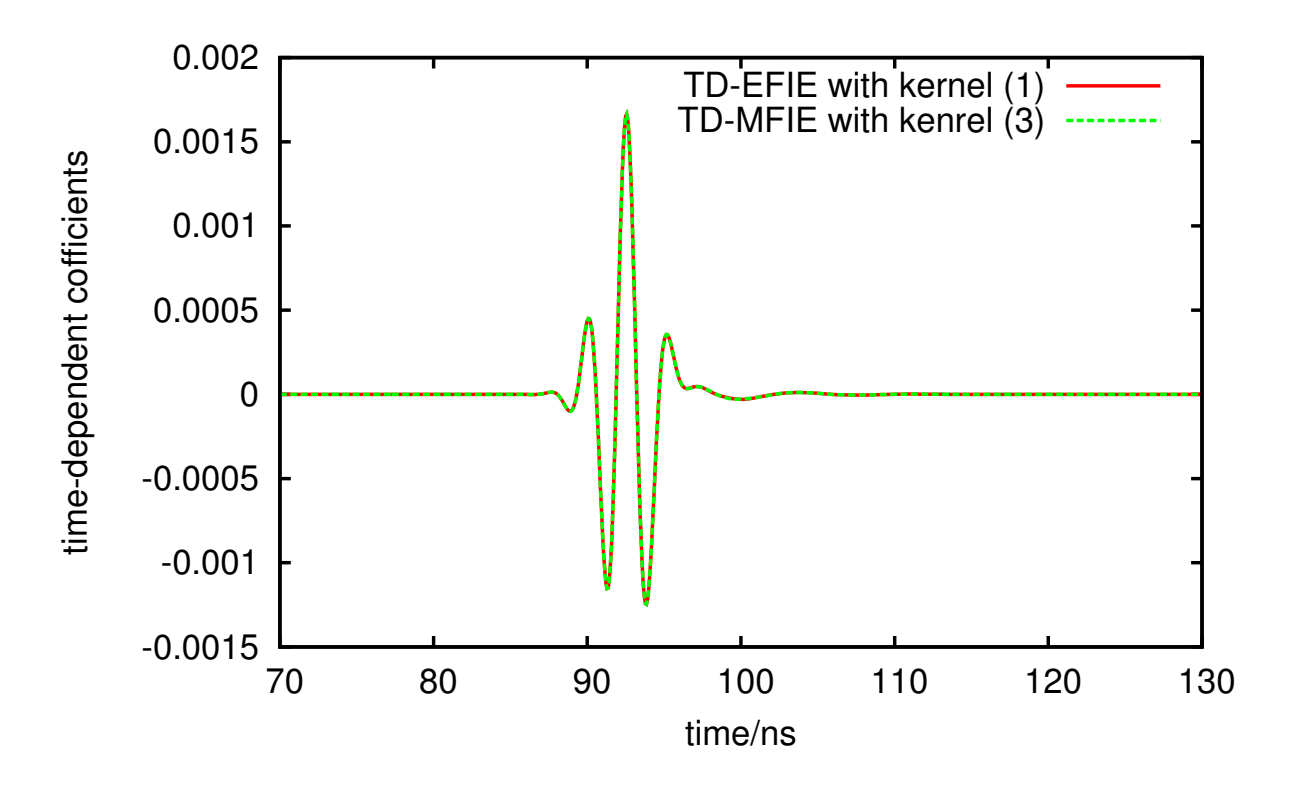


Figure 2.1: Time-domain coefficients for mode Ψ^1_3

With this configuration, the frequency band we are interested in is between 0.1GHz and 0.7GHz. Due to the fact that the power spectral density value at $f_{max} = 0.7$ GHz is 39dB lower than that at the center frequency, the number of spherical harmonics to (spatially) represent the plane wave is bounded by $N_m \approx [2ka] = 30$. In this work, unless specified otherwise, the time step size is chosen as $\Delta_t = \frac{1}{20f_m}$ and the width of the support of temporal basis function is Δ_t .

The first test is to illustrate the accuracy of the proposed method by comparing its frequency-domain counterpart. In this test, the temporal basis function are chosen up to first order Legendre polynomials. The time-dependent coefficients for modes Ψ^1_3 and Φ^1_3 are plotted in Fig. 2.1 and Fig. 2.2. Each plot contains two curves that are obtained using both TD-EFIE and TD-MFIE with corresponding kernels. The comparison in frequency domain within the frequency band is demonstrated in Fig.2.3, and the results from frequency domain

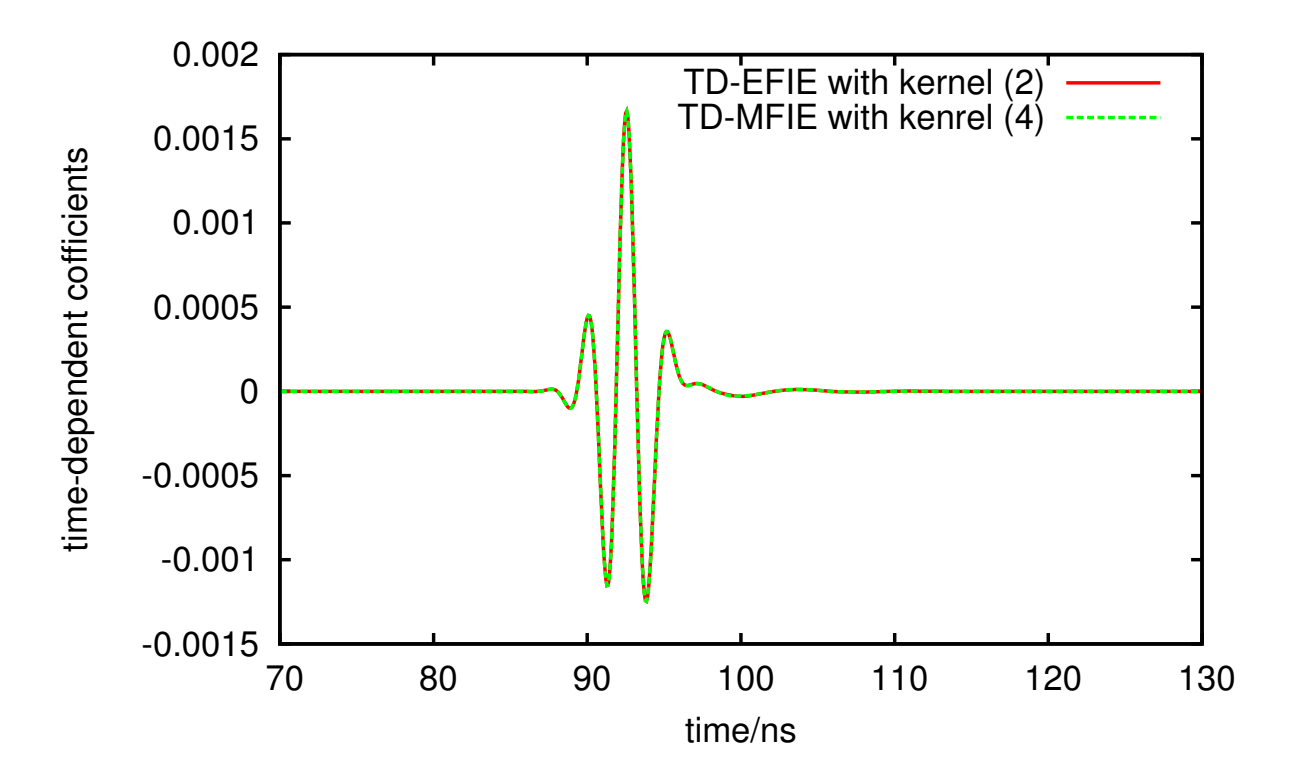


Figure 2.2: Time-domain coefficients for mode Φ_3^1

Mie (FD-Mie) series are also provided to verify the frequency responses. One can observe that the agreement is excellent between time and frequency domain. Similarly conclusion can be drawn for higher order modes. Time-domain and frequency-domain results for modes Φ_{30}^1 and Φ_{30}^1 are given in Figs. 2.4-2.5 and Fig. 2.6, respectively. One can also observe that coefficients for modes of degree 30 are orders of magnitude smaller that those of degree 3. From these results, one can recognize the feasibility of extracting transient response of spherical object with the presented mode by mode MOT approach. In the simulations we conducted, relative error convergence in frequency domain (down to 10^{-12}) versus the order of the temporal basis function (up to 6) has been observed.

The second test is to demonstrate the stability of the marching algorithm. Simulations with two different time steps are carried out for the four reduced Volterra kernels, where the temporal basis functions are chosen up to first order. The solutions are transient coefficients

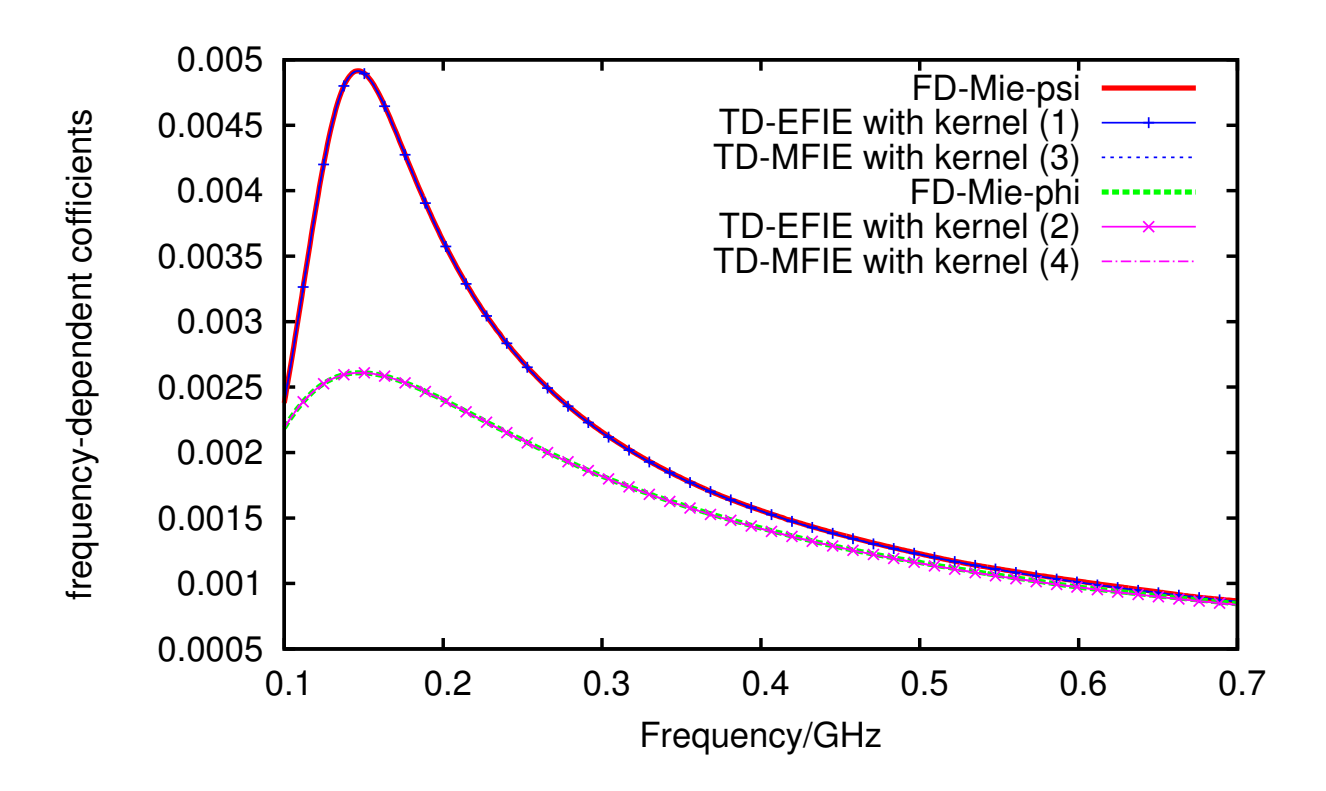


Figure 2.3: Frequency-domain coefficients for modes Ψ^1_3 and Φ^1_3 , compared to two curves (denoted by FD-Mie-psi and FD-Mie-phi respectively) with frequency domain Mie seires approach.

for the modes Ψ^1_{30} (solutions to VIE of kernels 1 and 3) and Φ^1_{30} (solutions to VIE of kernels 2 and 4). Time steps $\Delta_t = \frac{1}{20fm}$ and $\Delta_t = \frac{1}{100fm}$ are chosen (oversampling of 5 and 25 times the Nyquist's sampling rate), and results with 50,000 and 250,000 steps, respectively, are plotted in Fig. 2.7. It's obvious that no late-time instability is observed in these simulations. To further show the stability of the resulting MOT scheme, the eigenvalues analysis of the discretized marching system outlined earlier is given. The real and imaginary parts of the eigenvalues are plotted in Figs. 2.8a-2.8d, with all the values are within the unit circle except one lying on the unit circle which is associated with kernel 1. Similar stability and eigen-analysis results can be also found for simulations with smaller time steps, higher order temporal basis functions and Volterra kernels of different degrees.

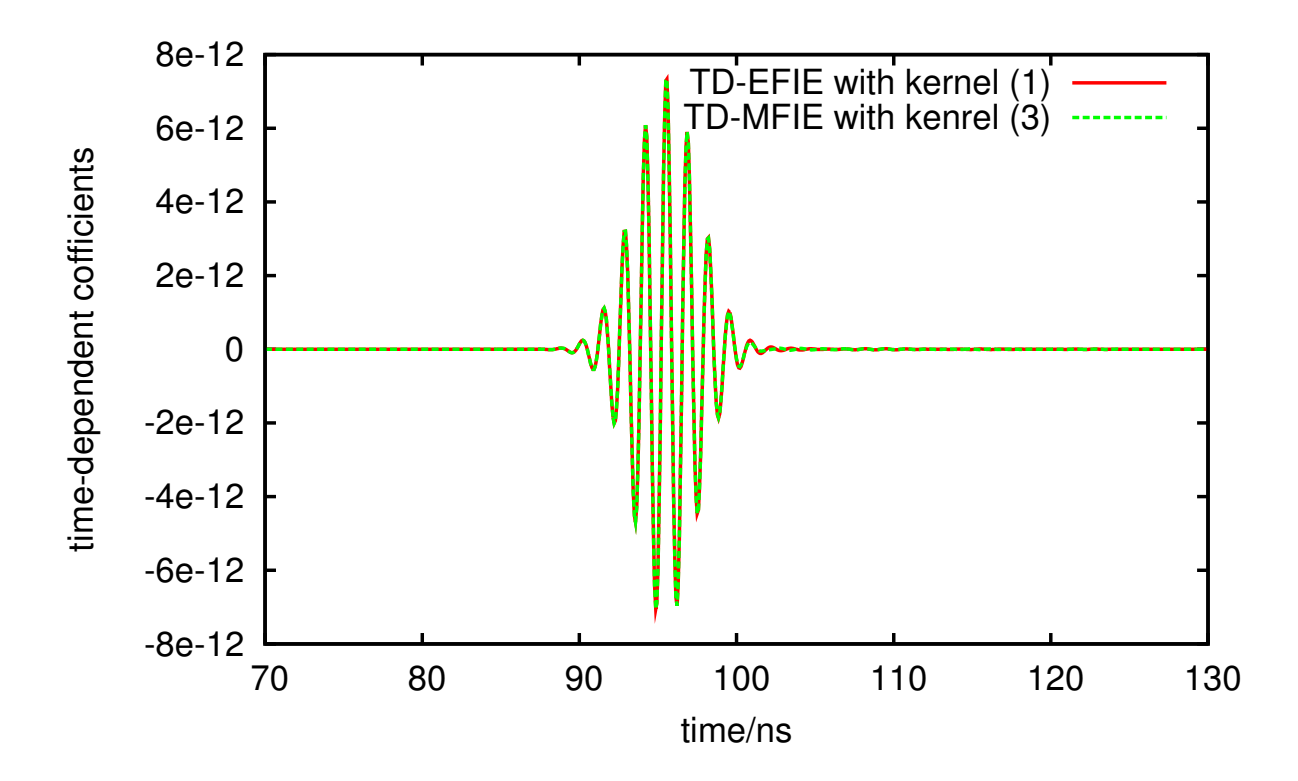


Figure 2.4: Time-domain coefficients for mode Ψ^1_{30}

2.7 Conclusion

In this work, a TDIE-based direct approach is proposed to calculate the time-dependent spherical multipoles due to the scattering by a PEC sphere. By using spherical harmonics as basis functions and expanding the tangential trace of time-domain dyadic Green's function with VSH, the proposed method analytically reduces the original time-domain integral into several novel one-dimensional Volterra integral equations. Those reductions allow very efficient computation for those time-domain spherical multipoles in a marching manner. As shown in the numerical examples, the accuracy and convergence of discretization in time are verified. The resulting kernels could also be considered as good testbeds for various temporal basis function choices and testing schemes. Stability issue arising in conventional TDIE could be studied with those reduced integral equation kernels, which is a current research

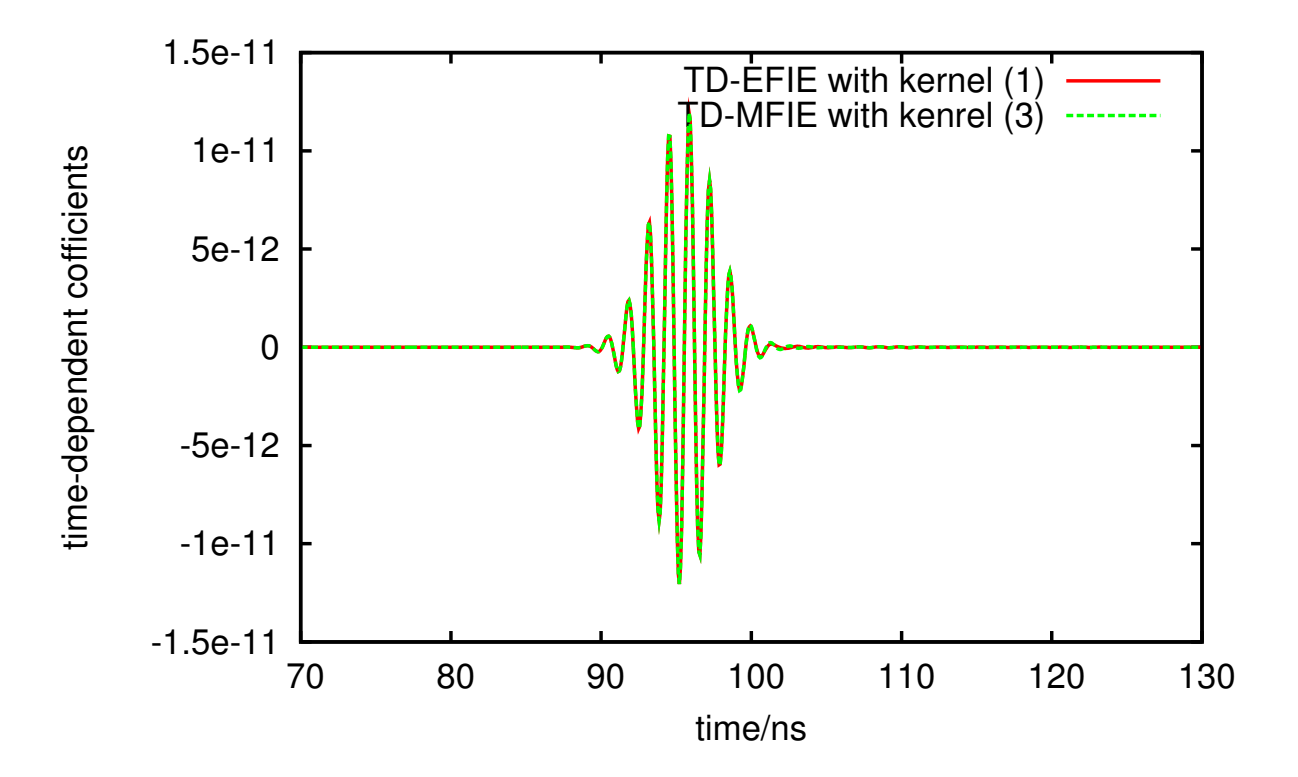


Figure 2.5: Time-domain coefficients for mode Φ_{30}^1

topic.

While the solution presented solves a long standing intellectual problem, it may seem sparse from an application perspective. However, interesting applications exist. For interest, there is a significant interest in developing methods for scattering from clusters of spherical particles that could be accelerated by fast methods [32]. Furthermore, it has many practical applications that its frequency domain counterpart cannot easily handle. First, the method can be used as a local but non-reflecting boundary conditions for time-dependent differential equations based solvers. Second, the proposed time-dependent approach, coupled with other physics-based solvers, can help to model interactions between waves and nonlinear particles. These ideas are currently active topics of research in our group.

This chapter, ©2015 IEEE, is reprinted, with permission, from Li, J. and Shanker, B., "Time-Dependent Debye-Mie Series Solutions for Electromagnetic Scattering," Antennas

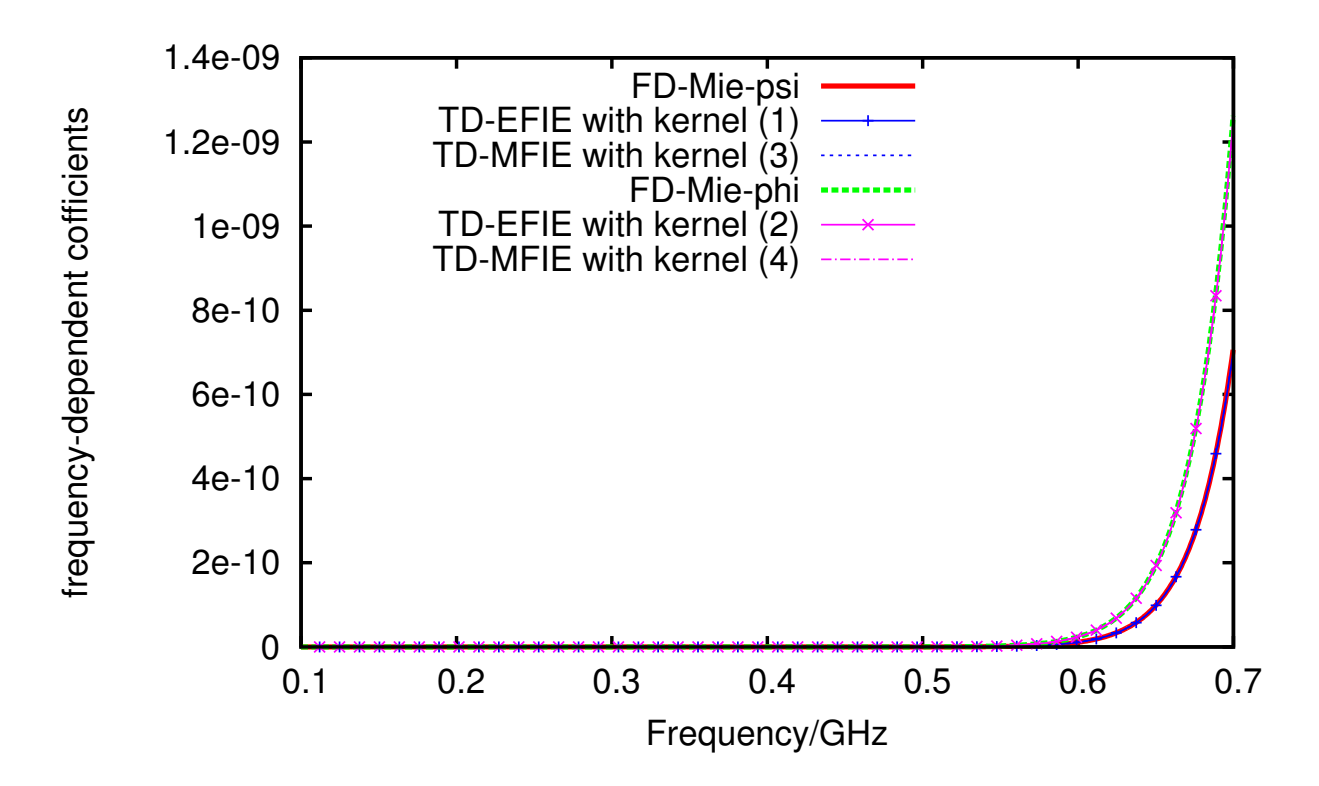


Figure 2.6: Frequency-domain coefficients for mode Ψ^1_{30} and mode Φ^1_{30} , compared to two curves (denoted by FD-Mie-psi and FD-Mie-phi respectively) with frequency domain Mie seires approach.

and Propagation, IEEE Transactions on, August 2015.

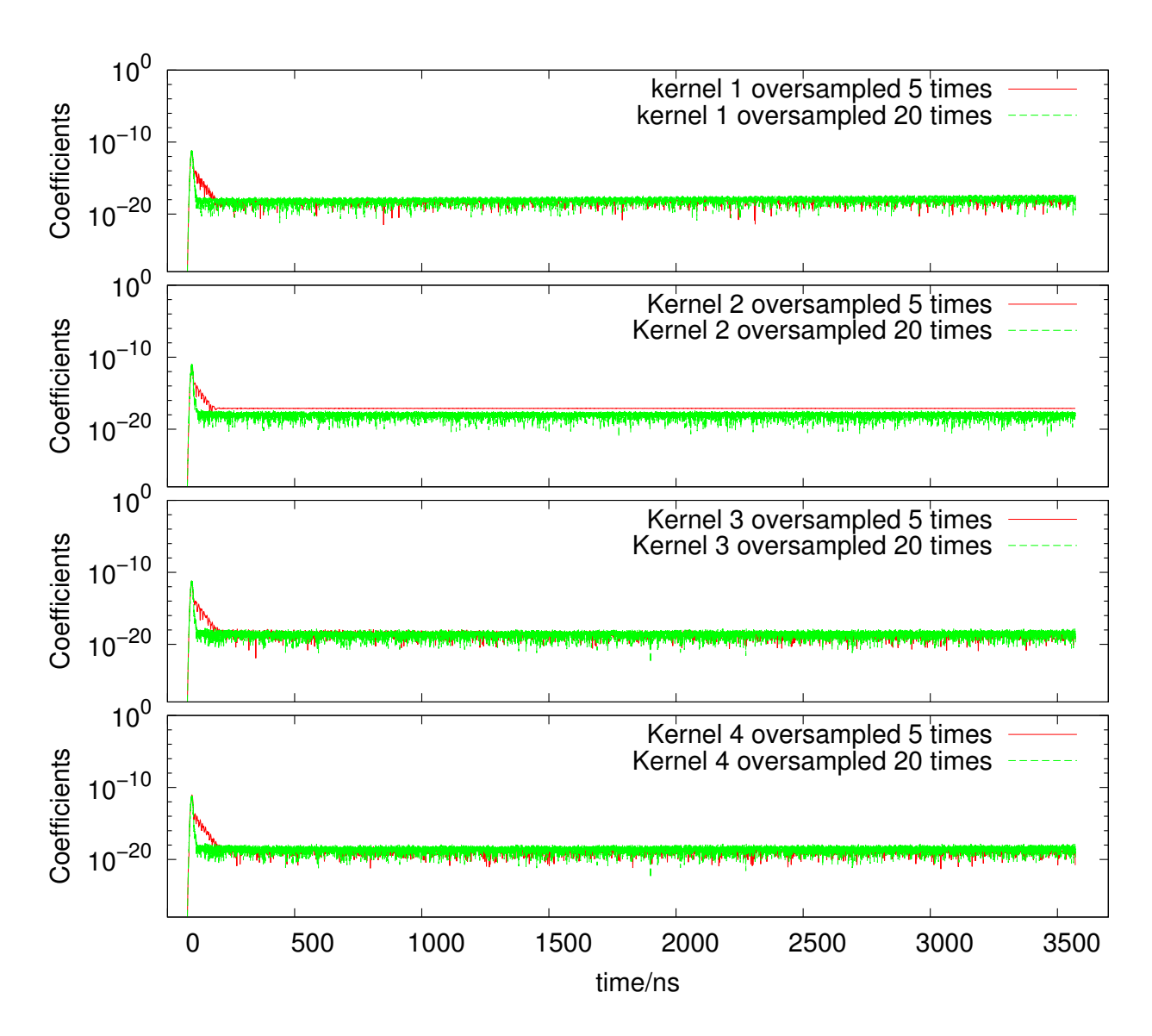


Figure 2.7: Late-time stability

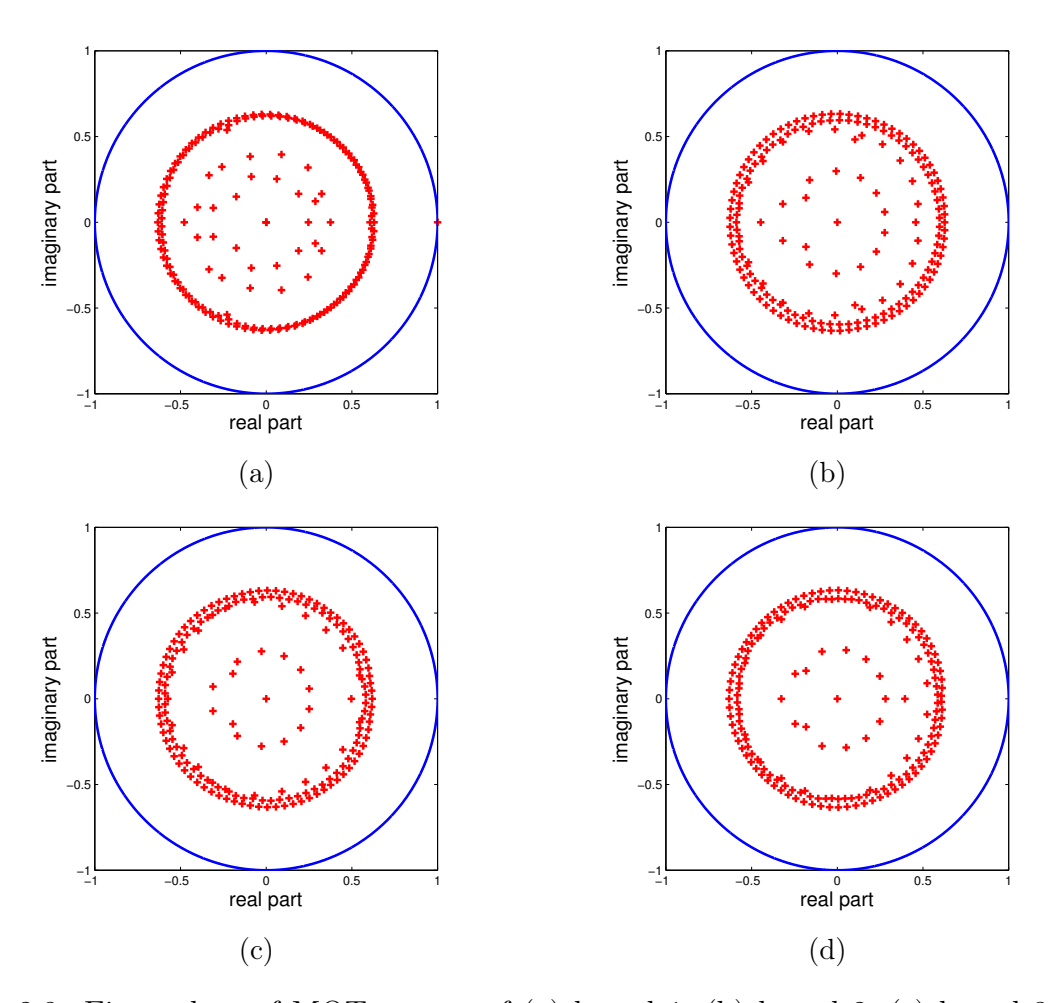


Figure 2.8: Eigenvalues of MOT system of (a) kernel 1, (b) kernel 2, (c) kernel 3 and (d) kernel 4.

CHAPTER 3

NUMERICAL SOLUTIONS ON HIGHER ORDER GEOMETRY REPRESENTATIONS

3.1 Introduction

Surface integral equation has been a very successful tool to analyze the electromagnetic (EM) scattering from homogeneous scatterers. Among them, electric field integral equation (EFIE) and its related forms are widely used. To solve the integral equation on the surface, a geometry representation and a physical quantity (such as the commonly used surface current density) representation are needed. The choice of physical function representation is usually strongly related to the choice of geometric representation. Choosing a good geometry representation is necessary to reduce the numerical error and also helps the construction of basis functions. Typical geometry representation directly employed in method of moments (MoM) is surface mesh, suffering from geometry error because the mesh is reduced from the highly accurate geometry natively defined in computer-aided design (CAD) tools. There are mesh-free methods and more recently isogeometric analysis (IGA) based methods available to at least partly solve the problem [5,43–46]. Furthermore, avoiding geometry representation reduction explicitly can also improve the efficiency of the design-through-analysis process. Isogeometric analysis starts with the original geometry representation format, such as nonuniform rational B-spline (NURBS) surface, subdivision and their modifications, and embeds the native geometry information in the basis design.

Two aspects, at least, of IGA should be developed further for future industry applications; (1) generalization to objects of arbitrary shape and topology and (2) convergence properties of the numerical scheme. Regarding the former, div-conforming basis function defined on curved surfaces, such as curvilinear RWG basis functions should be able to capture all the components in the function space of the current density. [47] shows that optimal convergence

of solutions can be obtained for high order basis functions if geometry representation satisfies certain requirement on the curvature of the cell. In this chapter, the subdivision surface, a powerful geometry representation technique that features high continuity and arbitrary topology, is explored to construct boundary integral equation solvers using the method of moments. Subdivision surface, mostly used in the animation industry, is a smooth geometry representation that can be considered as the limit surface after infinite refinements of primal control mesh. Loop subdivision [48] is one of the commonly used subdivision surface, which will be used in this work. The limit surface of Loop subdivision features C^2 continuity almost everywhere except finite number of isolated irregular vertices. Explicit refinement is not required in practical implementation thanks to the technique proposed by Stam [49]. With that approach, one can evaluate the limit position and up to second order surface differential operators at almost arbitrary points in the parameter domain. Generally, advantages of subdivision surface over other parametric surface like NURBS surface include (1) that it supports global continuity up to C^2 and (2) that it supports control mesh of arbitrary topology and genus (watertight and no gap issue).

This chapter covers the following,

- Isogeometric analysis on smoothly represented structures of arbitrary topology,
- Constructing Div-conforming basis of various orders on subdivision surface,
- Study of super-convergence properties of IGA-MoM.

3.2 Subdivision Surfaces

In what follows, we provide a brief overview of shape description as effected by subdivision surfaces. This section is provided purely for completeness and omits details that can be found in several references, e.g., [48–50]. The traditional workhorse of geometric description is NURBS. As a result, current iso-geometric methods have been largely developed using NURBS as basis functions. However, a singular feature stands out that poses to be a

bottleneck—while NURBS descriptions are C^2 in the interior of a patch, the continuity may be C^0 or even worse (not watertight) at the boundary between patches or at intersection curves. As a result, one has to define physical basis functions that are div- or curl-conforming for vector problems. Specifically, to solve for currents through electric field integral equation, the basis function has to be div-conforming [51–53]. This stands in contrast to subdivision surfaces that are constructed as limit surfaces obtained by subdivision processes. This leads to meshes that are C^2 almost everywhere except at isolated *points* where they are C^1 .

As triangular tessellation is ubiquitous in computational electromagnetics, the choice of the presentation below is based on the Loop subdivision scheme for closed triangular surface mesh. Let M_0 denote the primal base mesh or control mesh that leads to the limit surface. As in any tessellation, M_0 comprises a set of vertices \mathcal{V} and a connectivity map. The 1-ring (union of incident triangles) of a vertex produced by the connectivity map can be characterized by the valence of the vertex; specifically, (i) a valence-6 node/vertex is deemed regular and (ii) any other vertex is called *extraordinary* or *irregular*. A triangle is regular if all its vertices are regular, and irregular otherwise. Fig. 3.1 illustrates an irregular triangle and one subdivision around it.

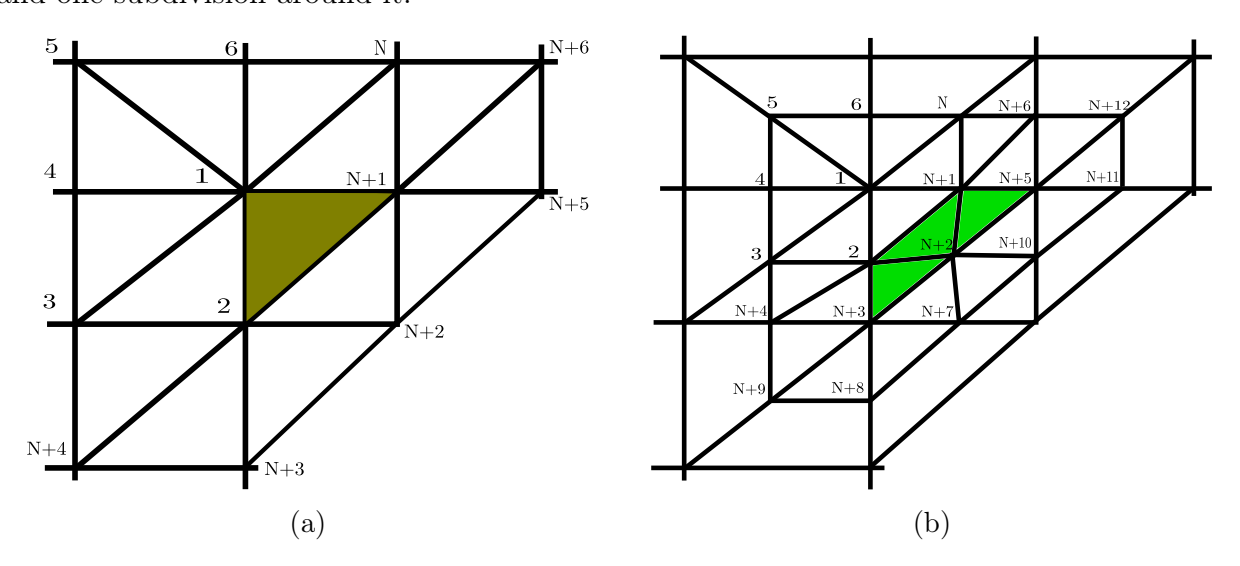


Figure 3.1: Irregular vertex and triangle (a) An irregular triangle (vertex 1 is valence-7), (b)subdivision once

In what follows, we present a high level prescription of Loop subdivision. Loop sub-

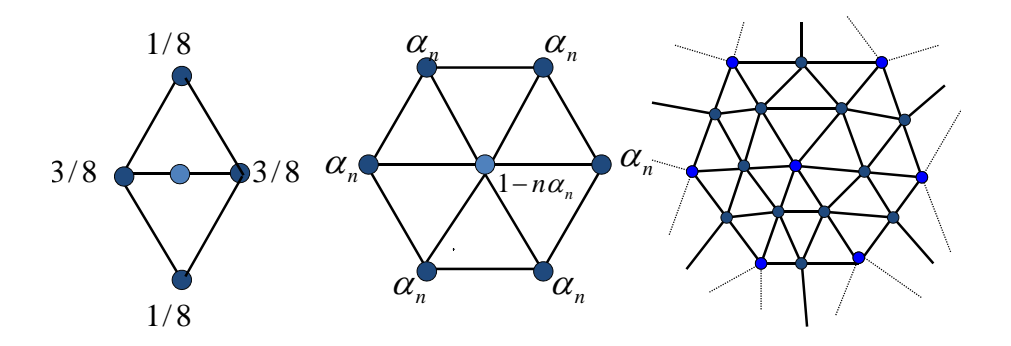


Figure 3.2: Local averaging during refinement.

division prescribes a smooth surface by defining an infinite sequence of meshes that are determined through repeatedly refining the k-th mesh into the (k+1)-th mesh by dividing each triangle into four subtriangles. Each subdivision step involves inserting one vertex per edge and adjusting vertex locations. The location of the newly inserted vertex is an affine combination of the end vertices of the edge, each with weight 3/8, and the other two vertices of the two incident triangles, each with weight 1/8. The location of the existing vertex on the refined mesh is an affine combination of its one-ring vertices with weight $\alpha_n = (5/8 - (3/8 + \cos(2\pi/n)/4)^2)/n$, and itself with weight $1 - n\alpha_n$, where n is the valence. The limit of the sequence of piecewise flat surface is the Loop subdivision surface with C^2 smoothness almost everywhere, except at the extraordinary vertices, where it has C^1 smoothness. Fig. 3.3 gives an example of subdivision surfaces.

In practice, the above prescription is *not* followed, i.e., there is not infinite refinement of meshes. On can alternatively view the surface in terms of basis functions defined at vertices. Consider the a limit surface $\mathbf{S}(u,v) = \sum \mathbf{x}_i \xi_i(u,v)$ that is defined by coordinates \mathbf{x}_i of the vertices V_i ; $\xi_i(u,v)$ is an effective basis function that is associated with quantities associated with vertex V_i , and (u,v) are the pairwise coordinates on a parameterization chart.

In the case of regular vertex, functions $\xi_i(u, v)$ are box-splines. In the case of irregular vertex, $\xi_i(u, v)$ can be constructed by the subdivision procedure starting with 1 assigned to V_i and 0 assigned to all other vertices. The process appears to be, again, not efficient if the evaluation is required at arbitrary location. But one can subdivide k times, instead

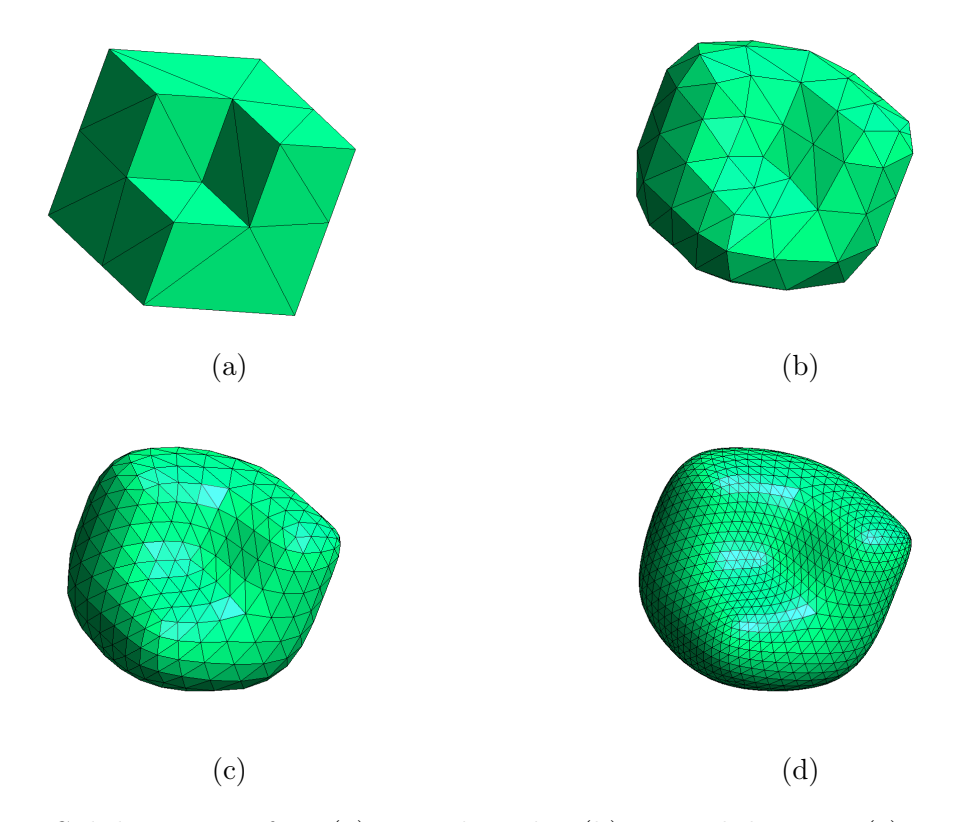


Figure 3.3: Subdivision surface (a) primal mesh, (b) one subdivision, (c) two subdivisions and (d) three subdivisions.

of unlimited times, when the interested location (location referenced by parametric values (u,v)) lies in a sub-triangle (Fig.3.4) with three regular vertices. Then the basis function can be evaluated through linear combinations of box splines with values on the relevant one-ring vertices of the interested sub-triangle. The relevant values for each subtriangle Ω_m^k can be stored in a vector $E_{k,m}$ containing 12 scalars, one for each vertex whose box spline basis function has the triangle in its support. $E_{k,m}$ can be calculated as

$$E_{k,m} = P_m \bar{A} A^k E_0,$$

where E_0 is the initial assignment of the n+6 vertices in Fig. 3.1a, which is 1 for V_l when evaluating ξ_l , and 0 for any other vertex; A is the subdivision operator matrix, an $(n+6)\times(n+6)$ -matrix denoting how the values influencing the irregular triangle in the next level are calculated from the values at the current level (Fig. 3.1b shows the vertex at the next level); \bar{A} is an extended version of A including how the vertices n+7 through n+12 of next

level is computed form the current level; P_m is the picking matrix selecting the relevant 12 values for Ω_m^k within the n+12 values. Note that, in practical implementation, eigenanalysis of A is performed so the evaluation involves taking powers of the eigenvalues as an efficient way of handling the calculation of A^k . Furthermore, the subdominant eigenvectors provide a means for direct evaluation of derivatives even in irregular triangles [49].

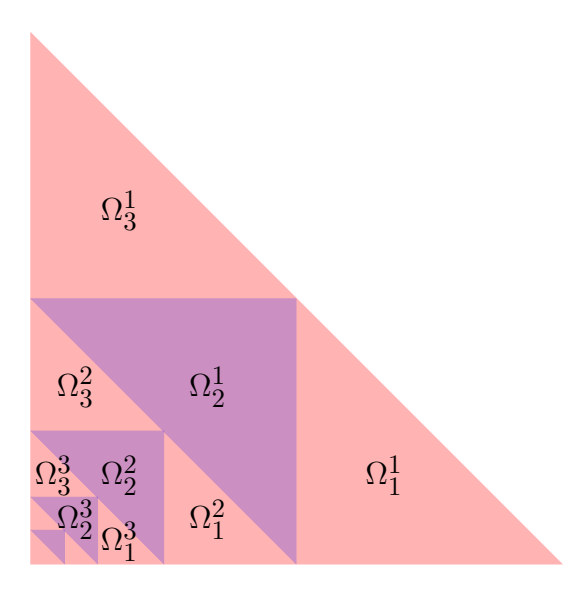


Figure 3.4: The parameter domain within an irregular triangle is recursively partitioned into an infinite number of subdomains.

3.3 Formulation and Discretization

This section will formulate the discrete scheme to solve the integral equation for EM scattering from PEC which is represented by the subdivision surface. Without loss of generality, only EFIE is solved, and extension to uniquely solvable IEs is straightforward. In this chapter, time harmonic factor $e^{j\omega t}$ is implicitly assumed and suppressed.

3.3.1 Integral Equation for PEC

From the equivalence theorem, surface current density $\mathbf{J}(\mathbf{r})$ can be used as the unknown of the EFIE. On the interface, from the boundary condition, one can build the EFIE as follows:

$$\hat{n} \times \hat{n} \times \left(\mathbf{E}^{i}(\mathbf{r}) + \mathbf{E}^{s}(\mathbf{r}) \right) = 0$$
 (3.1)

The scattered field can be represented as

$$\mathbf{E}^{s}(\mathbf{r}) = -j\omega\mu_{0} \int_{\partial\Omega} d\mathbf{r}' \left[\mathcal{I} + \frac{1}{k^{2}} \nabla \nabla \right] g(\mathbf{r}, \mathbf{r}') \cdot \mathbf{J}(\mathbf{r}')$$
(3.2)

The scalar Green's function in free space $g(\mathbf{r}, \mathbf{r}') = \frac{e^{-jk|\mathbf{r}-\mathbf{r}'|}}{4\pi|\mathbf{r}-\mathbf{r}'|}$ where k is the wave number in free space.

3.3.2 Div-conforming Basis on Smooth Subdivision Surface

In [5], C^2 continuous subdivision scalar basis was used to represent the scalar potentials and the current is expanded in the form of the surface gradient and surface vector curl of the potentials. Therefore no global loop component is represented when that scheme is applied to multiply connected structures. To capture that component, one solution is to use edge oriented basis as in RWG basis [52]. Using the Piola transformation, one can construct high order div-conforming basis on the subdivision surface:

$$\mathbf{f}_i(\mathbf{r}) = \frac{DF}{J_s}\bar{\mathbf{f}}(\mathbf{r}) \tag{3.3}$$

where $\bar{\mathbf{f}}(\mathbf{r})$ is the div-conforming basis of any order in the reference domain, DF is the jacobian matrix of the transformation from reference domain to subdivision surface, and J is the jacobian or the determinant of the jacobian matrix. In (3.3), the basis function is embedded with jacobian information of the subdivision surface.

After the basis function is chosen, Galerkin testing is used to set up the linear system which can be solved either directly or through an iterative solver.

3.4 Numerical Examples

In this section, numerical examples are given to demonstrate the convergence and effectiveness of the presented numerical scheme.

The first example is the analysis of scattering from a unit sphere illuminated by the an incidence plane at 100 MHz, where first order basis is used. The convergence in far field

solutions versus the number of degrees of freedom (DoFs) is plotted in Fig. 3.5. The order of the convergence versus the number of DoFs is 1.5, or 3 versus the average size of the control element. This super-convergence behavior in the far-field zone is expected as in [47].

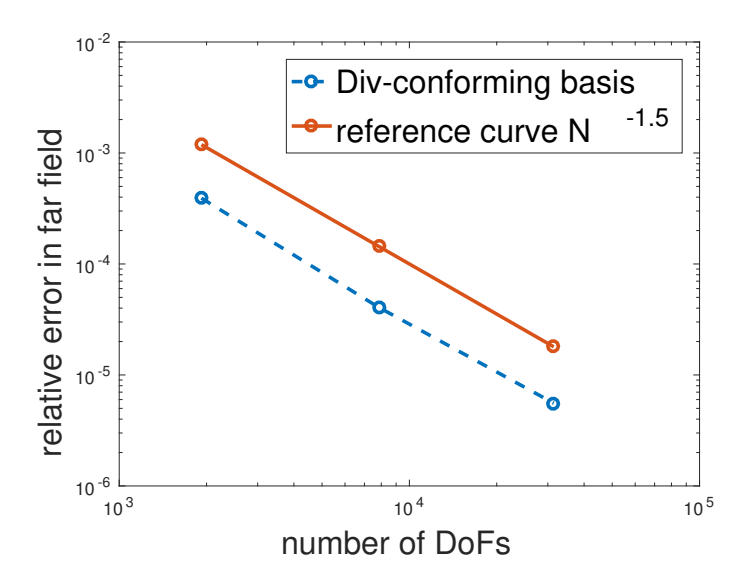


Figure 3.5: Convergence of the relative error in far field for the sphere

The second example is on the scattering from a genus-1 (with one hole) torus. The inner and outer diameters are 1.47λ and 2.52λ respectively, and the incidence is along the axis of the torus. The observed convergence rate shown in Fig.3.6 for first order basis is of the same order as expected.

3.5 Conclusion

This work applies the IGA to multiply-connected structure by using div-conforming basis constructed with the help of jacobians of subdivision surfaces. Numerical examples are presented for validation of the efficacy and excellent convergence performance as well. Details of the implementation, such as function evaluation and singular integral calculation on high order smooth surfaces, together with more numerical results will be presented at the conference.

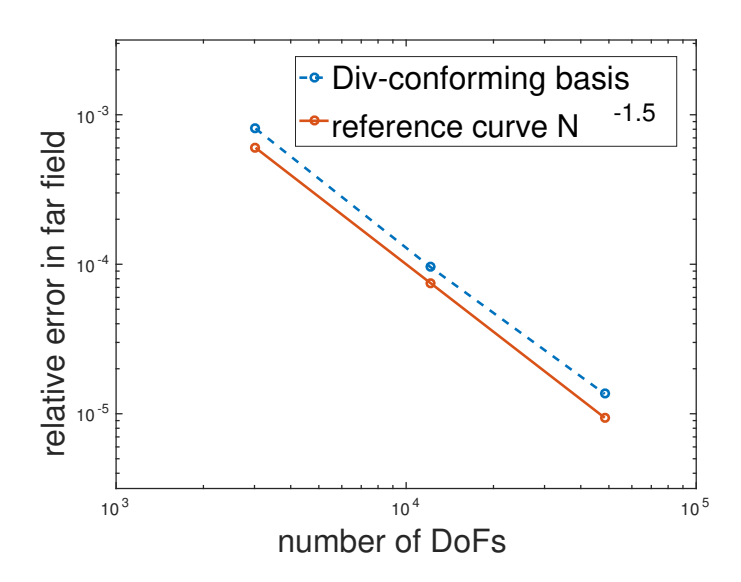


Figure 3.6: Convergence of the relative error in far field for the torus ${\bf r}$

CHAPTER 4

ISO-GEOMETRIC ANALYSIS ENHANCED METHOD OF MOMENTS

4.1 Introduction

Computational methods have become the mainstay of scientific investigation in numerous disciplines, and electromagnetics is no exception. Research in both integral equation and differential equation based methods has grown by leaps and bounds over the past few decades. This period has witnessed development of both higher order basis functions [53–57], and higher order representations of geometry (at least locally) [56–58] amongst many other equally important advances. These approaches have been applied to a wide range of realistic problems spanning several wavelengths.

However, despite advances in these areas, there is a fundamental disconnect between the geometry processing and analysis based on this geometry. Traditional analysis proceeds by defining a discrete representation of the geometry typically comprising piecewise continuous tessellations. Ironically, this discrete representation of the geometry is obtained using software or a computer aided design (CAD) tool that contains a higher order differentiable representation of the geometry. As eloquently elucidated in [44], the rationale for this disconnect can be attributed to the different periods in time that CAD tools and analysis tools developed. As the latter is older, the computational foundation is older as well. As a result, one is left with awkward communication with the CAD software for refining and remeshing. This is especially true insofar as accuracy is concerned; lack of higher order continuity in geometry can cause artifacts if the underlying spaces for field representations are not properly defined. Indeed, the need to define div/curl conforming spaces on tessellations that are only C_0 led to development of novel basis sets that meet this criterion [59]. An alternate approach that has recently been espoused is iso-geometric analysis (IGA). In this approach, the basis functions used to represent the geometry are the same as those used to represent

the physics on this geometry. As a result, the features of geometry representation such as higher order continuity, adaptivity, etc., carry over to function representation as well. Since the appearance of this approach in 2005 [44], it has been applied to a number of applications that range from structure mechanics [60] to fluid-structure interactions (FSI) [61] to contact problems [62] to flow [63] to shell analysis [64,65] to acoustics [66] and electromagnetics [67]. In addition to analysis techniques, the power of IGA has been harnessed for design-through-analysis phase in several practical applications [68–70].

Next, we briefly review some of the existing methods. Most CAD tools use bi/tri-variate spline based patches/solids like those based upon Bezier, B-splines, and non-uniform rational B-splines (NURBS). As a result, these basis functions are the most often used as IGA basis, with the most popular being NURBS. The latter choice is determined by the fact that NURBS is the industry standard for modern CAD systems. Properties such as non-negativity and the fact that it provides a partition of unity make it an excellent candidate for defining function spaces. Finite element methods based on NURBS basis functions that exhibit h- and p-adaptivity have been demonstrated [44]. Unfortunately, the challenge with using NURBS arises from the fact that the resulting shapes are topologically either a disk, a tube or a torus. As a result, stitching together these patches can result in surfaces that are not watertight. These complexities are exacerbated when the object being meshed is topologically complex or has multiple scales [71,72]. Two other geometry processing methodologies gaining popularity for handling shapes that are complex are T-splines and subdivision surface. The former, an extension to NURBS, can handle T-junctions and hence and greatly reduce the number of the control points in the control mesh. T-splines, especially analysis-ready T-splines, comprise a good candidate for constructing iso-geometric analysis. More detailed work on T-splines and its application in IGA can be found in [72, 73] and references therein. As opposed to T-splines, subdivision surfaces have played a significant role in the computer animation industry. Among its many advantages are the ease with which one can represent complex topologies, scalability, inherently multiresolution features, efficiency and ease of implementation. Furthermore, it converges to a smooth limit surface that is C^2 almost everywhere except at isolated points where it is C^1 continuous. There are several subdivision schemes; Loop, Catmull-Clark, Doo-Sabin to name a few. Generally speaking, all of the three of these schemes alluded above can be used to construct IGA method. To date, isogeometric analysis based on subdivision surface is less well studied. Some work on IGA based on Catmull-Clark can be found in [74], where IGA is used to solve PDEs defined on a surface.

While the literature on IGA for differential equations is reasonably widespread across multiple fields, IGA for integral equations is still at a nascent stage. As a result, it has recently become the focus of significant attention. Recently, two dimensional iso-geometric boundary element method (IGBEM) was proposed [75] to study elastostatic problem with NURBS interpolating basis to represent the geometry, displacement and tractions. In [76], IGBEM based on unstructured T-splines was developed for a three dimensional linear elastostatic problem. This approach was extended to address IEs associated with hydrodynamic interactions [68]. Likewise, IGBEM methods have been developed to study acoustic scattering from rigid bodies [66] as well as two-dimensional electromagnetic analysis [77]. To our knowledge, IGA has not been used for solution to three dimensional IEs associated with vector electromagnetic fields, and this serves to motivate this chapter.

The focus of this chapter will be on the construction of a well formulated low-frequency stable IGA solver for the electric field integral equation (EFIE) that is based on subdivision surfaces specifically, the Loop subdivision scheme. As will be evident, the choice of Loop subdivision scheme is only incidental; the presented method can be applied to most subdivision surface description. In developing a solver that is robust, several challenges need to be addressed; these range from definition of basis functions that correctly map the trace of fields on the surface to formulations that render the resulting system frequency stable to formulation of effective preconditioners. To set the stage for introduction of this formulation, we will assume that the surfaces are simply connected and have C^2 smoothness almost

everywhere. As will be evident, the assumption of sufficient "local" smoothness permits significant freedom in terms of defining function spaces. Thus, the principal contribution of this work is four-fold: We will

- present construction of a basis to correctly represent the tangent trace fields on simplyconnected surface,
- demonstrate convergence of EFIE-IGA solver for canonical geometries as well as present applications for complex targets,
- demonstrate stabilization of EFIE-IGA solvers using the proposed basis sets together with frequency scaling,
- demonstrate construction of the Calderón preconditioner using the proposed basis sets (without the need for auxiliary barycentric meshes),
- and, present scattering data from multiscale obstacles.

The chapter is organized as follows: In Section 4.2 outlines the problem, whereas Section 3.2 presents a brief summary of extant literature on subdivision surfaces. Section 4.3 details the crux of this chapter: (i) defines basis functions on the subdivision surface, (ii) develops methods to address low frequency breakdown and multiplicative Calderón preconditioners for the EFIE. Section 4.4 presents several numerical results that verify the accuracy and efficacy of this approach. Finally, Section 4.5 summarizes the contribution of the work as well as outlines directions for future research.

4.2 Integral Equations for Electromagnetic Scattering

The model problem for analysis will be a perfect electrically conducting object that occupies a volume Ω whose surface is denoted by $\partial\Omega$. It is assumed that this surface is equipped with an outward pointing normal denoted by $\hat{n}(\mathbf{r})$. The region external to this volume ($\mathbb{R}^3\backslash\Omega$) is occupied by free space. It is assumed that a plane wave characterized by

 $\{\mathbf{E}^i(\mathbf{r}), \mathbf{H}^i(\mathbf{r})\}$ is incident upon this object. The scattered field for $\mathbf{r} \in \mathbb{R}^3 \setminus \Omega$ can be obtained using equivalence theorems as follows:

$$\hat{n}(\mathbf{r}) \times \mathbf{E}^{s}(\mathbf{r}) = \mathcal{T} \circ \mathbf{J}(\mathbf{r})$$

$$\hat{n}(\mathbf{r}) \times \mathbf{H}^{s}(\mathbf{r}) = \mathcal{K} \circ \mathbf{J}(\mathbf{r})$$
(4.1a)

where

$$\mathcal{T} \circ \mathbf{J}(\mathbf{r}) \doteq -j\omega\mu_0 \hat{n}(\mathbf{r}) \times \int_{\partial\Omega} d\mathbf{r}' \left[\mathcal{I} + \frac{1}{\kappa^2} \nabla \nabla \right] g(\mathbf{r}, \mathbf{r}') \cdot \mathbf{J}(\mathbf{r}')$$

$$\mathcal{K} \circ \mathbf{J}(\mathbf{r}) \doteq \hat{n}(\mathbf{r}) \times \nabla \times \int_{\partial\Omega} d\mathbf{r}' g(\mathbf{r}, \mathbf{r}') \mathbf{J}(\mathbf{r})$$
(4.1b)

where $g(\mathbf{r}, \mathbf{r}') = \exp\left[-j\kappa|\mathbf{r} - \mathbf{r}'|\right]/(4\pi|\mathbf{r} - \mathbf{r}'|)$, κ is the wave number in free space, $\mathbf{J}(\mathbf{r})$ is the equivalent current that is induced on surface, and \mathcal{I} is the idempotent. In the above expression and in everything that follows, we have implicitly assumed (and suppressed) an $\exp\left[j\omega t\right]$ time dependence. Using the above equations, one may prescribe the requisite integral equations as

EFIE:
$$\hat{n}(\mathbf{r}) \times \hat{n}(\mathbf{r}) \times \left(\mathbf{E}^{i}(\mathbf{r}) + \mathbf{E}^{s}(\mathbf{r}) \right) = 0 \quad \forall \mathbf{r} \in \partial\Omega$$
 (4.2a)

MFIE:
$$\hat{n}(\mathbf{r}) \times \left(\mathbf{H}^{i}(\mathbf{r}) + \mathbf{H}^{s}(\mathbf{r})\right) = 0 \quad \forall \mathbf{r} \in \partial \Omega^{-}$$
 (4.2b)

that are known as the electric/magnetic field integral equations (EFIE/MFIE). In (4.2b), $\partial\Omega^-$ denotes a surface that is conformal to but just inside $\partial\Omega$. These equations do not have unique solutions at the so-called irregular frequencies, but may be combined to yield the combined field integral equation [78] that gives unique solution at all frequencies. It should be noted that while these are the most popular formulations that are used in practice, they are not the only ones. Other formulations such as the combined source integral equation [79], augmented EFIE, augmented MFIE [80] and the charge current integral equation [81] exist and have seen recent development. However, this chapter's focus will be on the EFIE and its discretization. The choice is largely motivated by the numerous challenges that exists in solving these equations, both at the mid and low frequency regimes. To this end, in what follows, we will develop basis functions that are well formulated and present modifications

to the formulation to account for both low frequency behavior and to impose Calderón preconditioners.

Methods for solving these equations follow the standard prescriptions: (i) represent the surface of the scatterer using some tessellation, (ii) define basis function on this approximation to the geometry, (iii) demonstrate desirable properties of these basis sets, and (iv) validate solutions to integral equations solved using this procedure. As elucidated earlier, as opposed to classical tessellation, we use subdivision surfaces for geometric representation. This is elucidated next.

4.3 Current Representation and Field Solvers on Subdivision Surfaces

4.3.1 Iso-geometric Basis Sets

Section 3.2 developed a framework wherein one dealt with the representation of the limit geometry surface. Using the same representation as presented earlier, we introduce the concept of scalar functions that are defined on the limit surface. As with geometry, the "limit" function can be represented in terms of 1-ring control weights of a regular triangle and the box splines as

$$f(\mathbf{r}) = f(\mathbf{r}(u, v)) = \sum_{i=1}^{12} N_i(u, v) w_i; \text{ for } \mathbf{r} \in T$$

$$(4.3)$$

where $N_i(u, v)$ denotes the box spline function [49]. Several properties of underlying basis functions for the geometry are worth noting as they are critical to represent both the geometry as well as the physics defined on the geometry. Note, some of these properties are available for a NURBS description as well in the interior of the element, but not necessarily across domains. These include the following:

- 1. compact support,
- 2. non-negativity,

- 3. convexity preserving,
- 4. and C^2 continuity across patch boundaries.

The above properties make this subdivision basis functions a good candidate for modeling physics on both regular and irregular (with the help of subdivision scheme) triangular meshes.

In the above, we have assumed that the mapping $\mathbf{r}(u,v)$ exists, where (u,v) are the barycentric coordinates of a triangle. In what follows, this assumption will be implicit, and only \mathbf{r} will be used. It can be readily verified that if only one vertex has a weight of unity and other zeros, one would immediately get a smooth (up to 2nd order continuity globally) scalar function. As a result, one can associate an effective basis function with every vertex such that the limit function

$$f(\mathbf{r}) = \sum_{n=1}^{N_V} a_n \xi_n(\mathbf{r}) \tag{4.4}$$

where N_V is the number of vertex and $\xi_n(\mathbf{r})$ is an effective basis function that describes the influence of the scalar quantities associated with a vertex. Fig. 4.1a gives an example of the scalar basis function used for formulating iso-geometric analysis on top of subdivision-described surface. The basis function is associated with an irregular vertex of valence 8. To demonstrate 2nd order continuity, the surface Laplacian of the scalar function is plotted in Fig. 4.1b. The behavior of the subdivision basis and its derivatives follow: $\xi_n(\mathbf{r}) \approx O(1)$, $\nabla_s \xi_n(\mathbf{r}) \approx O(1/h)$ and $\nabla_s^2 \xi_n(\mathbf{r}) \approx O(1/h^2)$ where h is an approximate dimension of the patch. Two salient properties of the scalar subdivision basis used for this definition are: (i) as they rely on approximating subdivision they are C^2 almost everywhere; and (ii) if $\Omega = \bigcup_n \Omega_n$, where Ω_n is the domain associated with $\xi_n(\mathbf{r})$, then the function $\xi_n(\mathbf{r})$ vanishes on $\partial \Omega_n$. In other words, the basis functions $\xi_n(\mathbf{r}) \in C_0^2$ almost everywhere.

Next, to use this basis set to represent the current, we note that current on any surface can be represented using a Helmholtz decomposition as follows:

$$\mathbf{J}(\mathbf{r}) = \nabla_s \phi(\mathbf{r}) + \nabla \times (\hat{\mathbf{n}}\psi(\mathbf{r})) + \varpi(\mathbf{r})$$
(4.5)

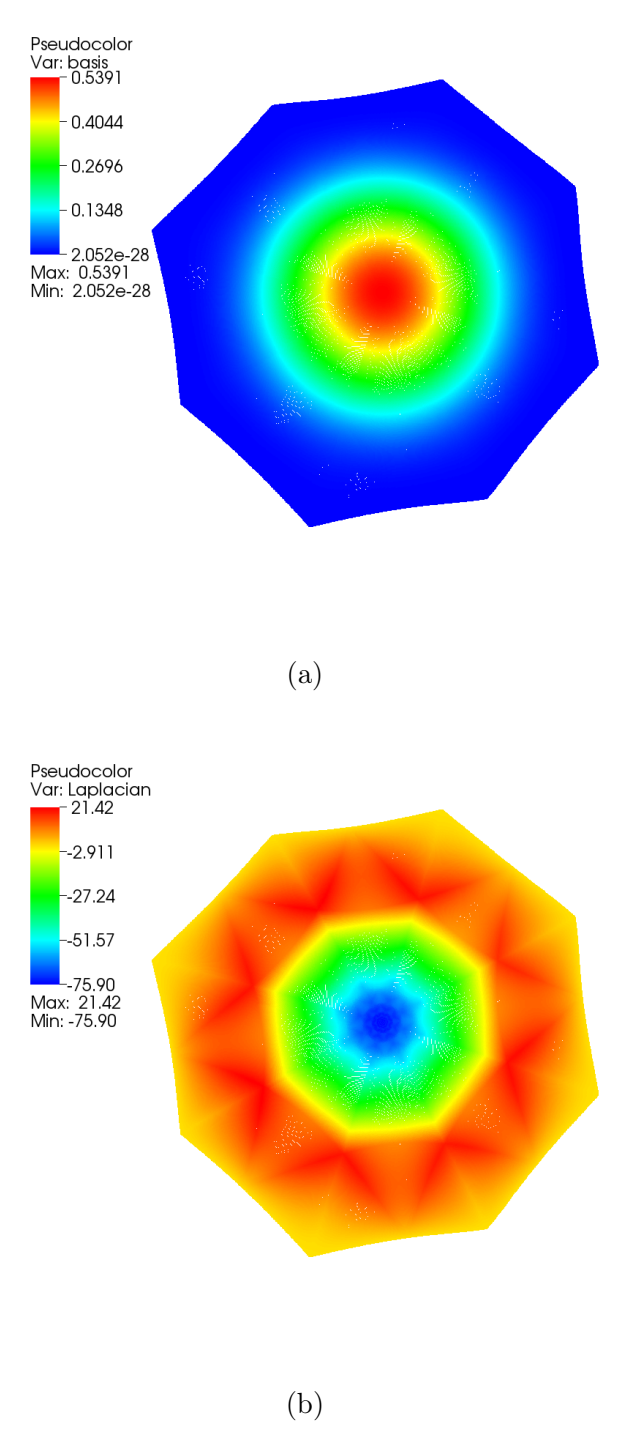


Figure 4.1: Scalar basis function associated with a vertex with valence of 8. (a) Basis function, (b) Surface Laplacian of the basis function

where $\varpi(\mathbf{r})$ is the harmonic field and has a trivial solution ($\varpi(\mathbf{r}) = 0$) for simply-connected structures, and $\phi(\mathbf{r})$ can be associated with the charge space. Following the subdivision

representation in (4.4), we will assume that $\tilde{\phi}(\mathbf{r})$ and $\tilde{\psi}(\mathbf{r})$ represent approximations to $\phi(\mathbf{r})$ and $\psi(\mathbf{r})$, respectively, and they can be represented in a manner similar to (4.4); viz.,

$$\phi(\mathbf{r}) \approx \tilde{\phi}(\mathbf{r}) = \sum_{n} a_{1,n} \xi_{n}(\mathbf{r})$$

$$\psi(\mathbf{r}) \approx \tilde{\psi}(\mathbf{r}) = \sum_{n} a_{2,n} \xi_{n}(\mathbf{r})$$
(4.6)

Using (4.6), it is now possible to define the approximations to the current as

$$\mathbf{J}(\mathbf{r}) \approx \tilde{\mathbf{J}}(\mathbf{r}) = \sum_{n} \left[a_{1,n} \mathbf{J}_{n}^{1}(\mathbf{r}) + a_{2,n} \mathbf{J}_{n}^{2}(\mathbf{r}) \right]$$

$$\mathbf{J}_{n}^{1} = \nabla_{s} \xi_{n}(\mathbf{r})$$

$$\mathbf{J}_{n}^{2} = \hat{\mathbf{n}} \times \nabla_{s} \xi_{n}(\mathbf{r})$$

$$(4.7)$$

The physical interpretation of this representation is akin to a standard subdivision representation of a limit surface; we represent the the "limit" current via the "limit" scalar functions. We note, that the basis for the currents (and the auxiliary potentials) are represented via operations on the subdivision basis which can be effected numerically rather trivially. In this work, the standard definition of the inner product $\langle \mathbf{X}, \mathbf{Y} \rangle = \int_{\Omega} d\mathbf{r} \mathbf{X} \cdot \mathbf{Y}$ is used.

Several properties of the basis functions make this definition appealing. These are as follows:

Continuity Due to the reliance on functions $\xi_n(\mathbf{r})$ that are C_0^2 almost everywhere, the resulting basis functions have C^1 continuity almost everywhere and C^0 continuity at isolated points. This stands in stark contrast with classical Rao-Wilton-Glisson (RWG) [52] or their higher order counterparts [57] that are div-conforming but not C^0 at the boundary.

Orthogonality The inner product of $\langle \mathbf{J}_n^1, \mathbf{J}_n^2 \rangle = 0$. The proof for this assertion can be trivially obtained using Green's theorems together with properties of the surface curl and the fact that $\xi_n(\mathbf{r}) = 0$ for $(\mathbf{r}) \in \partial \Omega$. Specifically,

$$\int_{\Omega_n} d\mathbf{r} \mathbf{J}_n^1(\mathbf{r}) \cdot \mathbf{J}_n^2(\mathbf{r}) = \oint_{\partial \Omega_n} d\mathbf{r} \xi_n(\mathbf{r}) \hat{u} \cdot \mathbf{J}_n^2(\mathbf{r}) - \int_{\Omega_n} d\mathbf{r} \xi_n(\mathbf{r}) \nabla_s \cdot \mathbf{J}_n^2(\mathbf{r})
= 0$$
(4.8)

where \hat{u} is the normal of $\partial \Omega_n$ tangent to the surface.

Representation and Convergence While the use of these basis for geometry exists [49], the convergence of the subdivision-enhanced basis function for scalar fields was presented in the framwork of scalar finite element method [82]. The basis functions used to represent the currents are orthogonal, with the nonsolenoidal component of the current, $\nabla_s \phi(\mathbf{r})$, is only represented through $\mathbf{J}_n^1(\mathbf{r})$, and the solenoidal part is represented through $\mathbf{J}_n^2(\mathbf{r})$. The Hemlholtz decomposition used here is complete. As a result, the tangent spaces show properties presented in [51,83–85].

Charge neutrality The basis functions maintain charge neutrality. This is proved using

$$\int_{\Omega} d\mathbf{r} \nabla_{s} \cdot \tilde{\mathbf{J}}(\mathbf{r}) = \sum_{n} a_{1,n} \int_{\Omega_{n}} d\mathbf{r} \nabla_{s} \cdot \nabla_{s} \xi_{n}(\mathbf{r})$$

$$= \sum_{n} a_{1,n} \oint_{\partial \Omega_{n}} d\mathbf{r} \hat{u} \cdot \nabla_{s} \xi_{n}(\mathbf{r})$$

$$= 0 \text{ as } \nabla_{s} \xi_{n}(\mathbf{r}) = 0 \ \forall \mathbf{r} \in \partial \Omega_{n}$$

$$(4.9)$$

Compactness The definition of basis function is local.

Refinement The basis functions are subdivision based. As a result, they inherit properties of subdivision representation including adaptivity.

These properties ensure a complete representation of the currents on the surface of an simply connected object, and forms a rigorous Helmholtz decomposition of currents on the surface. Again, as opposed to classical basis functions defined on tessellation, Helmholtz decomposition is inherent in the definition of basis functions where as the common approach is to design "quasi"-Helmholtz decomposition using weighted sum of basis functions. It should be noted that, in the above representation, the potential functions are the actual unknown functions and not the currents. As a result, extra steps have to be taken to ensure their uniqueness. These are elucidated below when using these basis functions within a Galerkin framework.

Using these definition of basis functions, each vertex is associated with two degrees of freedom (DoF). Therefore the number of DoFs is twice the number of vertices. This situation is quite different from the hierarchical higher order basis functions that involve polynomials of different degrees (the polynomial degree used is fixed in the proposed IGA.). Fig. 4.2 shows the behavior of the two basis functions associated with a node of valence 8. A point to note is that the number of solenoidal and non-solenoidal basis functions are equal to each other. As we will see, this helps creating Calderón preconditioners. It is also worth noting that the proposed tangent basis set only works for closed surface, since extra requirements, such as no boundary charge, need to be imposed on open edges. The extension to open structures that is nontrivial will be studied in the future work.

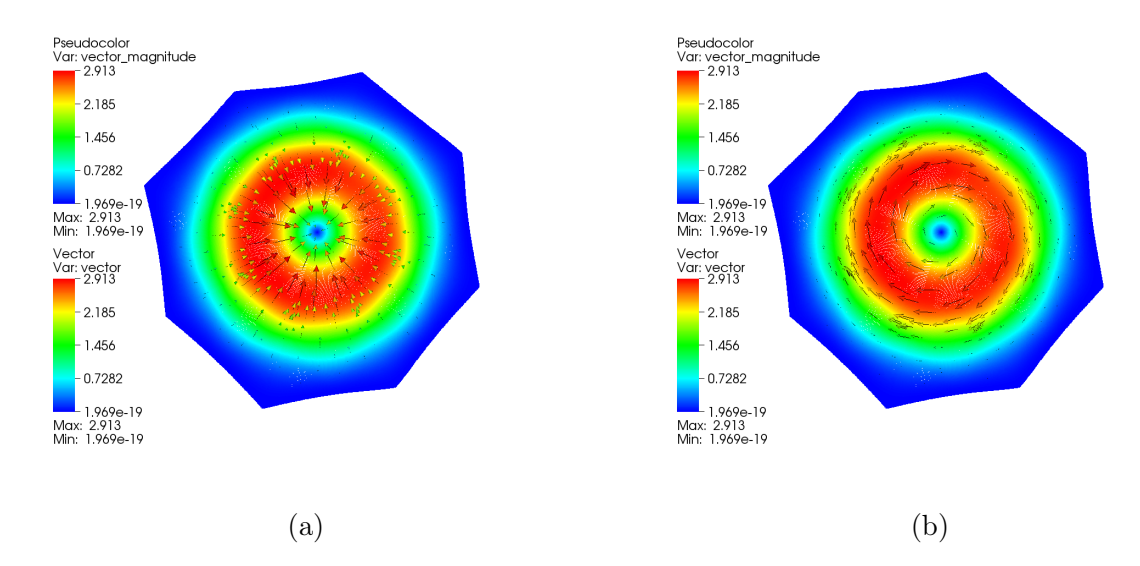


Figure 4.2: Basis function associated with a vertex with valence of 8. (a) nonsolenoidal type, (b) solenoidal type

4.3.2 Field Solvers

Given the prescription of basis functions, the discretized version of (4.2a) can be obtained using Galerkin testing. The resulting matrix equation can be written as

$$\begin{bmatrix} \mathcal{Z}^{11} & \mathcal{Z}^{12} \\ \mathcal{Z}^{21} & \mathcal{Z}^{22} \end{bmatrix} \begin{Bmatrix} \mathcal{I}^{1} \\ \mathcal{I}^{2} \end{Bmatrix} = \begin{Bmatrix} \mathcal{V}^{1} \\ \mathcal{V}^{2} \end{Bmatrix}$$
(4.10a)

where

$$\mathcal{Z}_{nm}^{lk} = j\omega\mu_0 \int_{\Omega_n} d\mathbf{r} \mathbf{J}_n^l(\mathbf{r}) \cdot \int_{\Omega_m} d\mathbf{r}' g(\mathbf{r}, \mathbf{r}') \mathbf{J}_m^k(\mathbf{r}')
- \frac{j\delta_{l1}\delta_{k1}}{\omega\varepsilon_0} \int_{\Omega_n} d\mathbf{r} \nabla_s \cdot \mathbf{J}_n^1(\mathbf{r}) \int_{\Omega_m} d\mathbf{r}' g(\mathbf{r}, \mathbf{r}') \nabla_s \cdot \mathbf{J}_m^1(\mathbf{r}')$$
(4.10b)

$$\mathcal{I}_n^k = a_{k,n}; \mathcal{V}_n^k = \int_{\Omega_n} d\mathbf{r} \mathbf{J}_n^k(\mathbf{r}) \cdot \mathbf{E}^i(\mathbf{r})$$
(4.10c)

In the above equations, δ_{ij} denotes a Kronecker's delta. Interesting features of the above expression are apparent; (i) \mathbb{Z}_{nm}^{11} is the only term that has the charge contribution. As will be shown later, this "decoupling" is an essential component for the construction of low frequency stable solvers, and (ii) since the system of equations are constructed using conditions on currents that rely on derivatives of the potential $\tilde{\phi}(\mathbf{r})$ and $\tilde{\psi}(\mathbf{r})$, it follows that the potentials are determined upto a constant, and the number of degrees of freedom is less by one for each potential. While one can impose this via different means, we have chosen to essentially constrain the system by choosing $a_{1,N}$ and $a_{2,N}$ to be zero. This implies a trivial change to the system of equations (4.10). The evaluation of the inner products in the above equations is effected via higher order quadrature and Duffy integration rules. While the approach presented thus far is valid for all frequencies, it suffers from low frequency breakdown. In what follows, we demonstrate that (4.10) can be modified trivially to alleviate low-frequency breakdown. Likewise, Calderón preconditioners can be easily implemented using this space of basis functions.

But before we proceed, interesting insight may be gained by examining the inner products that arise using the Galerkin procedure. Matrices arise from testing the electric field, i.e., \mathcal{Z}_{nm}^{lk} corresponds to measuring the radiated electric field due to $\mathbf{E}_m(\mathbf{r}) \doteq \mathbf{E} \left\{ \mathbf{J}_m^k \right\}$ by \mathbf{J}_n^l . If follows that

$$\int_{\Omega_n} d\mathbf{r} \mathbf{J}_n^1(\mathbf{r}) \cdot \mathbf{E}_m(\mathbf{r}) = \int_{\Omega_n} d\mathbf{r} \nabla_s \xi_n(\mathbf{r}) \cdot \mathbf{E}_m(\mathbf{r})$$

$$= \oint_{\partial\Omega_n} d\mathbf{r} \xi_n(\mathbf{r}) \hat{u} \cdot \mathbf{E}_m(\mathbf{r}) - \int_{\Omega_n} d\mathbf{r} \xi_n(\mathbf{r}) \nabla_s \cdot \mathbf{E}_m(\mathbf{r})$$

$$= -\int_{\Omega_n} d\mathbf{r} \xi_n(\mathbf{r}) \nabla_s \cdot \mathbf{E}_m(\mathbf{r})$$
(4.11a)

$$\int_{\Omega_{n}} d\mathbf{r} \mathbf{J}_{n}^{2}(\mathbf{r}) \cdot \mathbf{E}_{m}(\mathbf{r}) = \int_{\Omega_{n}} d\mathbf{r} \hat{\mathbf{n}} \times \nabla_{s} \xi_{n}(\mathbf{r}) \cdot \mathbf{E}_{m}(\mathbf{r})$$

$$= \int_{\Omega_{n}} d\mathbf{r} \hat{\mathbf{n}} \times \nabla \xi_{n}(\mathbf{r}) \cdot \mathbf{E}_{m}(\mathbf{r})$$

$$= \int_{\Omega_{n}} d\mathbf{r} \hat{\mathbf{n}} \cdot (\nabla \xi_{n}(\mathbf{r}) \times \mathbf{E}_{m}(\mathbf{r}))$$

$$= \int_{\Omega_{n}} d\mathbf{r} \hat{\mathbf{n}} \cdot \nabla \times (\xi_{n}(\mathbf{r}) \mathbf{E}_{m}(\mathbf{r})) - \int_{\Omega_{n}} d\mathbf{r} \xi_{n}(\mathbf{r}) \hat{\mathbf{n}} \cdot \nabla \times \mathbf{E}_{m}(\mathbf{r})$$

$$= \oint_{\partial\Omega_{n}} d\mathbf{r} \xi_{n}(\mathbf{r}) \mathbf{E}_{m}(\mathbf{r}) \cdot \hat{\mathbf{t}} + j\omega\mu_{0} \int_{\Omega_{n}} d\mathbf{r} \xi_{n}(\mathbf{r}) \hat{\mathbf{n}} \cdot \mathbf{H}_{m}(\mathbf{r})$$

$$= j\omega\mu_{0} \int_{\Omega_{n}} d\mathbf{r} \xi_{n}(\mathbf{r}) \hat{\mathbf{n}} \cdot \mathbf{H}_{m}(\mathbf{r})$$

$$= j\omega\mu_{0} \int_{\Omega_{n}} d\mathbf{r} \xi_{n}(\mathbf{r}) \hat{\mathbf{n}} \cdot \mathbf{H}_{m}(\mathbf{r})$$

In the above equation, \hat{t} is a unit vector tangential to the boundary $\partial\Omega_n$, and $\mathbf{H}_n(\mathbf{r})$ is the magnetic field due to \mathbf{J}_m^k . From the above equations, it is apparent that (4.11a) tests the tangential component of the electric field. However, (4.11b) yields equations that test in normal component of the magnetic field. So the two basis functions used in the analysis impose tangential continuity of the electric field as well as the normal component of the magnetic field. As a result, using a basis that satisfies the Helmholtz decomposition (and relies on scalar function that are C_0^2), results in equations that naturally fit into the framework of the Current-Charge Integral Equations (CCIE) [81]. It should also be noted that while eqns. (4.11a) and (4.11b) were specified for the scattered field, they are equally valid for the incident field. Indeed, using the final expression in (4.11b) to evaluate the integrals is more accurate and requires fewer quadrature points.

4.3.3 Low-frequency Stable EFIE

It is well known that the EFIE suffers from low-frequency breakdown. The rationale for this breakdown is readily apparent by examining the components of the impedance matrix in (4.10). Assuming that the average largest linear dimension of the support of the patch is h. It follows that the entries corresponding to

$$\mathcal{Z}_{nm}^{lk} = \mathcal{O}(\kappa h^2) + \delta_{l1}\delta_{k1}\mathcal{O}(1/\kappa)$$
(4.12)

These results follow from the fact that the functions $\xi(\mathbf{r}) = \mathcal{O}(1)$. The above scaling indicates that a portion of the elements associated with source and test basis functions that are associated with irrotational functions $\mathbf{J}_n^1(\mathbf{r})$ scale as $\mathcal{O}(1/\kappa)$, whereas all others scale as $\mathcal{O}(\kappa h^2)$. This implies that as $\kappa \to 0$, the portion of \mathcal{Z}_{nm}^{11} that corresponds to the charge contribution dwarfs the rest. This situation is similar to those encountered for by classical Nedelec elements. Here, one takes recourse to loop-star/loop-tree decompositions [86–88] that effect an approximate Helmholtz decomposition of the currents. As has been shown, the resulting decompositions contain a portion that is exactly divergence free and one that is approximately curl free. Whereas the support of the divergence-free portion is local, the same is not true of curl-free portion. This is in contrast to the method presented here wherein both components have local support. Using these basis results in the charge being modeled correctly, and a matrix whose scaling looks like (4.12). Rescaling these equations has been shown to render the solution stable. Following a similar procedure, it can be shown that rescaling both the matrix elements, the coefficients and the right hand side results in

$$\mathcal{Z}_{nm}^{lk} = j\omega\beta_{lk}\mu_0 \int_{\Omega_n} d\mathbf{r} \mathbf{J}_n^l(\mathbf{r}) \cdot \int_{\Omega_m} d\mathbf{r}' g(\mathbf{r}, \mathbf{r}') \mathbf{J}_m^k(\mathbf{r}')
- \frac{j\delta_{l1}\delta_{k1}}{\varepsilon_0} \int_{\Omega_n} d\mathbf{r} \nabla_s \cdot \mathbf{J}_n^1(\mathbf{r}) \int_{\Omega_m} d\mathbf{r}' g(\mathbf{r}, \mathbf{r}') \nabla_s \cdot \mathbf{J}_m^1(\mathbf{r}')$$
(4.13)

where

$$\beta_{lk} = \begin{cases} \omega & \text{if } l = 1, k = 1\\ \omega^{-1} & \text{if } l = 2, k = 2\\ 1 & \text{otherwise} \end{cases}$$
 (4.14)

$$\mathcal{I}_{n}^{k} = a_{k,n}\omega^{-\delta_{k1}}; \mathcal{V}_{n}^{k} = \omega^{-\delta_{k2}} \int_{\Omega_{n}} d\mathbf{r} \mathbf{J}_{n}^{k}(\mathbf{r}) \cdot \mathbf{E}^{i}(\mathbf{r})$$
(4.15)

As prescribed, these equations achieve the desired stability. As can be trivially shown, these equations decouple as $\omega \longrightarrow 0$. This is akin to similar prescriptions for classical loop-star/tree algorithms [86,87,89]. However, a *salient* feature of the IGA-basis is that constructing a well behaved system is tantamount to using a *diagonal preconditioning* sans constructing the complementary system that is required for a loop-tree/star (Hodge) decomposition.

It should be noted that Helmholtz decomposition is not the only way to solve low frequency breakdown, and other techniques [81,90–93] exist. The iso-geometric basis functions presented herein could help construct those methods.

4.3.4 Calderón Preconditioner

It is well known that the standard EFIE presented in the earlier sections is a first kind equation, and as with all first kind equations, can be ill-conditioned especially when the spatial scales in the problem are widely separated. As has been shown by several others (see Refs. [51,94,95], and references therein), the rationale for the ill-conditioning is the spectral separation of the eigenvalues of the operator with increase in discretization density, with a set that clusters around zero and others that cluster around infinity. Given this separation, the resulting matrix systems become rapidly ill-conditioned. The remedy to this problem exploits the Calderón identities wherein the EFIE operator ($\mathcal{T}\{\cdot\}$) preconditions itself resulting in a second kind integral operator whose eigenvalues accumulate around -1/4 [51,96,97]. The challenge in using these identities was the lack of well behaved Gram matrices that link the domain and range of the \mathcal{T} operator [97,98]. For Thomas-Raviart/Rao-Wilton-Glisson basis sets and C^0 geometries, basis functions developed by Buffa and Christiansen [99] have been exploited in a sequence of papers to thoroughly understand and solve this problem. In what follows, we show that basis functions defined herein result in a well conditioned Gram matrix, thereby permitting a natural discretization of the Calderón operator. To begin, we

define operators

$$\mathcal{T} \circ \mathbf{J}(\mathbf{r}) = \mathcal{T}_a \circ \mathbf{J}(\mathbf{r}) + \mathcal{T}_\phi \circ \mathbf{J}(\mathbf{r})$$
 (4.16a)

where

$$\mathcal{T}_{a} \circ \mathbf{J}(\mathbf{r}) \doteq -j\omega\mu_{0}\hat{n}(\mathbf{r}) \times \int_{\partial\Omega} d\mathbf{r}' g(\mathbf{r}, \mathbf{r}') \cdot \mathbf{J}(\mathbf{r}')$$

$$\mathcal{T}_{\phi} \circ \mathbf{J}(\mathbf{r}) \doteq -j\frac{1}{\omega\varepsilon_{0}}\hat{n}(\mathbf{r}) \times \int_{\partial\Omega} d\mathbf{r}' \nabla\nabla g(\mathbf{r}, \mathbf{r}') \cdot \mathbf{J}(\mathbf{r}')$$
(4.16b)

The Calderón projector is defined as $\mathcal{T}^2 \circ \mathbf{J}(\mathbf{r}) \doteq \mathcal{T} \circ \mathcal{T} \circ \mathbf{J}(\mathbf{r})$. It has been shown that $\mathcal{T}^2 \circ \mathbf{J}(\mathbf{r}) = (-1/4 + \mathcal{K}^2) \circ \mathbf{J}(\mathbf{r})$, where $\mathcal{K}^2 \circ \mathbf{J}(\mathbf{r}) \doteq \mathcal{K} \circ \mathcal{K} \circ \mathbf{J}(\mathbf{r})$ is compact, and the eigenvalues are clustering around -1/4. Alternatively, this operator may also be written as $\mathcal{T}^2 \circ \mathbf{J} = (\mathcal{T}_a \circ \mathcal{T}_a + \mathcal{T}_a \circ \mathcal{T}_\phi + \mathcal{T}_\phi \circ \mathcal{T}_a + \mathcal{T}_\phi \circ \mathcal{T}_\phi) \circ \mathbf{J}$. Since direct discretization of \mathcal{T}^2 is impossible, typical implementation follows the multiplier approach; i.e., define intermediate mapping from the range space of the \mathcal{T} operator to the domain of the \mathcal{T} . This is typically effected via a Gram matrix and has been extensively explored. Given the usage of Helmholtz decomposition (4.7) and the orthogonality (4.8) between the two components, it can be shown that $\mathcal{T}_\phi \circ \mathcal{T}_\phi \circ \mathbf{J} = 0$. Enforcing the latter condition has been difficult to accomplish in traditional discretization and representation schemes.

The principal advantage of using (4.7) is that it enforces an exact global Helmholtz decomposition in terms of a set of local scalar functions that are C_0^2 almost everywhere. Recall the following: $\langle \mathbf{J}_n^l, \mathbf{J}_m^k \rangle = \gamma_{nm} \delta_{lk}$, where γ_{nm} is the result of evaluating the inner product over the support of basis functions $\Omega_n \cap \Omega_m$ and is defined in (4.18). As a result, the Gram matrix \mathcal{G} is block diagonal with entries $\mathcal{G}_{nm}^{lk} = \gamma_{nm} \delta_{lk}$. Given that, for a pair of spaces, $(\mathbf{J}^1, \mathbf{J}^2)$, it can be shown that the following sequence is satisfied: $(\mathbf{J}^1, \mathbf{J}^2) \xrightarrow{\mathcal{T}} (\mathbf{J}^2, \mathbf{J}^1) \xrightarrow{\mathcal{T}} (\mathbf{J}^1, \mathbf{J}^2)$. Specifically, $(\mathbf{J}^1, \mathbf{J}^2) \xrightarrow{\mathcal{T}_{\phi}} (\mathbf{J}^2, 0)$ and $(\mathbf{J}^1, \mathbf{J}^2) \xrightarrow{\mathcal{T}_{a}} (\mathbf{J}^2, \mathbf{J}^1)$. It follows from the above that $(\mathbf{J}^1, \mathbf{J}^2) \xrightarrow{\mathcal{T}_{\phi}} (\mathbf{J}^2, 0) \xrightarrow{\mathcal{T}_{\phi}} (0, 0)$. In matrix form, the above sequence can be rewritten as

$$\mathcal{T}\mathcal{G}^{-1}\mathcal{T} = \begin{bmatrix} \mathcal{T}_a^{11} & \mathcal{T}_a^{21} \\ \mathcal{T}_a^{21} + \mathcal{T}_\phi^{21} & \mathcal{T}_a^{22} \end{bmatrix} \begin{bmatrix} \mathcal{G}^{11} & 0 \\ 0 & \mathcal{G}^{22} \end{bmatrix}^{-1} \begin{bmatrix} \mathcal{T}_a^{11} & \mathcal{T}_a^{21} \\ \mathcal{T}_a^{21} + \mathcal{T}_\phi^{21} & \mathcal{T}_a^{22} \end{bmatrix}$$
(4.17)

Finally, a critical component in discretizing the \mathcal{T}^2 operator is the Gram matrix. The benefits of using local Helmholtz decomposition becomes apparent in its construction with the off-diagonal blocks being zero and the element of the diagonal blocks being

$$\gamma_{nm} = \int_{\Omega_n \cap \Omega_m} d\mathbf{r} \nabla_s \xi_n(\mathbf{r}) \cdot \nabla_s \xi_m(\mathbf{r})$$
 (4.18)

that are a variational form of the Laplace-Beltrami operator on a scalar function. The resulting system is positive definite leading to well behaved inverse of the Gram system with diagonal preconditioner or simply.

4.4 Numerical Examples

This section presents several numerical examples to demonstrate the efficacy of the proposed approach to electromagnetic analysis. In order to do so, we shall present data that demonstrates the following; (i) accuracy of the approach to when compared against analytical data; (ii) examples illustrating low frequency stability, (iii) analysis of multiscale structures to illustrate the efficiency of the Calderón preconditioner, and (iv) application to complex targets,. Unless stated otherwise, the data presented compares in radar scattering cross-section computed using the IGA-MoM solver and those computed using either analytical methods (if available) or a validated method of moments code that is based on RWG basis functions.

4.4.1 Accuracy of IGA-MoM

To validate and demonstrate the accuracy of the proposed approach, we consider scattering from a sphere discretized at multiple resolutions. To this end, consider a sphere with radius of 1.0 meter that is modeled using an initial control mesh comprising 642 vertices. In all the data presented below, a plane wave field propagating in $\hat{k} = -\hat{z}$ and polarized along \hat{x} axis is incident on the sphere.

First, the performance of the proposed vector basis functions is tested by reconstructing the surface currents due to the incidence plane waves at two different frequencies, 200MHz

Table 4.1: Rel. L_2 error in the reconstructed surface currents density

	subdivision times	0	1	2	3	4
	No. of elements	1280	5120	20480	81920	327680
200MHz	IGA	2.781e-2	2.292e-3	2.365e-4	3.082e-5	5.037e-6
	RWG	9.239e-2	4.456e-2	2.218e-2	1.113e-3	5.604e-3
300MHz	IGA	1.072e-1	7.027e-3	6.633e-4	7.915e-5	1.086e-5
	RWG	1.464e-2	7.137e-2	3.556e-2	1.783e-2	8.946e-3

and 300MHz. At each frequency, the surface is subdivided four times. That would result in five sets of control meshes with face number of surface elements ranging from 1280 to 32,7680. Note, the limit surface for all three mesh densities is identical. As a result, what changes is the support of the basis functions, and therefore, approximations to the discrete operators. The convergence of the relative L_2 errors versus the number of surface elements in the control mesh is given in the table 4.1. The same test was also implemented using the regularly used div-conforming RWG basis. Next, the surface current excited by the incidence waves is solved at 300MHz. Likewise, starting from the control mesh and performing one and two Loop subdivision results in two other meshes with 2562 and 10242 vertices, respectively. The number of degrees of freedom (DoF) for IGA-MoM is twice the number of vertices; consequently, the three tests have 1284, 5124, and 20484 DOFs, respectively. By comparing those obtained using IGA-MoM with Mie series approach, the relative errors in surface currents are 0.0257, 0.0067 and 0.0030, respectively, for these three different discretizations. Fig. 4.3 plots the current distribution, with its radar cross section (RCS) result given in Fig. 4.4. Figs. 4.5a and 4.5b present pointwise errors in absolute values of the real and imaginary parts of the current for the case of two subdivisions. As is evident, the accuracy in the current both in the L_2 and L_1 norms is excellent.

4.4.2 Scattering from Structures at Regular Frequency

In what follows, we analyze the performance of the proposed approach and compare these with a conventional MoM EFIE solution technique that relies on RWG basis functions. Un-

less specified otherwise, the metric for comparison is RCS data in the $\phi = 0$ plane. Furthermore, the geometry of all scatterers that are analyzed in this chapter is smooth; extension to non-smooth structures is non-trivial but realizable from a subdivision perspective [100]. IGA solvers that include in open and sharp surfaces will form the basis of a future work.

The first example is a truncated cone, with the height 3.0λ and the radii of the top and bottom circular cross-sections being 0.2λ and 1λ , respectively. A plane wave that is polarized along \hat{x} and propagating in the $-\hat{z}$ direction is incident on the object. The object is represented using 12378 nodes; this number is increased at the top and bottom surfaces so as to maintain a sufficient degree of sharpness. The number of DoFs for IGA-MoM and conventional MoM are 24756 and 37128, respectively. The surface current density obtained using IGA-MoM is depicted in Fig. 4.6. It is evident from these plots that the currents are smooth (without unphysical aberrations anywhere, especially near the crease). Fig. 4.7 compares the radar cross section between the proposed method and the conventional method of moments, and it is apparent that the agreement between the two is excellent.

The second example is a structure composed of a block $(3.33\lambda \times 10.0\lambda \times 1.33\lambda)$ and five cylinders (radius is 0.5λ and the height is 0.67λ) uniformly distributed on the top surface of the block. An electromagnetic field that is propagating along $-\hat{y}$ and polarized along the \hat{z} incident on this object. The number of DoF for the IGA-MoM and conventional MoM are 29028 and 43536, respectively. Figure 4.8 presents the real and imaginary parts of the current distribution on the surface of the object, and again, it is evident that the results are smooth without artifacts. Further, excellent agreement can be seen between IGA-MoM and conventional MoM in the RCS data.

As a final example in this set, we analyze scattering from a model airplane whose dimensions are $5.49\lambda \times 5.48\lambda \times 1.52\lambda$. The plane wave incident on the object is propagating along $-\hat{y}$ and polarized along \hat{z} . As before, data is obtained using both IGA-MoM and conventional MoM using 23988 and 35976 DoFs, respectively. The current distribution using IGA-MoM is depicted in Fig.4.10. Again, it is evident that the current is well captured as

is the scattering cross-section (see Fig. 4.11).

4.4.3 Conditioning of iso-geometric System at Low-frequency

Next, we discuss the stability of the resulting system (and its preconditioned form) at low frequency using IGA basis and the aforementioned wavenumber scaling. The metrics used for the discussion are both the condition number of the resulting system and the number of iterations necessary to achieve a desired error tolerance when solving this system using an iterative solver. In all the examples presented, we use a generalized minimal residual (GMRES) iterative solver and the object being analyzed is a sphere with radius 1m that is discretized such that the average distance between vertices is around 0.15m.

Fig. 4.12 depicts the condition number of IGA-MoM systems as a function of frequency from 1Hz to 100MHz. The three curves are, respectively, for the original IGA system, the diagonal preconditioned system, the Calderon preconditioned system. From the plots, it is evident that the condition number is almost constant over the whole band for all the systems. Both diagonal preconditioner and application of the Calderón precondition offer significant improvements over the original IGA-MoM. Note, the behavior of the original IGA-MoM is very much unlike conventional MoM, thanks to the properties of the basis function used.

Next, we examine the number of GMRES iterations required to converge to an error tolerance of 1.0×10^{-6} and 1.0×10^{-10} at various frequencies. These results are depicted in Figs. 4.13 and Fig. 4.14, respectively, both sampled at 1Hz, 100Hz, 10^4 Hz, 10^6 Hz and 10^8 Hz. Since the iterative numbers for the original IGA system are much higher than that of the diagonal preconditioned and Calderon preconditioned system, only the iteration numbers for the latter two systems are given. As seen in the two plots, the number of iterations required for both systems are relatively constant across a range of frequencies (from 1Hz to 100MHz).

These two tests serve to illustrate some of the salient features of the proposed approach.

(i) Low frequency stability is achieved simply by diagonal preconditioning. This is in contrast

with conventional approaches where it is explicitly necessary to define auxiliary unknowns albeit at linear cost. (ii) Imposition of the Calderón preconditioner involves an inversion of the Gramm matrix as an addition operation. The original matrix system is retained which makes integration with fast methods trivial. This is different from existing methods that require Buffa-Christiansen basis functions to be defined on barycentric meshes. Finally, as is evident from Fig. 4.15, the results obtained from the Calderón preconditioned solver at 1Hz agrees very well with analytical data obtained.

4.4.4 Examples with Multi-scale Mesh

In all the examples analyzed thus far, the initial control mesh is such that the resulting tesselation is almost uniform in that the ratio of the maximum edge length to the minimum edge length is $\mathcal{O}(1)$. However, a more intellectually interesting and practically applicable problem is when this ratio is significantly higher. It is challenging to design stable methods for these problems due to two effects that act in concert with each other; wavenumber and element size scaling. In this example, scattering from a sphere with locally refined meshes is simulated, and verified by comparing with the one with almost uniform initial control mesh. Fig. 4.16 demonstrates the multiscale control mesh for the unit sphere. The radius of the sphere is 1λ , and the incident plane wave is polarized along the \hat{x} direction and propagating in the $-\hat{z}$ direction. The resulting system of equations is solved using GMRES. Figure 4.17 compares the convergence history for both the Calderón preconditioned system as well as a diagonal preconditioned system. The efficacy of the Calderón preconditioned system is evident by the rapid convergence.

4.5 Conclusion

In this chapter, we have developed a novel iso-geometric analysis technique for solving the electric field integral equation that is encountered in electromagnetic field analysis. The fundamental thesis of iso-geometric methods is that they inherit the rather significant advantages of modern CAD tools—smoothness of geometry representation, morphing, dynamic meshes (if necessary), etc-by using the same basis sets for both geometry representation as well as representation of physics on this geometry. The choice of the electric field integral equation is predicated upon the fact that it is one of the more challenging equations to solve. The approach presented here leverages existing geometric construction techniques that use subdivision to define basis functions that result in well behaved integral operators. Thanks to these operators, it is possible to trivially modify these to impose Calderón preconditioners, and construct systems that are low frequency stable and can handle multiscale geometric features. A number of results demonstrate the convergence and accuracy of the technique, applicability to computation of scattering at both regular and low frequencies, as well as to structures with multiscale features. It is very simple to apply the proposed basis set to other types of integral equations, such as magnetic field integral equation and combined field integral equation. However, as with the introduction of any new technique several open problems remain: these include addition of features to handle edges and open domains, integration with fast solvers, development of techniques for multiply connected objects, using this framework to include Debye sources, etc. Several of these topics are active areas of research within the group and will be presented in different forums soon.

This chapter, ©2016 Elesvier, is reprinted, with permission, from Li, J.; Dault, D.; Liu, B.; Tong, Y. and Shanker, B., "Subdivision based isogeometric analysis technique for electric field integral equations for simply connected structures," Journal of Computational Physics, August 2016, with slight modifications to fit in this dissertation.

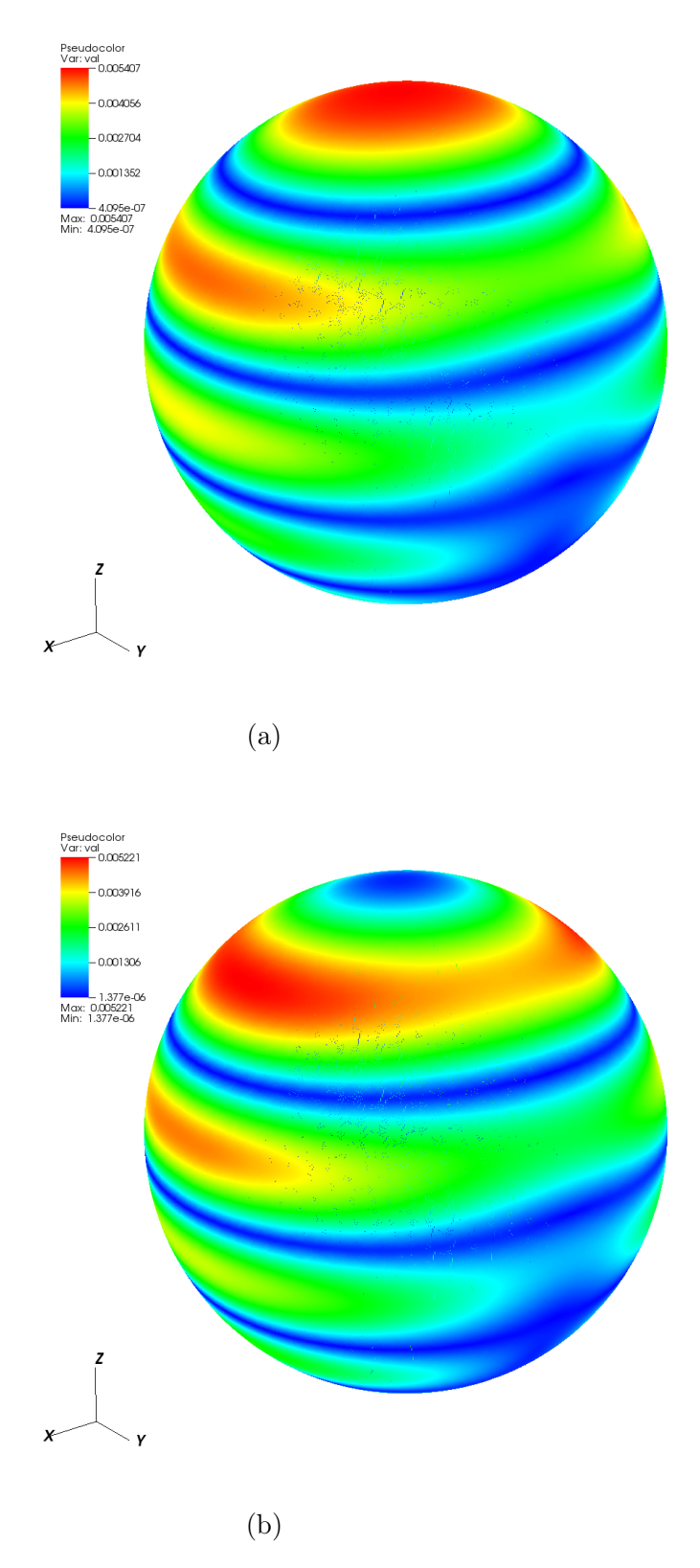


Figure 4.3: Magnitude of surface currents density on the sphere: (a) real part and (b) imaginary part

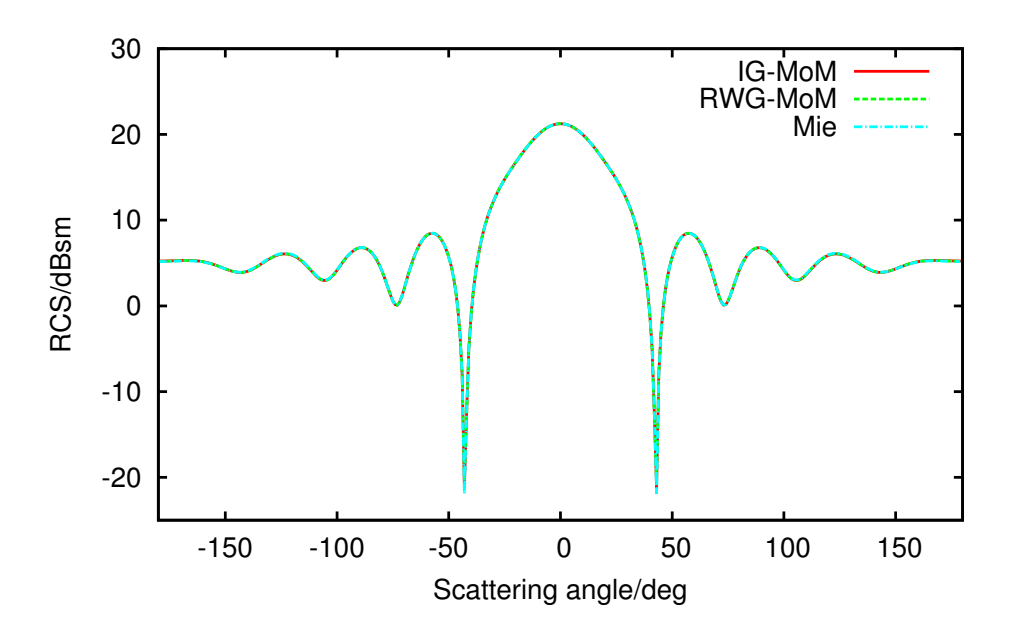


Figure 4.4: Radar cross section of the sphere ($\phi=0$ cut)

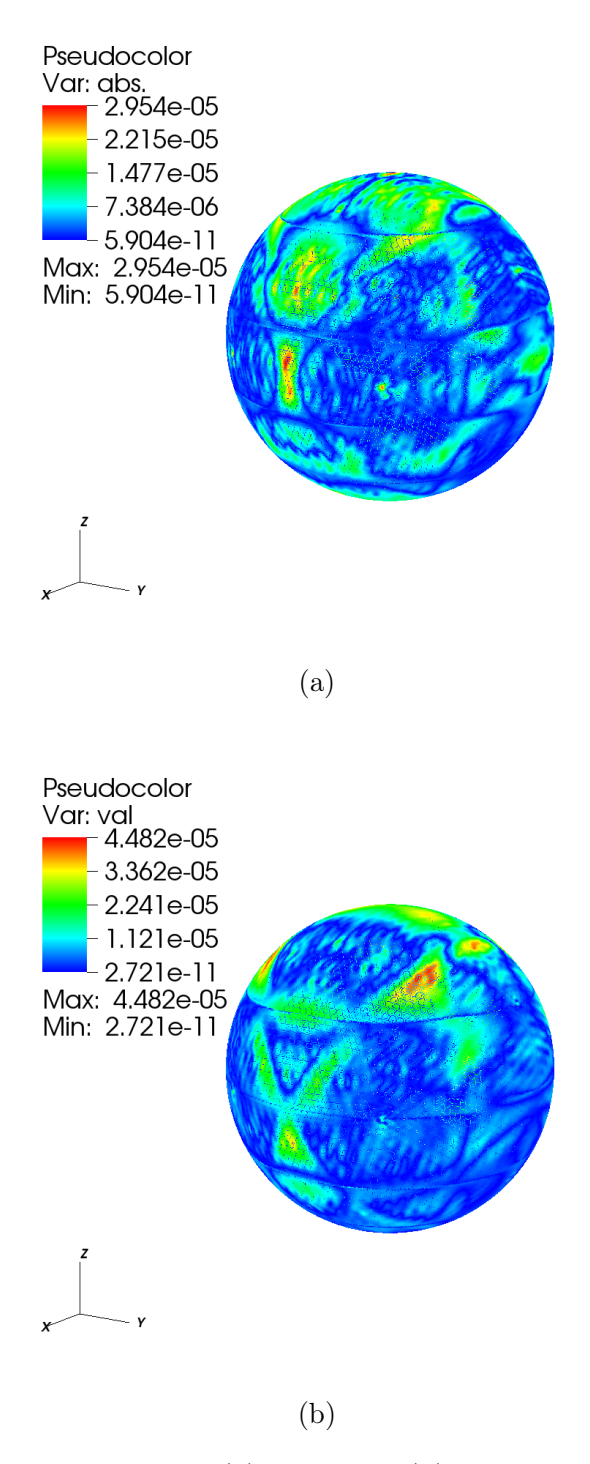


Figure 4.5: Pointwise relative error (a) real part, (b) imaginary part with 20484 DoFs

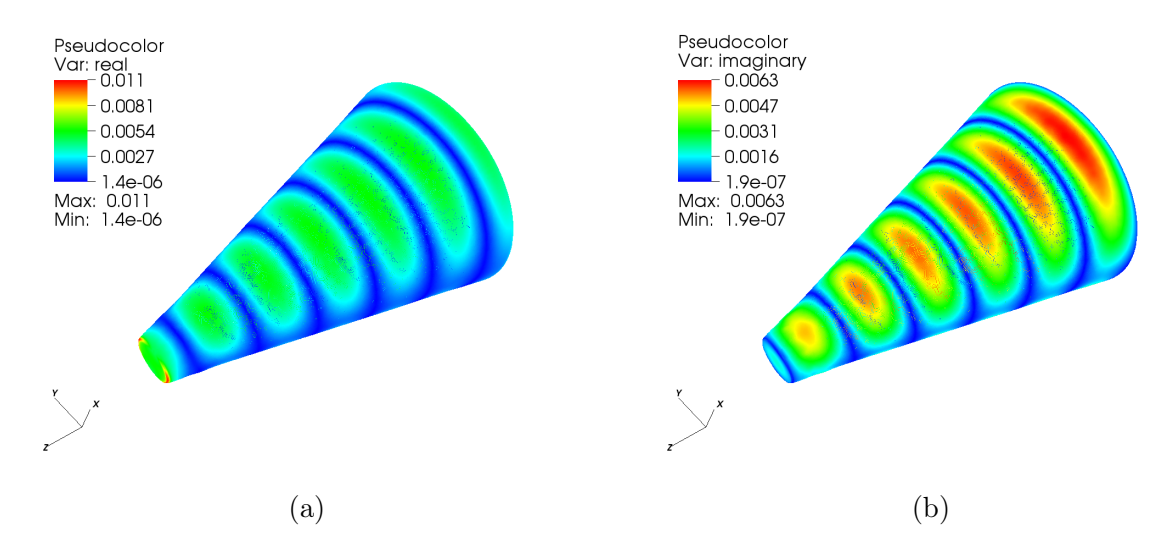


Figure 4.6: Magnitude of surface current density on the truncated cone: (a) real part and (b) imaginary part

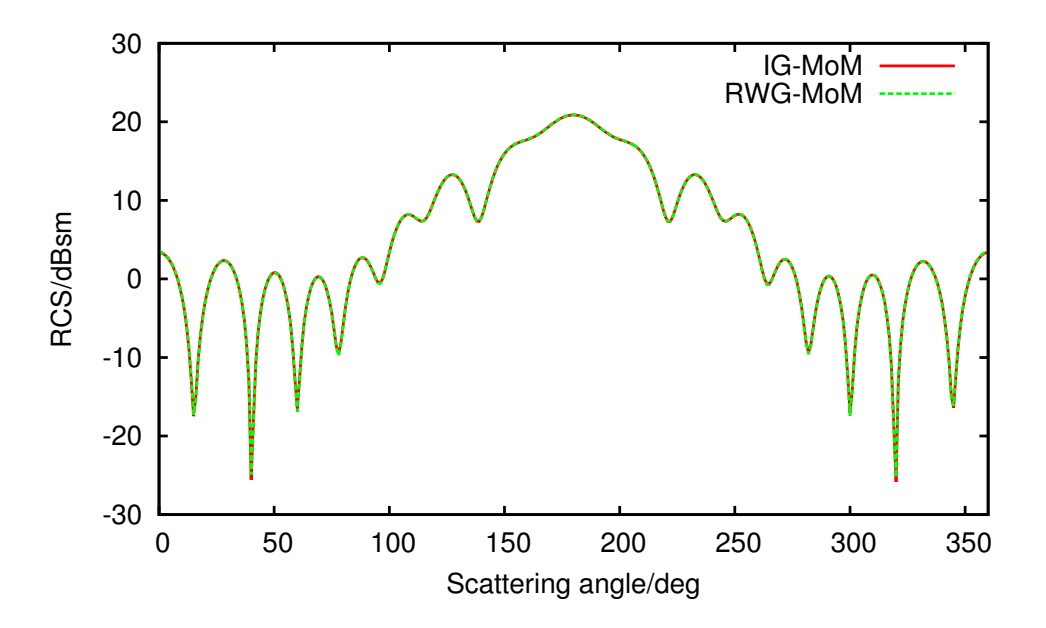


Figure 4.7: Radar cross section of the truncated cone ($\phi = 0$ cut)

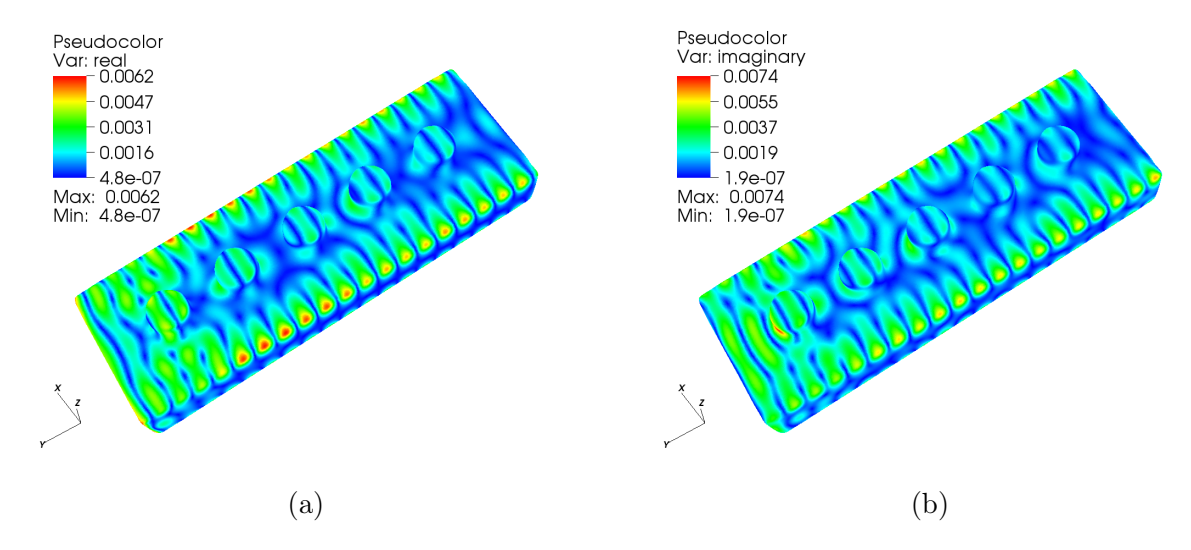


Figure 4.8: Magnitude of surface current density on the composite structure: (a) real part and (b) imaginary part

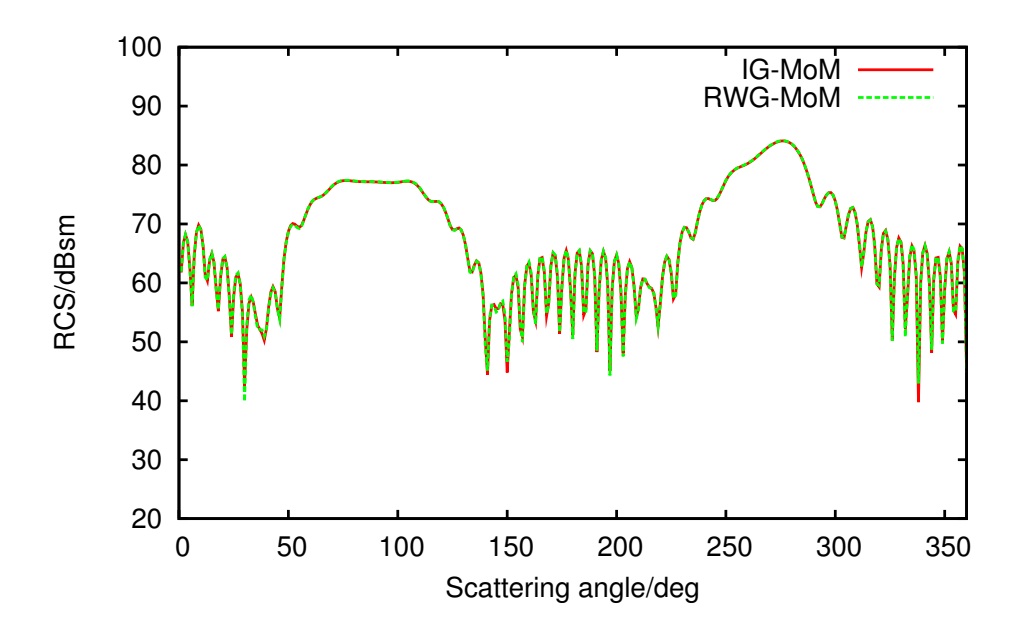


Figure 4.9: Radar cross section of the composite structure ($\phi = 90 \text{ cut}$)

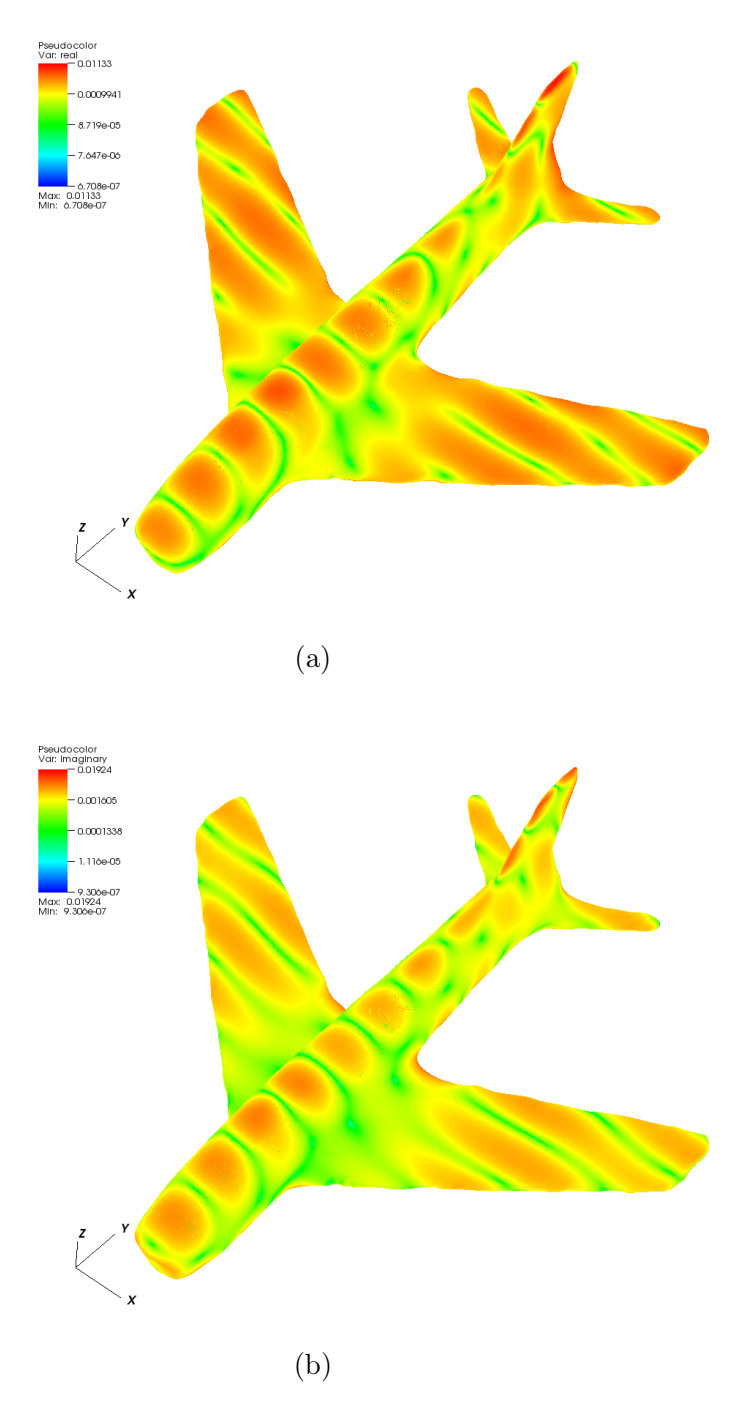


Figure 4.10: Magnitude of surface current density on the air plane model: (a) real part and (b) imaginary part

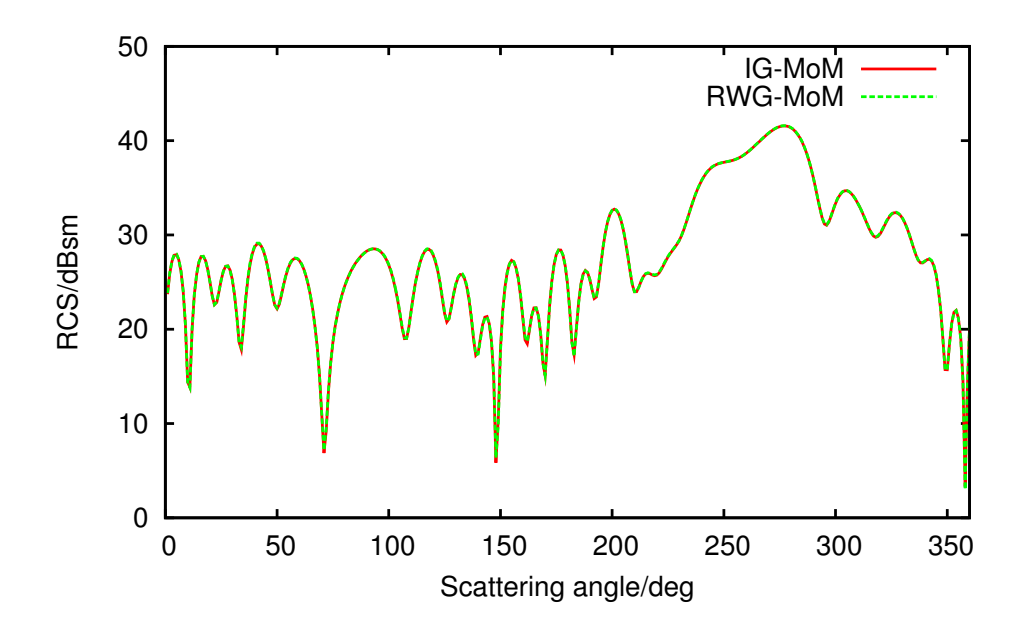


Figure 4.11: Radar cross section of the air plane model ($\phi = 90 \text{ cut}$)

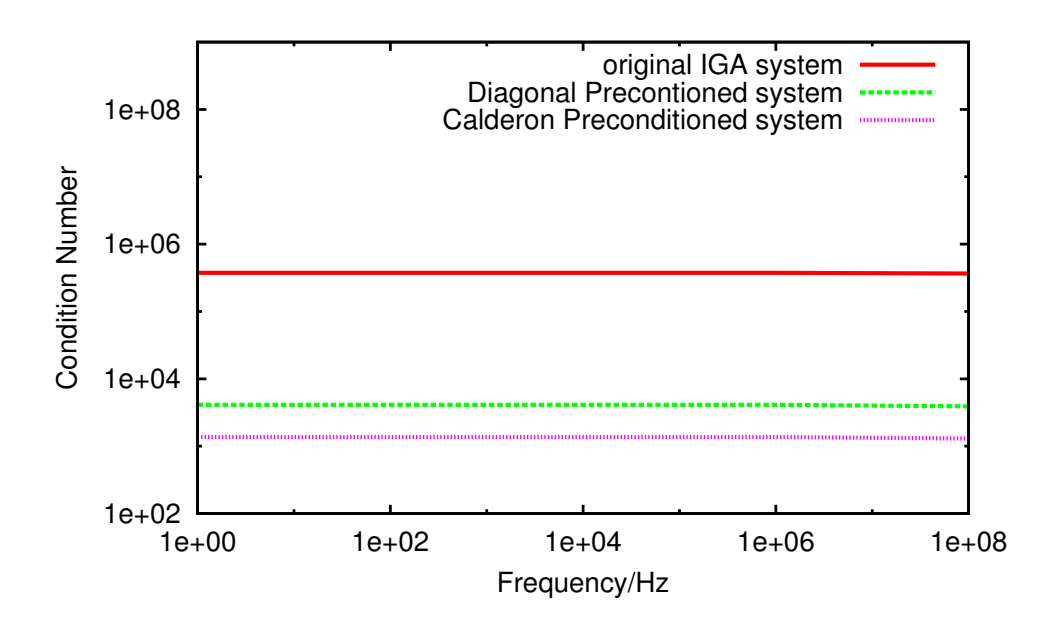


Figure 4.12: Condition number at different frequencies

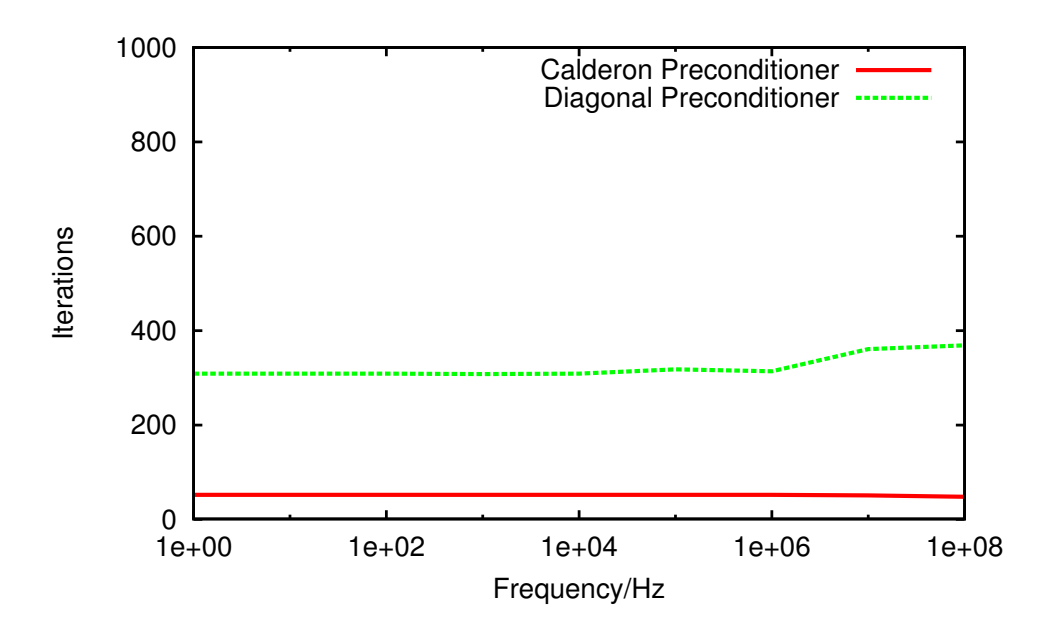


Figure 4.13: Number of GMRES iterations to converge to a tolerance of 1.0×10^{-6}

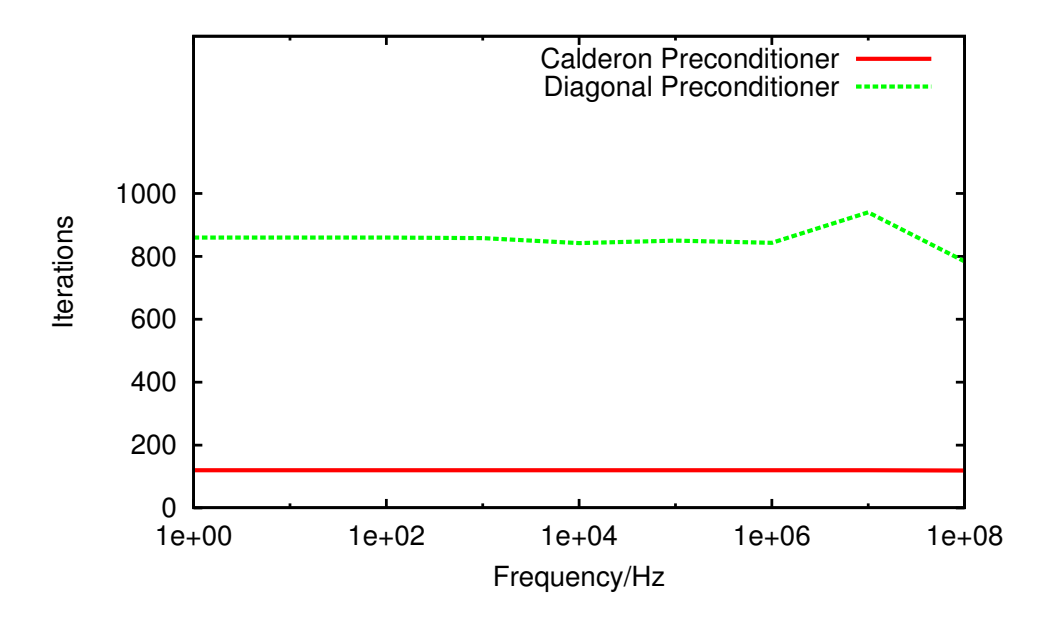


Figure 4.14: Number of GMRES iterations to converge to a tolerance of 1.0×10^{-10}

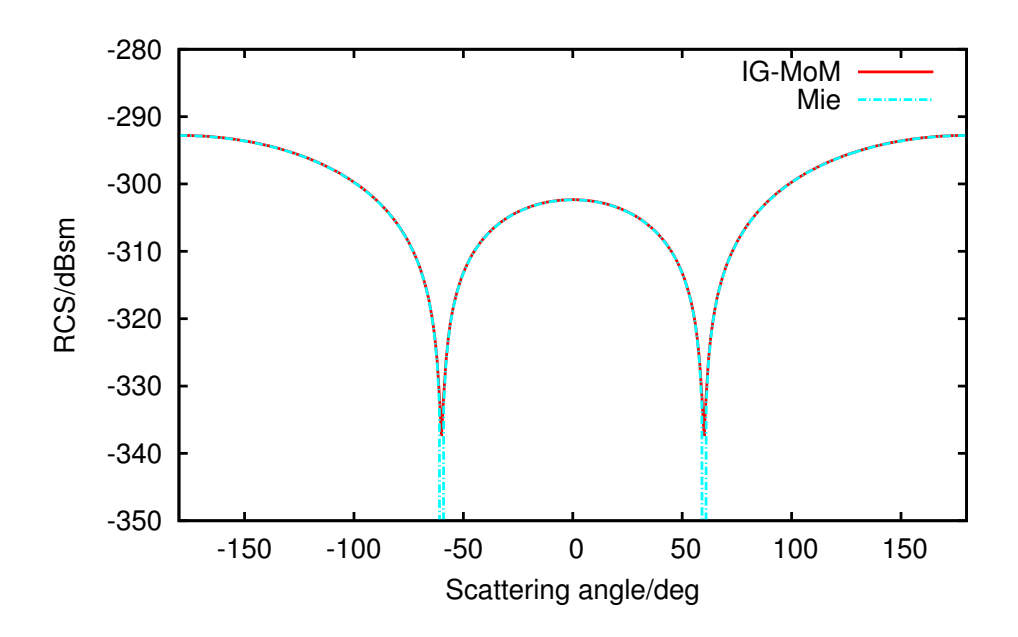


Figure 4.15: Comparison of RCS data obtained at 1Hz with analytical solutions

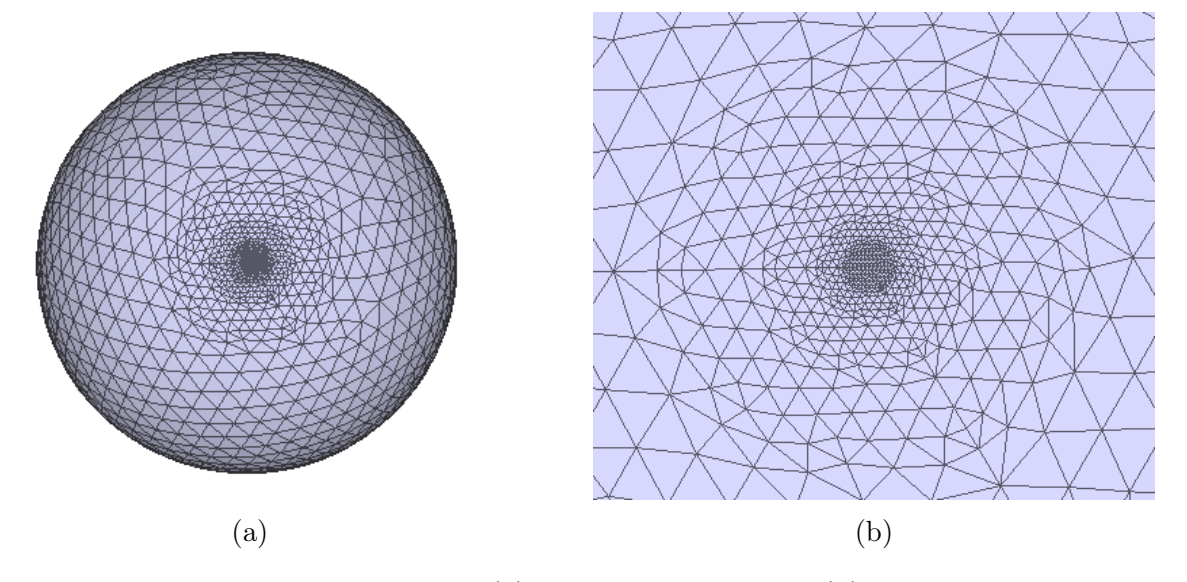


Figure 4.16: Multiscale control mesh: (a) the whole mesh and (b) locally refined region

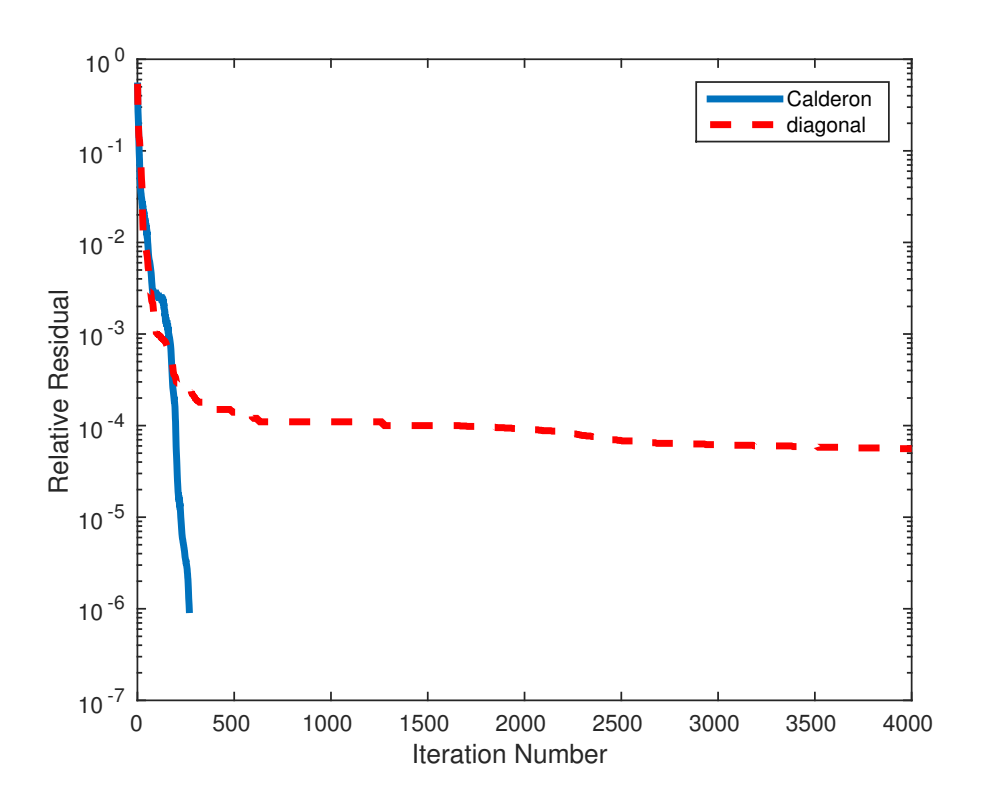


Figure 4.17: Convergence of the iterative solver

CHAPTER 5

SCALAR INTEGRAL EQUATIONS FOR ELECTROMAGNETICS

5.1 Introduction

Surface integral equation based method have long been considered an effective and efficient approach to study electromagnetic scattering and radiation [101]. The integral equation enables the use of surface discretization (hence fewer degree-of-freedom) and its natural marriage with fast divide-and-conquer methods makes it even more popular for engineering analysis. Recent research efforts made by the computational electromagnetics community in surface integral equations can be grouped into categories including fast methods [102], remedies for low-frequency breakdown [87, 91, 103–105], basis functions and higher order methods [52, 56, 99, 106], new formulations [79, 80, 91, 103, 107, 108], flexible geometry representation for design purpose [3, 5, 45], preconditioning techniques [96, 97, 109] and so on. Among them, research in stable formulations, geometry representation and basis functions is of significant importance since it can affect many aspects of the integral equation solvers. For examples, well-conditioned system would definitely enhance the iteration based fast methods; good geometry representation can help the development of high order basis functions and speed up the design and optimization processes. Discussions in this chapter will focus on these aspects: scalar formulation, geometry representation and iso-geometric basis that is inspired by the representation of the geometry.

Most commonly used formulations, like electric field integral equation (EFIE), use the field representations derived from equivalent surface current densities (this is also called direct approach in mathematics community). In these integral equations, two problems arise: (1) unbalanced frequency dependence of the contributions from scalar and vector potentials (the low-frequency breakdown) and (2) div-conforming requirement on basis functions for those currents. Even in some stable integral equation formulations, the post-processing stage

usually involves low-frequency breakdown. Studies focusing on low frequency breakdown include quasi-Helmholtz decomposition based methods [87, 105, 110] and new formulations such as current-charge integral equations (CCIE) [108] and augmented EFIE (AEFIE) [90]. Another approach [5] is based on the use of scalar potential as the unknown to implement the rigorous Helmholtz decomposition (this is cast within an iso-geometric framework). Both CCIE and AEFIE work with extra continuity equation after introducing auxiliary charges in the system. In all of the aforementioned research, save for [5], explicit unknown currents are still involved. In these direct approaches [111], tangent and/or normal components of the field are considered as the observation field. So a natural question is whether there is another set of integral equations that can be derived. Other remedies, using indirect approach with unknowns that don't usually have physical meaning, include generalized Debye sources approach [91, 112, 113] and the more recent work on decoupled potential integral equations [103, 114]. The former leads to a second kind integral equation that is stable over a broadband, which only involves scalar unknowns. The latter solves the problem in a totally different perspective by re-writing the original Maxwell's boundary value problem into one in terms of vector and scalar potentials. The approach presented is similar to the first one, but with different formulations (they are still categorized as direct formulations) and hence the unknowns. Similar effort on the conventional EFIE with scalar basis function is presented in [115], where the tangential component of the electric field is used as the observation field.

In addition to the formulation, discretization of the integral equation also matters in aspects like accuracy and convergence. The discretization involves geometry representation and the construction of basis functions on the geometry. Different formulation might impose certain requirement on geometry and/or basis functions. Studies in these directions include [5, 45, 56, 57, 116]. Most of the studies use piecewise continuous patch representation that might again introduce further difficulties in defining basis or test functions. Furthermore, the mesh on which physical quantities are sampled and represented is usually reduced from high-fidelity geometry representations in computer-aided-design (CAD) software. In contrast, the

iso-geometric analysis [5, 44, 117] embeds more information about the geometry to define the basis function on it, hence no re-meshing process will be needed. Without further geometry accuracy loss, simulation on the native geometry can be more accurate and flexible [5, 44, 117–119]. In [5], scalar potentials are used as the unknown quantity defined on the subdivision surface and are used to solve the conventional EFIE. However, naive extension to magnetic field integral equation (MFIE) will not recover the identity plus compact operator. The scalar integral equation formulations presented in this chapter allow straightforward application of the iso-geometric to both integral equations. The almost C^2 continuous scalar basis function generated in the Loop subdivision surface [48,49] can be used to represent the both the unknown scalar charges and the development of test functions.

The principal contribution of this chapter is theoretical development of scalar integral equations and analytical proofs of stability over a wide frequency range. The results presented serve to validate this theme as opposed to presenting large scale analysis. To this end, the contributions of the chapter are the following: We present

- a rigorous formulation of several stable scalar electromagnetic integral equations,
- analytical stability and spectral analysis over wide frequency band,
- iso-geometric implementation of the well-conditioned formulations on simply connected surfaces,
- and numerical examples demonstrating the accuracy and stability of the iso-geometric analysis of the scalar formulation.

The remainder of the chapter is organized as follows. Section 5.2 derives the scalar formulation from different forms of boundary conditions. Section 5.3 discusses the iso-geometric analysis implementation of the scalar formulations. In section 5.4, spectral properties of the new formulations and performances of the IGA implementations are demonstrated through numerical examples. Conclusion and related remarks are given in section 5.5.

5.2 Formulation

This chapter will focus on electromagnetic (EM) scattering from a simply-connected perfect electric conductor (PEC) or a collection of simply-connected PEC objects. Without losing generality, in what follows only one scatterer is considered in formulating the scalar integral equations.

5.2.1 Problem Statement

Assume the scatterer enclosed by the surface S is illuminated by an incident EM waves denoted by $(\mathbf{E}^i, \mathbf{H}^i)$. Traditional approaches to solving for the scattered fields $\{\mathbf{E}^s, \mathbf{H}^s\}$ rely on the surface equivalence theorem wherein one posits an equivalent current \mathbf{J} that exists on surface S. Then the total fields satisfy boundary conditions on the surface S. Typically, these take the form of twisted tangential field components on the boundary, viz.,

$$\mathbf{n} \times \mathbf{E}^t = \mathbf{n} \times \left(\mathbf{E}^i + \mathbf{E}^s \left\{ \mathbf{J} \right\} \right) = 0 \tag{5.1}$$

and

$$\mathbf{n} \times \mathbf{H}^t = \mathbf{n} \times \left(\mathbf{H}^i + \mathbf{H}^s \left\{ \mathbf{J} \right\} \right) = \mathbf{J}.$$
 (5.2)

The properties of these equations have been explored extensively [51,87,101,104,105,108,114] with regard to their behavior at high and low frequencies, condition number, etc. These equations are used to develop integral equations (that may or may not be well-conditioned). In what follows, we explore an alternative approach.

5.2.2 Charge based Representation

To start, consider the standard mixed potential formulation for the scattered electric field due to surface current densities $\mathbf{J}(\mathbf{r})$,

$$\mathbf{E}^{s}(\mathbf{r}) = -j\omega\mu \mathcal{S}_{k}[\mathbf{J}] + \frac{1}{j\omega\epsilon} \nabla \mathcal{S}_{k}[\nabla'_{s} \cdot \mathbf{J}], \tag{5.3}$$

where the single layer potential operator is defined as

$$S_k[\mathbf{J}](\mathbf{r}) = \int_S G(\mathbf{r}, \mathbf{r}') \mathbf{J}(\mathbf{r}') dS'$$
(5.4)

and $G(\mathbf{r}, \mathbf{r}')$ is the free space Green's function for the Helmholtz equation in free space.

As in [5], Helmholtz decomposition of the surface current can help one introduce scalar sources into the system. Instead of using the potentials, one can introduce charges through the Poisson equation on the surface. Therefore, given two charge sources, one can represent the two generalized Debye potentials [91] as follows:

$$\psi = -j\omega\Delta_s^{-1}\rho, \quad \phi = -j\omega\Delta_s^{-1}\rho_m, \tag{5.5}$$

where Δ_s^{-1} is the inverse surface Laplacian or Laplace-Beltrami operator. By applying the Helmholtz decomposition to the surface currents, one can write the currents with the following representation.

$$\mathbf{J} = -j\omega\nabla_s\Delta_s^{-1}\rho - j\omega\mathbf{n} \times \nabla_s\Delta_s^{-1}\rho_m. \tag{5.6}$$

After replacing the currents in (5.3) with the above one, one can get the following representation of the scattered field;

$$\mathbf{E}^{s} = -\omega^{2} \mu \mathcal{S}_{k} [\nabla'_{s} \Delta'_{s}^{-1} \rho] -\omega^{2} \mu \mathcal{S}_{k} [\mathbf{n} \times \nabla'_{s} \Delta'_{s}^{-1} \rho_{m}] - \frac{1}{\epsilon} \nabla \mathcal{S}_{k} [\rho].$$
(5.7)

Similarly for scattered magnetic field, one obtains

$$\mathbf{H}^s = \nabla \times \mathcal{S}_k[\mathbf{J}] \tag{5.8}$$

and

$$\mathbf{H}^{s} = -j\omega\nabla \times \mathcal{S}_{k}[\nabla'_{s}\Delta'_{s}^{-1}\rho]$$

$$-j\omega\nabla \times \mathcal{S}_{k}[\mathbf{n} \times \nabla'_{s}\Delta'_{s}^{-1}\rho_{m}].$$
(5.9)

It's worth noting that the new representations of both eletromagnetic fields are special cases of the conventional equivalence theorem with native support of the Helmholtz decomposition.

These scalar source based representations, as well as formulations derived later, are different from those in the indirect approach used in [91] where combined current sources are used.

Given these scalar sources, the question is whether one can identify the corresponding scalar field quantities that can be used to construct integral equations. The starting point of the analysis is inspired by [91], wherein divergence of a tangent electric field $(\nabla \cdot (\mathbf{n} \times \mathbf{n} \times \mathbf{E}))$ is chosen. It can be trivially shown that this implies conditions on the divergence of rotated magnetic current. Here, we propose additional conditions on both the trace and the twisted trace of both the electric and magnetic fields; viz:

$$\nabla \cdot (\mathbf{n} \times \mathbf{n} \times \mathbf{E}), \tag{5.10a}$$

$$\nabla \cdot (\mathbf{n} \times \mathbf{E}) \tag{5.10b}$$

of the electric field and

$$\nabla \cdot (\mathbf{n} \times \mathbf{H}), \tag{5.11a}$$

$$\nabla \cdot (\mathbf{n} \times \mathbf{n} \times \mathbf{H}) \tag{5.11b}$$

of the magnetic field.

The main goal of choosing the specific source-observable pair is to allow the use of scalar basis functions and testing functions. Next, several independent sets of IEs derived from boundary conditions associated with the above scalar observables will be introduced.

5.2.3 Scalar Electric Field Integral Equation

In PEC case, one can use (5.10) to construct a set of integral equations as in the EFIE. While one can think of (5.10b) as a condition on surface divergence of the equivalent magnetic current and (5.10a)a as a condition on the surface divergence of the rotated magnetic current, it is also possible to show that (5.10a) is tantamount to imposing conditions on the normal

component of the electric field and its normal derivative via

$$\nabla \cdot (\mathbf{n} \times \mathbf{n} \times \mathbf{E}) = -\nabla \cdot (\mathbf{E} - \mathbf{n}E_n) = \nabla \cdot (\mathbf{n}E_n)$$

$$= \nabla \cdot \mathbf{n}E_n + \mathbf{n} \cdot \nabla E_n$$

$$= JE_n + \mathbf{n} \cdot \nabla E_n,$$
(5.12)

where J is the first curvature of the surface.

By using the scalar representation developed earlier, one can get a set of integral equations for the scattering problem.

$$\nabla \cdot \mathbf{n} \times \mathbf{n} \times \left[-\omega^2 \mu \mathcal{S}_k \left[\nabla_s' \Delta_s'^{-1} \rho \right] - \frac{1}{\epsilon} \nabla \mathcal{S}_k [\rho] \right]$$

$$-\omega^2 \mu \nabla \cdot \mathbf{n} \times \mathbf{n} \times \mathcal{S}_k \left[\mathbf{n} \times \nabla_s' \Delta_s'^{-1} \rho_m \right] = g_1,$$
(5.13a)

$$\nabla \cdot \mathbf{n} \times \left[-\omega^2 \mu \mathcal{S}_k \left[\nabla_s' \Delta_s'^{-1} \rho \right] - \frac{1}{\epsilon} \nabla \mathcal{S}_k [\rho] \right]$$

$$-\omega^2 \mu \nabla \cdot \mathbf{n} \times \mathbf{n} \times \mathcal{S}_k \left[\mathbf{n} \times \nabla_s' \Delta_s'^{-1} \rho_m \right] = g_2,$$
(5.13b)

where $g_1 = -\nabla \cdot (\mathbf{n} \times \mathbf{n} \times \mathbf{E}^i)$ and $g_2 = -\nabla \cdot (\mathbf{n} \times \mathbf{E}^i)$.

The above equations are the scalar equivalent of the electric field integral equations (sEFIE) for solving for scattering from a PEC surface as opposed to the usual tangential components of electric field. It should be pointed out that in this framework we would need to explicitly impose a constraint on charge neutrality on the scalar sources. This is not done in conventional framework that uses div-conforming basis.

5.2.4 Scalar Magnetic Field Integral Equation

A similar procedure can be used for the magnetic fields as well. Using the jump condition on the trace and twisted trace one can obtain two equations

$$\nabla \cdot (\mathbf{n} \times \mathbf{H}^s) + \nabla \cdot (\mathbf{n} \times \mathbf{H}^i) = \nabla \cdot \mathbf{J}, \tag{5.14}$$

$$\nabla \cdot (\mathbf{n} \times \mathbf{n} \times \mathbf{H}^s) + \nabla \cdot (\mathbf{n} \times \mathbf{n} \times \mathbf{H}^i) = \nabla \cdot (\mathbf{n} \times \mathbf{J})$$
 (5.15)

These equations can be used to obtain the following scalar magnetic field integral equation (sMFIE).

$$\rho - \nabla \cdot (\mathbf{n} \times \nabla \times \mathcal{S}_k [\nabla_s' \Delta_s'^{-1} \rho]) + \nabla \cdot (\mathbf{n} \times \nabla \times \mathcal{S}_k [\mathbf{n} \times \nabla_s' \Delta_s'^{-1} \rho_m]) = \frac{g_3}{-j\omega},$$
(5.16a)

$$\rho_{m} - \nabla \cdot (\mathbf{n} \times \mathbf{n} \times \nabla \times \mathcal{S}_{k} [\nabla'_{s} \Delta'_{s}^{-1} \rho])$$

$$+ \nabla \cdot (\mathbf{n} \times \mathbf{n} \times \nabla \times \mathcal{S}_{k} [\mathbf{n} \times \nabla'_{s} \Delta'_{s}^{-1} \rho_{m}]) = \frac{g_{4}}{-i\omega},$$

$$(5.16b)$$

where
$$g_3 = \nabla \cdot (\mathbf{n} \times \mathbf{H}^i)$$
 and $g_4 = \nabla \cdot (\mathbf{n} \times \mathbf{n} \times \mathbf{H}^i)$.

Both of these integral equations are associated with an identity plus compact operators, which means the eigenvalues of the system cluster around a non-zero value if the frequency doesn't correspond to a resonance frequency for the interior domain. Thus, they have better spectral properties than the one derived using electric fields. Direct implementation of the iso-geometric magnetic field integral equation using potential as the unknowns, as in [5], will not necessarily lead to such well-conditioned system.

5.2.5 Combined Integral Equation

It is apparent that both the integral formulations in (5.13) and (5.16) can be used to solve for scattering from PECs and don't involve non-physical solutions at low frequencies. Neither of them has the low-frequency breakdown as a rigorous Helmholtz decomposition is used (indirectly on the current). However they still suffer resonance problem at higher frequencies. To remove it, one can use the approach as in the combined field integral equation (CFIE), which is to use the linear combination of the two integral equation sets. The combined version or the scalar CFIE can be written as

$$sMFIE + \frac{\alpha}{\eta_0} sEFIE, \qquad (5.17)$$

where η_0 is impedance in free space and α is the weighting factor.

5.3 Method of Moments Solution Procedure

In what follows, we prescribe a method of moments solution procedure that is based on a smooth representation of the geometry. The motivation behind this representation is two fold: (i) the preceding formulation makes use of a Laplace-Beltrami operator (and other operators) that rely on a smooth representation of the geometry, and (ii) our using both scalar unknowns and observables opens the door to using the same basis set to represent both the geometry and the unknowns on the geometry. These are elucidated in the next subsection.

5.3.1 Iso-geometric Analysis on Subdivision Surface

To numerically implement the above integral equations, one has to choose suitable geometry representation and corresponding scalar basis functions defined on it. The subdivision surface, unlike polygon or splines based geometric representations, can lead to global smoothness of at least C^1 everywhere for arbitrary shaped surfaces. One of the popular subdivision schemes is called Loop subdivision [48, 49] and it will be used for the implementation purposed in this work. An equivalent basis function that is (a) smooth and (b) of compact support will be generated through the process of subdivision as is detailed in [5, 49]. This leads to the idea of iso-geometric analysis.

Generally speaking, iso-geometric analysis on subdivision surface is chosen to implement the new formulation due to the considerations in two aspects. Firstly, as shown in [5], subdivision enhanced Galerkin method has natural choice of scalar basis functions defined on a globally smooth representations (up to C^2 almost everywhere or at least C^1 everywhere). The same basis used for both physical simulation and geometry representation allows the design-through-analysis in the engineering practice. Secondly, smooth geometry (smooth normal directions in this case) and smooth basis allow the reduction of the singularities, for example, by transferring derivatives from the integral kernels to the test functions.

5.3.2 Scalar Basis Function and Linear System Setup

A scalar function (including each component of the position vector) defined on the the subdivision surface can be evaluated at local coordinate (u, v) by the following expansion

$$f(\mathbf{r}(u,v)) = \sum_{i=1}^{N_v} a_i \xi_i(\mathbf{r}(u,v))$$
(5.18)

where N_v is the number of vertices in the primal control mesh and i is the global index for each vertex. Since each basis function $\xi_i(\mathbf{r}(u,v))$ associated with vertex i has finite (two-neighborhood) support [5,49], the contribution in last expansion can be reduced into a local one,

$$f(\mathbf{r}(u,v)) = \sum_{j=1}^{N_{val}+6} a_j \xi_j(\mathbf{r}(u,v)), \qquad (5.19)$$

where N_{val} is the valence (equal to 6 if there is no irregular vertex) of the irregular vertex in the current element of the control mesh. The expansion (5.19) is quite similar to two dimensional scalar finite element methods, where unknown function can be represented by several basis or interpolatory functions associated with the interested element. The only difference is that, in subdivision basis, the contribution of each vertex is covering triangles in its two ring around it [5,49] (Figure 5.1), rather than 1-ring as in hat functions case, hence there will be more but smooth basis functions contributing to each element.

The basis function can be evaluated in the same way as explained in chapter 3. An example of the basis function associated with a vertex that has a valence of 5 is given in Figure 5.2.

Using Gauss and singular quadrature rules, one can evaluate the elements of impedance matrix. Two parts of the discrete system are involved, where the first one is from the integral operator and the second one is from the surface Laplacian operator. In the first system, surface Laplacian is not considered, as its inverse operator is not explicit available for matrix assembly for generalized surfaces. One can consider the Laplacian as a right preconditioner for general case, though in the sEFIE case the inverse Laplacian operator can be canceled

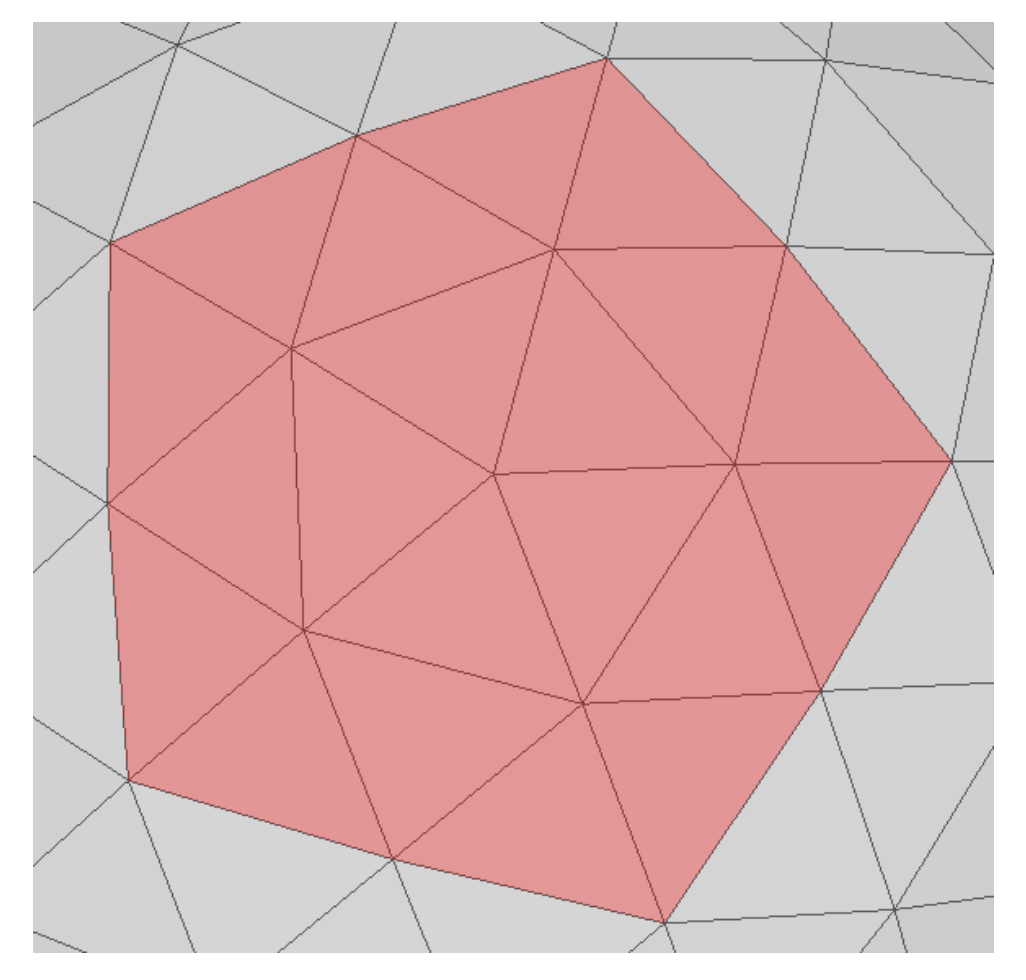


Figure 5.1: The support of the scalar basis: two ring of a valence-5 vertex

in the $\nabla_s \cdot J$ term. Here only the system assembly for the sMFIE is given, since other two formulations can be discretized in the similar way. The first linear system for sMFIE can be written as the 2 by 2 block matrix,

$$Z = \begin{bmatrix} A & B \\ C & D \end{bmatrix}, \tag{5.20}$$

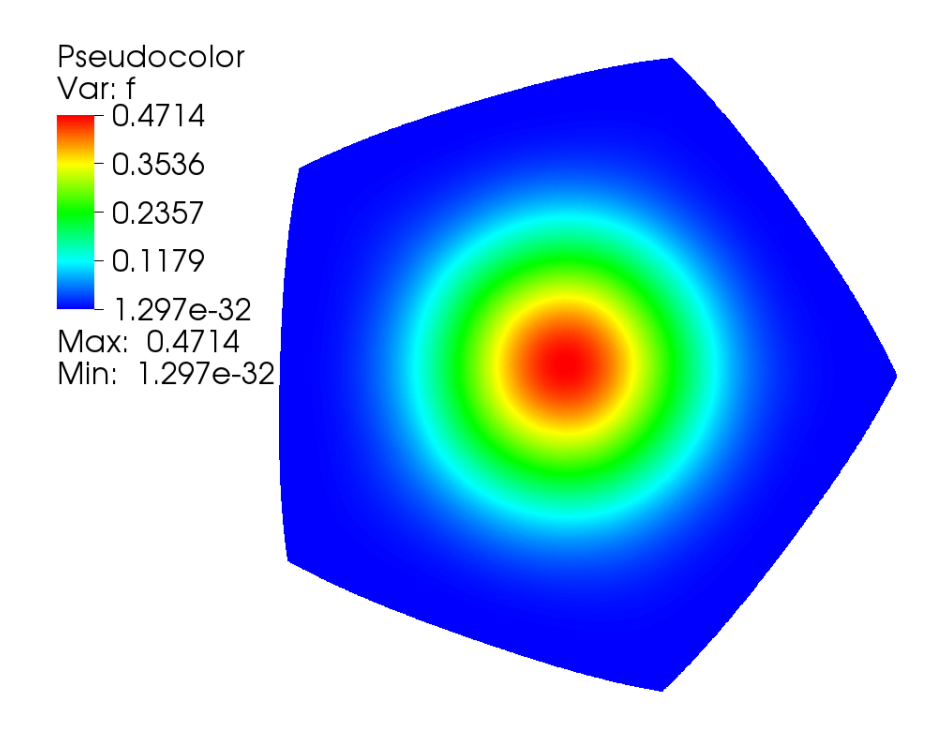


Figure 5.2: Scalar basis associated with a vertex

Each element of the matrix block corresponds to the following integrals

$$A_{ij} = G_{ij} - \int_{S_i} f_i(\mathbf{r}) \mathcal{P}_1[\nabla_s' f_j] dS, \qquad (5.21a)$$

$$B_{ij} = \int_{S_i} f_i(\mathbf{r}) \mathcal{P}_1[\mathbf{n}' \times \nabla_s' f_j] dS, \qquad (5.21b)$$

$$C_{ij} = -\int_{S_i} f_i(\mathbf{r}) \mathcal{P}_2[\nabla_s' f_j] dS, \qquad (5.21c)$$

$$D_{ij} = -G_{ij} + \int_{S_i} f_i(\mathbf{r}) \mathcal{P}_2[\mathbf{n}' \times \nabla_s' f_j] dS, \qquad (5.21d)$$

where G_{ij} is the matrix element (with index $\{i, j\}$) of the Gram system and $\mathcal{P}_1[\mathbf{j}(\mathbf{r}')] = \nabla \cdot [\mathbf{n} \times \nabla \times \int_{S_j} G(\mathbf{r}, \mathbf{r}') \mathbf{j}(\mathbf{r}') dS']$ and $\mathcal{P}_2[\mathbf{j}(\mathbf{r}')] = \nabla \cdot [\mathbf{n} \times \mathbf{n} \times \nabla \times \int_{S_j} G(\mathbf{r}, \mathbf{r}') \mathbf{j}(\mathbf{r}') dS']$.

The second system is the inverse of the surface Laplacian. One has to take the inverse operator through the inverse of the discrete Laplacian. The discrete Laplace-Beltrami operator can be also set up through a Galerkin scheme, the matrix entry of the Laplacian system

can be computed through

$$L_{ij} = \int_{S} \nabla_{s} f_{i} \cdot \nabla_{s} f_{j} dS \tag{5.22}$$

where the numerical integration for each matrix element could only happen on a compact region due to the compactness of the basis functions. The nonsingular right hand side vector can be evaluated similarly using Gauss quadrature as in regular methods of moments.

5.3.3 System Solution

The solution to the system of equations is slightly more challenging than a conventional system due to the inverse of the surface Laplacian that is involved in the solution procedure. As will become apparent, direct solutions are difficult. As a result we take recourse to an iterative procedure. The two steps in the solution procedure are as follows: (1) invert the discrete surface Laplacian operator that operates on charge data and (2) solve the discrete pseudo-impedance system that operates on the potential data. The first step, in our work, is implemented through an inner iterative solver, conjugate gradient based solvers are effective in solving the surface Laplacian system [115]. Special care has to be taken to carry out the first step since the surface Laplacian operator is exactly rank-deficient by one. One can compute the inverse by either reducing the rank of the system accordingly as in [5] or using more rigorous methods as discussed in [115]. The second step is identical to that used in regular method of moments implementations, which can be accelerated by fast algorithms [102].

5.4 Numerical Examples

In this section, the proposed formulation will be studied in several aspects through numerical examples. First, the spectral properties and stabilities will be tested on the unit spherical surface. Next, validation of the numerical implementation will be given, together with convergence study of the iterative solver. Finally, more generalized examples are studied.

5.4.1 Spectral Properties

In this test, the analytical properties of system of equations derived earlier are studied using spherical harmonic functions on a unit sphere. Since only scalar basis functions are required, the scalar tesseral harmonics are used in a Galerkin framework to derive a modal representation of the system of equations; as is expected, this is block diagonal matrix, with each block corresponding to one mode. The procedure is very similar to the one that models quasi-analytical transient acoustic scattering in [3]. If no surface Laplacian is involved, the modal system is quite similar to the their vector counterparts in [51]. Here we examine the properties of the scalar formulations, especially the scalar MFIE, that has not been reported elsewhere.

First, in the low frequency range where ka < 1, the conditioning for three systems are studied. The condition number and the eigen-condition number are used to examine the behavior of these equations across the frequency spectrum, where the eigen-condition number denotes the ratio between largest and smallest absolute values of eigenvalues. It is noted that neither sEFIE nor sMFIE will suffer from the spurious resonance problem within the interested low frequency range that is below the first resonance frequency of the corresponding spherical cavity. Only scalar EFIE, with its scaled version (as in [2] or other loop-tree or loop-star based methods), and MFIE are studied here. Figure 5.3 plots condition number curves versus the frequency for three systems, and the corresponding eigen-condition number results are shown in Figure 5.4. From both figures, one can see the scaled scalar EFIE and scalar MFIE have stable condition numbers over the wide low-frequency band. In scaled scalar EFIE case, the fundamental reason is that Helmholtz decomposition and frequency-rescaling resolve the low-frequency breakdown. However, in scalar MFIE case, the existence of second kind integral operators ensures the good conditioning in the interested frequency range.

Second, at high frequencies, the spectral behaviors are tested by plotting the eigenvalues of the interested system. At high frequency, neither sEFIE nor sMFIE is immune from

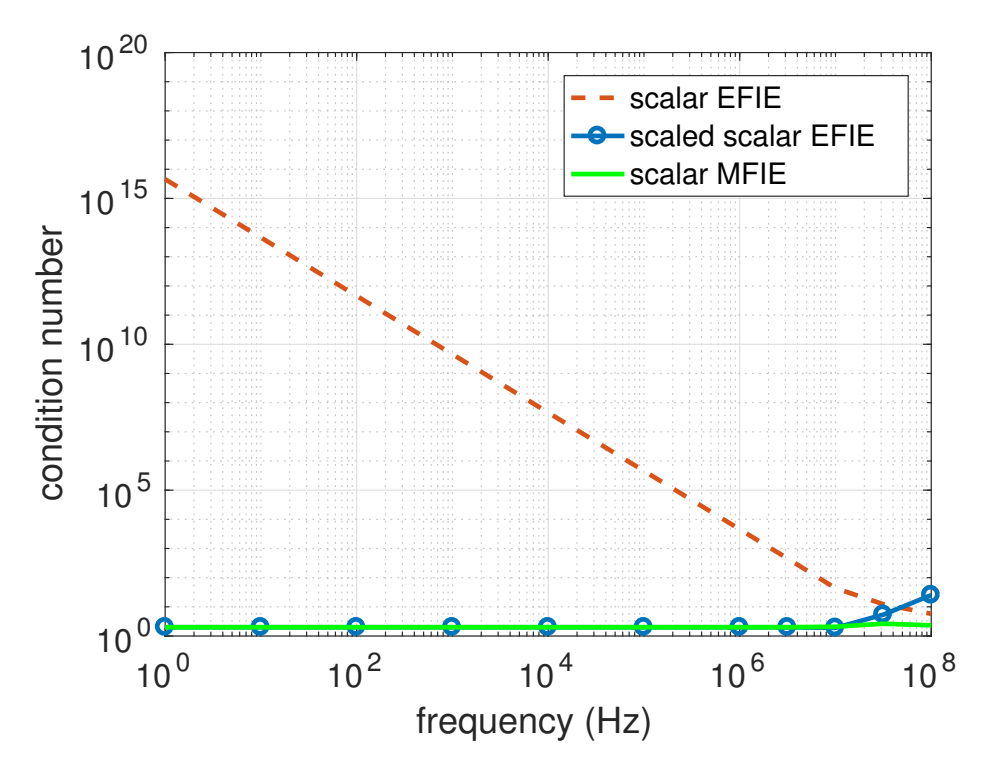


Figure 5.3: Condition number versus frequency

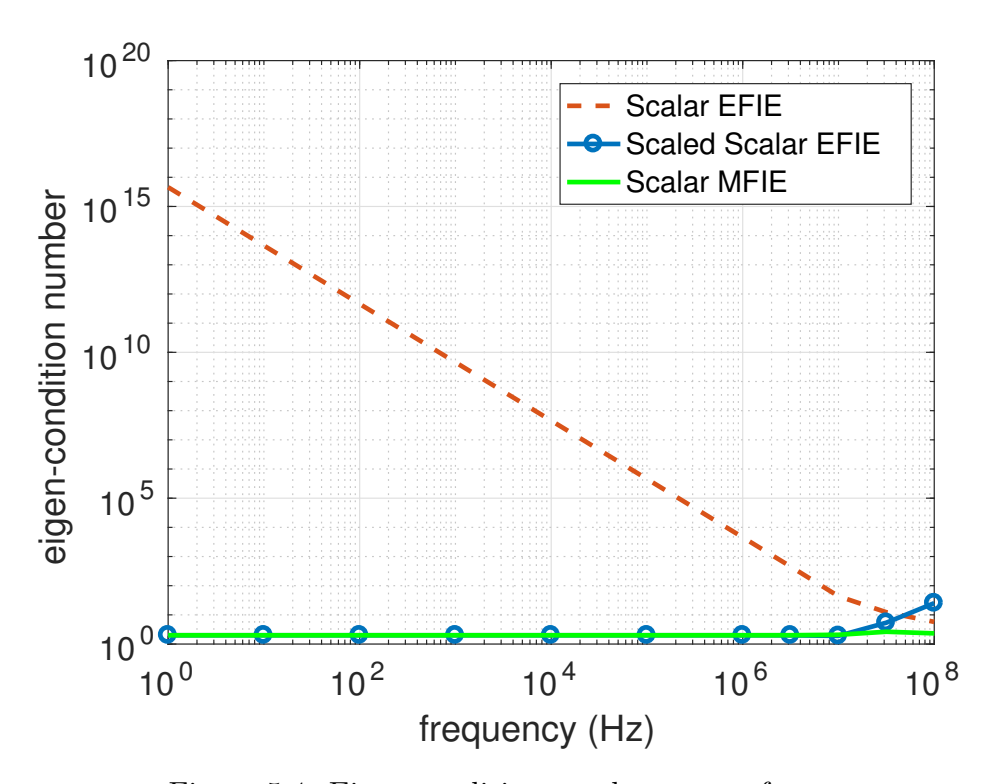


Figure 5.4: Eigen-condition number versus frequency

internal resonance, hence, combined version of scalar formulations has to be used. Figure 5.5 and Figure 5.6, respectively, demonstrate the eigenvalues and singular values of three systems (sEFIE, sMFIE and the combined formulation), where the frequency is f = 10 GHz and the highest mode is at the degree of n = 210. The singular value distributions are very similar across the formulations while the performances in eigenvalue spectra are very different. Since the sMFIE is a second kind integral equation, it can keep the compact spectrum as the regular MFIE, much better than that of scalar EFIE. Due to the spectral properties of the operators in sEFIE, the combined formulation is not second kind anymore, however, as is expected its spectrum is better than that of the scaled sEFIE.

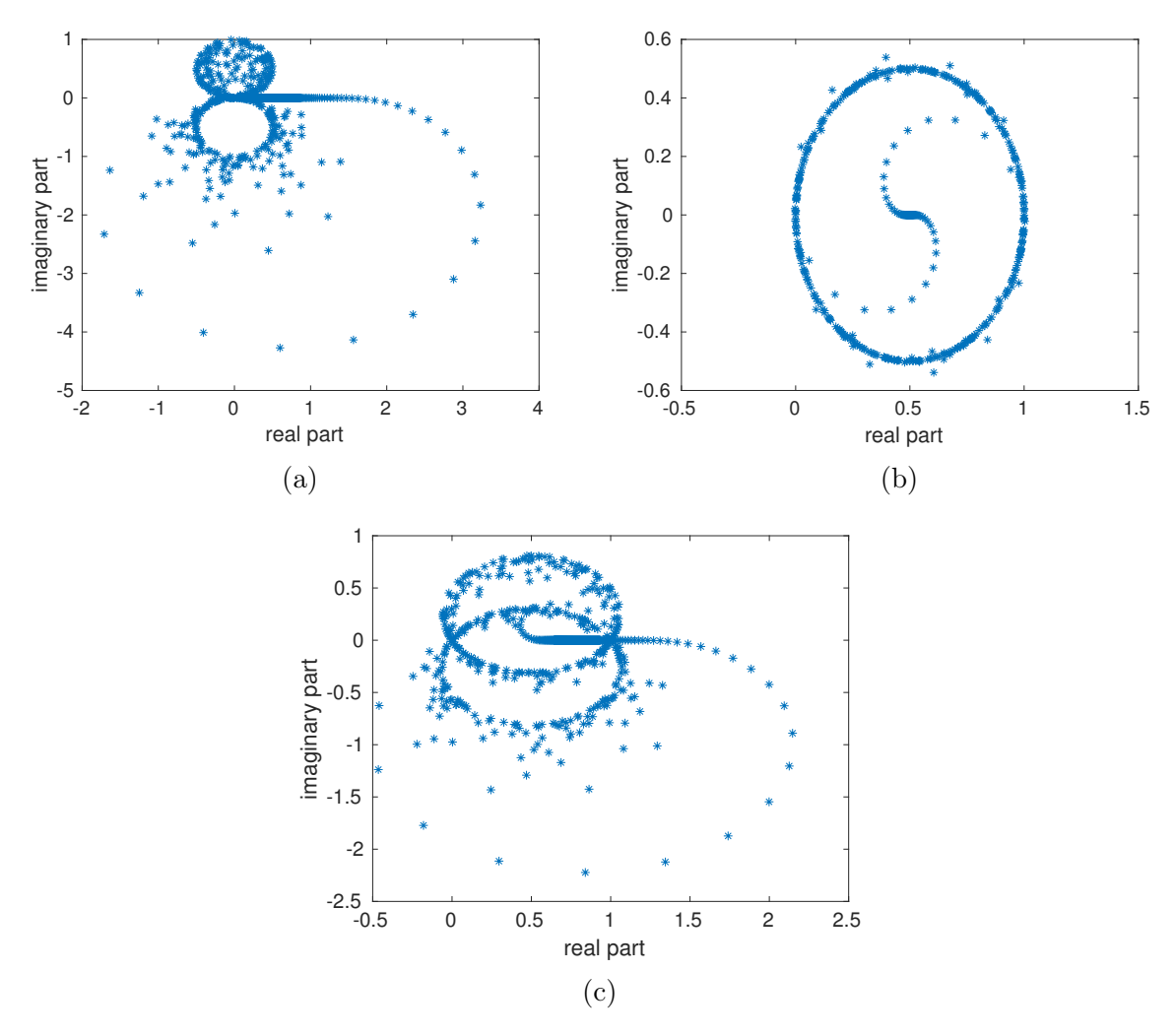


Figure 5.5: Eigenvalues of the system of (a) scalar EFIE, (b) scalar MFIE and (c) scalar CFIE with $\alpha=0.5/\eta$

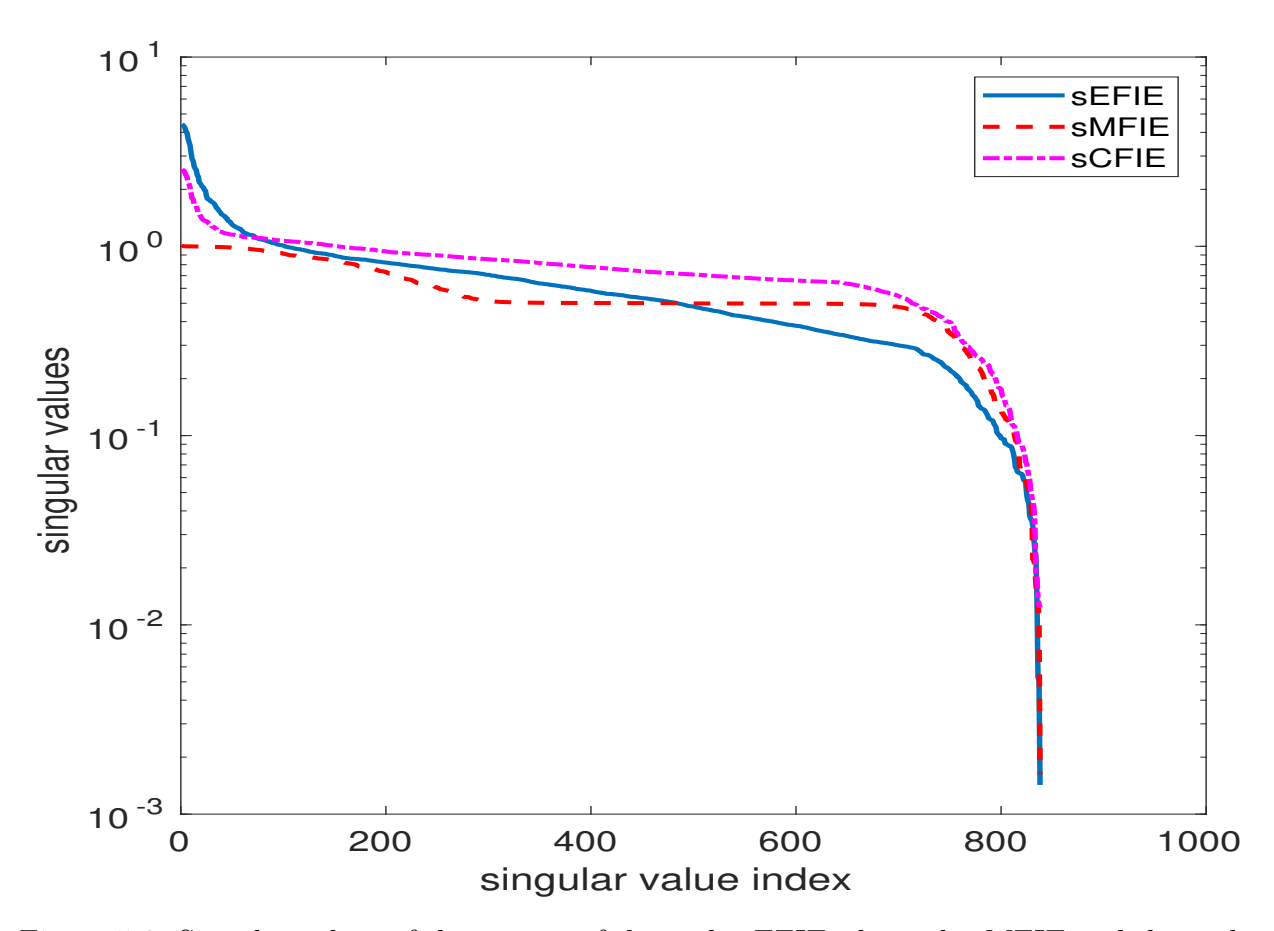


Figure 5.6: Singular values of the system of the scalar EFIE, the scalar MFIE and the scalar CFIE with $\alpha = 0.5/\eta$

5.4.2 Numerical Test

Next, we test the accuracy of the formulation numerically by computing the radar cross section of the unit sphere. An \hat{x} -polarized plane wave propagating in the \hat{z} direction at frequency $f=600 \mathrm{MHz}$ is used as the incidence field. In the geometry representation, 2562 control vertices are involved, therefore the total number of degree-of-freedom is 5124 for all the three cases. The linear solver chosen is GMRes (generalized minimal residual method) with restart set to 30, without using any preconditioner. The radar cross section data of $\phi=0$ cut in the far field are computed using the presented formulation and given in Figure 5.7, and analytical result from Mie series approach are also plotted for reference. Note that all the error in all three formulations at this frequency give almost the same relative error in far field values ($\sim 2 \times 10^{-3}$); therefore only one result is actually plotted.

The performances of the iterative solver for the three formulations are given in Figure 5.8. At this specific frequency, the sCFIE shows the better performance than sMFIE simply because of the oscillating nature of eigen-spectrum of the MFIE formulation even though the frequency chosen does not correspond to a spurious resonance frequency. As shown in the the result, the sEFIE, like in regular EFIE case doesn't convergence fast, as is expected from the spectrum of the sEFIE operator.

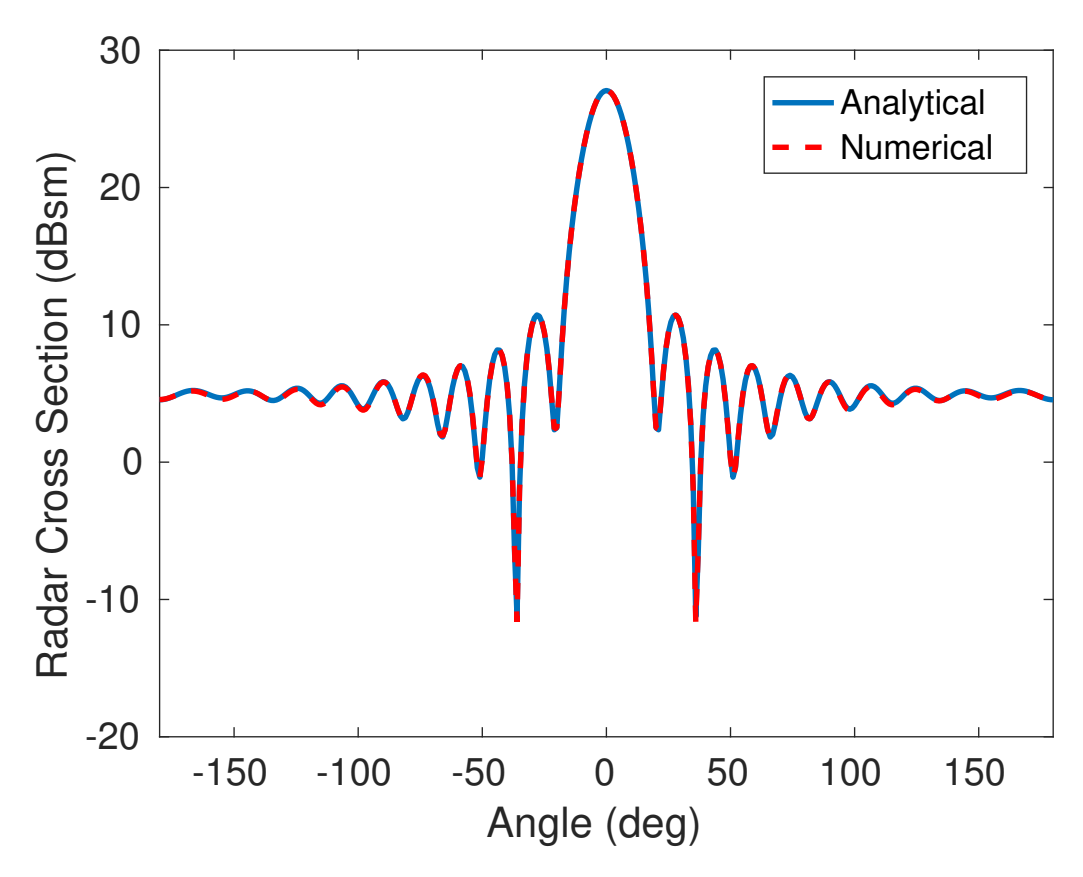


Figure 5.7: Radar cross sections of the sphere

Finally, a more complicated structure, the toy plane model with dimension around $11m \times 11m \times 3m$ in Figure 5.9, to show the stability of the sMFIE formulation at low frequency range. The model is presented by the subdivision surface with 11,994 vertices, that corresponds to 23,988 unknowns when the integral equation is discretized. The incidence field is \hat{x} polarized and propagating along \hat{y} . The scattering problem is solved at different frequencies, mainly at low frequency range. The current density distribution at 10MHz is also demonstrated in

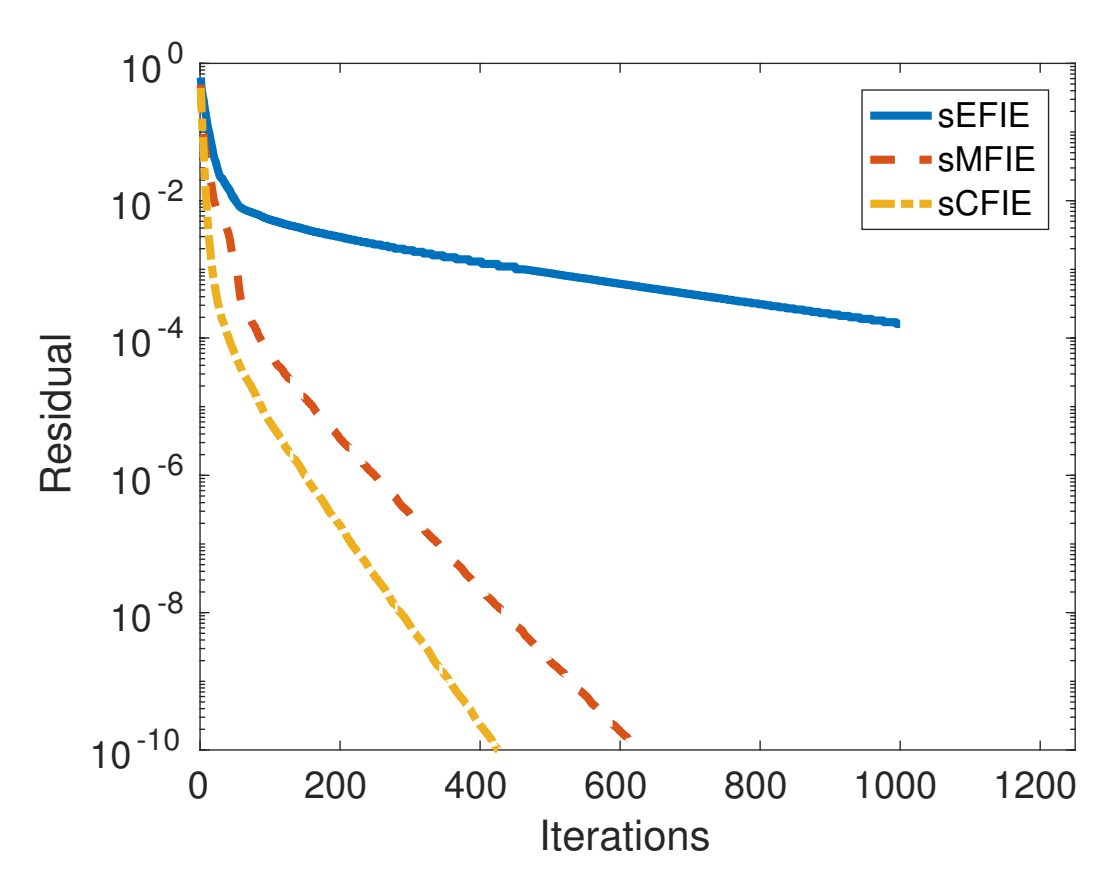


Figure 5.8: Residual of GMRES Iterations, 600Mhz

Figure 5.9. Actual changes in the residual of the iterative solver (as mentioned previously, no preconditioner is used for the GMRes solver) at different frequencies are given in Figure 5.10. Wide frequency stability in the iterative solvers can be observed, thanks to the spectral properties discussed earlier.

5.5 Conclusion

In this chapter, a new well-conditioned scalar charge based formulation has been presented to model the EM scattering from simply-connected structures. It is noted that fundamental unknowns are chosen similarly as in [91]. The the current representation J and electrical charge representation ρ are physical in this work, whereas they are not physical in [91] because the indirect approach is used therein. The formulation features wide-band stability in terms of spectral properties and conditioning of the resulting system. The ad-

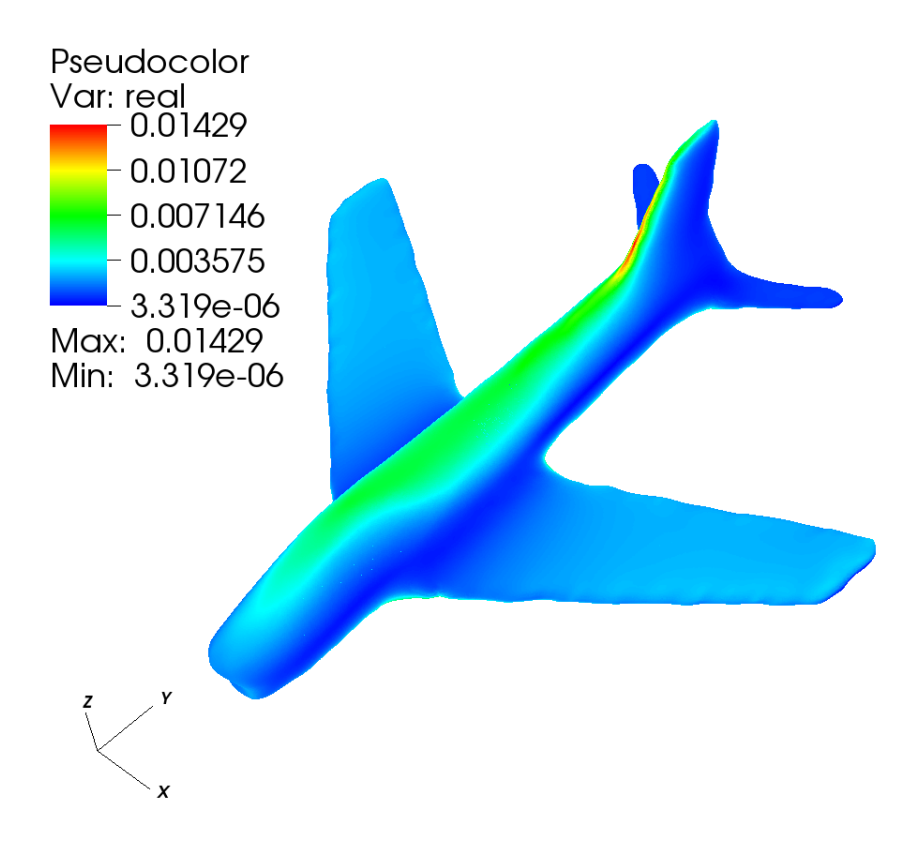


Figure 5.9: A plane model: real part of the magnitude of the surface current density

vantage of this formulation in terms of implementation and potential integration with higher order CAD descriptions is that it involves scalar basis functions; as shown, this enables easy implementation within an iso-geometric analysis framework via subdivision surfaces or spline surfaces. We anticipate that the methods developed herein wherein the description of the geometry and the physics on the geometry are intimately related would be of substantial use to the engineering community; this is the direction of our future research. Another important and non-trivial extension of the current formulation to multiply connected shapes will be discussed in future communications.

This chapter, ©2018 IEEE, is reprinted, with permission, from Li, J., Fu, X. and Shanker, B., "Formulation and Iso-Geometric Analysis of Scalar Integral Equations for Electromagnetic Scattering," Antennas and Propagation, IEEE Transactions on, April 2018.

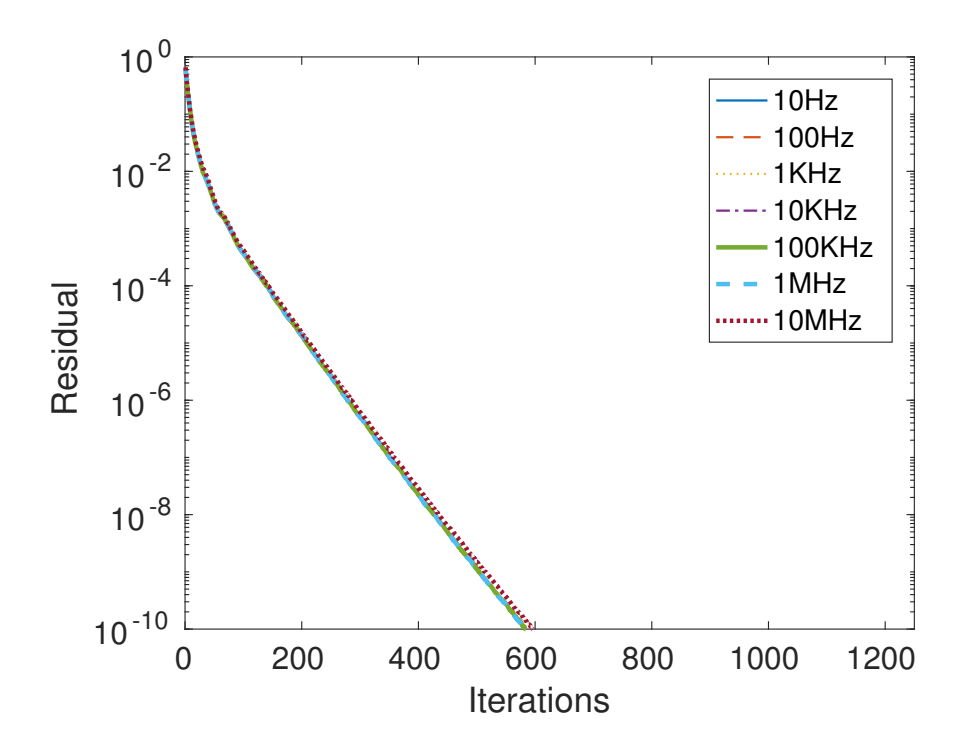


Figure 5.10: Residual of GMRES iterations at different frequencies

CHAPTER 6

DECOUPLED POTENTIAL BASED FORMULATIONS

6.1 Introduction

Surface integral equation methods have been widely used for the analysis of electromagnetic (EM) scattering and radiation [101, 120–122]. Commonly used integral equations for perfectly electrical conductors (PECs) include electric field integral equation (EFIE), magnetic integral equation (MFIE) and combined field integral equation (CFIE) and their modified forms [101]. For the problem of electromagnetic scattering from dielectric objects (transmission problem), the Poggio-Miller-Chang-Harrington-Wu-Tsai (PMCHWT) [121] and Müller formulations [122] are most popular ones. Issues such as low-frequency breakdown [87, 104], dense mesh breakdown [123] and topology breakdown [124] have been observed in numerical implementations of method of moments when solving these integral equations. Much of the breakdown phenomenon arises from either catastrophic cancellation, choosing different types of boundary conditions or badly imposed scalings. Direct consequence of the breakdown is ill-conditioning (hence poor convergence of iterative solvers) in the resulting linear system or lost accuracy in post-processing. Stabilizing existing integral equations solvers or designing new stable formulation has been extensively studied by the computational electromagnetics and applied mathematics communities; see Refs. [5, 97, 98, 101, 105, 108, 110, 112, 125–128] and references therein for a complete analysis.

Approaches for stabilizing the EFIE or its related incarnations range from loop-tree/star decomposition [87, 98, 105] (approximate Helmholtz decomposition) to constrained [129] and rigorous [5] Helmholtz decompositions. Remedies for dense mesh breakdown includes Calderon preconditioning [97, 123, 125] and quasi-Helmholtz projector-based methods [110]. All of the aforementioned methods work directly on the ill-conditioned integral equations. More recently, there has also been an effort to develop new or modify existing formulations.

Augmented EFIE (AEFIE) [126,127] is used to fix the low-frequency breakdown by introducing auxiliary charge terms and continuity constraints. The current-charge integral equation (CCIE) [108] is very similar to AEFIE but it can be used to develop a second kind integral equation for analyzing scattering from dielectric objects. Another example of recent work in this area is the scalar formulations including generalized Debye sources [91,112] or scalar charge EFIE and MFIE for simply connected structures [128].

The decoupled potential-based approach [103, 130, 131] is a very recent effort to solve the low-frequency breakdown problem. Besides its application to addressing breakdown associated with the low-frequencies, the scalar and vector potential approach can potentially be applied to simulations that use vector potential directly [103, 130] as opposed to the electric/magnetic fields. To date, new boundary conditions on the vector and scalar potentials have been developed so as to describe scattering from perfect electrically conducting (PEC) bodies [103,130,131]. In [103], a second kind integral equation was constructed based on the indirect approach, and the formulation presented is well-conditioned in that it does not suffer from either the low-frequency or dense mesh breakdown. Additionally, it does not have any spurious resonance issues or suffer from topology breakdown. The integral equation solved in [131] is not the second kind, but one that behaves like the AEFIE. An effort to address well-conditioned equations for dielectric objects using the DPIE framework is more recent, and focuses on further developing and fleshing out ideas presented in [4, 132]. Analysis of dielectric objects is more complex simply because more unknowns are involved. Another challenge is choosing suitable unknowns and observables. These are the challenges that we will address in this chapter; the formulation presented is well-conditioned, is not susceptible to non-uniqueness due to resonances or breakdown due to either low-frequencies or dense meshes. Specifically, in this chapter, we will present:

 Decoupled boundary conditions in terms of scalar and vector potential for transmission problems,

- well-conditioned scalar and vector potential integral equations for EM scattering from homogeneous dielectric objects,
- reduced decoupled integral equations for PEC problems,
- and, a study of the analytical properties of the resulting system to demonstrate features of the proposed integral equation framework.

The remainder of the paper is organized as follows. Section 6.2 gives preliminary information on the classical boundary value problem for EM scattering by dielectric objects. A new description for the scattering problem is introduced in Section 6.3 involving decoupled boundary value problems. Sections 6.4 presents the decoupled boundary conditions. Section 6.5 formulates the scalar and vector potential integral equations for the transmission problem. In Section 6.6, the analytical properties of the presented integral equations are studied with the help of asymptotic analysis. Section 6.8 provides some numerical results on the resulting linear system for a sphere. Finally, conclusions and related remarks are given in Section 6.9.

6.2 preliminaries

Consider a homogeneous dielectric object occupying a volume Ω_2 that is immersed in a homogeneous background Ω_1 . Let the surface enclosing the domain Ω_2 be denoted by S and equipped with a normal \mathbf{n} that points into Ω_1 . An electromagnetic plane wave characterized by $\{\mathbf{E}^i(\mathbf{r}), \mathbf{H}^i(\mathbf{r})\}$ is incident on the object. Each domain is characterized by a set of constitutive parameters, permittivity ϵ_i , permeability μ_i and wavenumber k_i for i=1,2. Henceforth, field quantities in domain Ω_i will be denoted using the subscript i. For the purpose of normalization, the permittivity, permeability, and wavenumber in free space are denoted by ϵ_0 , μ_0 and k_0 . The problem to be solved can be posed as follows: Given the scatterer configuration as described, find the total field $(\mathbf{E}^t(\mathbf{r}))$ and $(\mathbf{E}^t(\mathbf{r}))$ in each region Ω_i that comprises incident field $(\mathbf{E}^i_i(\mathbf{r}))$ or $\mathbf{H}^i_i(\mathbf{r})$ and scattered field $(\mathbf{E}^s_i(\mathbf{r}))$ or $\mathbf{H}^s_i(\mathbf{r})$.

The solution will be given through an integral equation approach which exploits equivalent sources on the surface that can be used to express the scattered field in Ω_i . In this chapter, a time-harmonic factor $e^{j\omega t}$ will be used and suppressed, and spatial dependence on \mathbf{r} will be assumed.

To derive the surface integral equation for the scattering problem, the Stratton-Chu representation for \mathbf{E}_i^s and \mathbf{H}_i^s can be used. Specifically,

$$\mathbf{E}_{i}^{s} = -j\omega\mu\mathcal{S}_{k_{i}}[\mathbf{J}_{i}] + \frac{1}{j\omega\epsilon}\nabla\mathcal{S}_{k_{i}}[\nabla_{s}'\cdot\mathbf{J}_{i}] - \nabla\times\mathcal{S}_{k_{i}}[\mathbf{M}_{i}]$$
(6.1)

$$\mathbf{H}_{i}^{s} = -j\omega\epsilon \mathcal{S}_{k_{i}}[\mathbf{M}_{i}] + \frac{1}{j\omega\mu} \nabla \mathcal{S}_{k_{i}}[\nabla_{s}' \cdot \mathbf{M}_{i}] + \nabla \times \mathcal{S}_{k_{i}}[\mathbf{J}_{i}]$$
(6.2)

In the previous representations, the notation for single layer potential operator is used, which is defined as

$$S_k[x](\mathbf{r}) = \int_S G_k(\mathbf{r}, \mathbf{r}') x(\mathbf{r}') dS', \tag{6.3}$$

with the integral path defined as enclosing the object. $G_k(\mathbf{r}, \mathbf{r'})$ denotes the Green's function for Helmholtz equation in free space (with k being the appropriate value corresponding to the host medium), and

$$G_k(\mathbf{r}, \mathbf{r}') = \frac{e^{-jk|\mathbf{r} - \mathbf{r}'|}}{4\pi|\mathbf{r} - \mathbf{r}'|}$$
(6.4)

The integral operators involve ${\bf J}_1={\bf n}\times{\bf H}_1$ (${\bf J}_2=-{\bf n}\times{\bf H}_2$) and ${\bf M}_1={\bf E}_1\times{\bf n}$ (${\bf M}_2=-{\bf E}_2\times{\bf n}$) as the sources for the radiation field in the exterior (interior) domain. ${\bf J}_1=-{\bf J}_2$ and ${\bf M}_1=-{\bf M}_2$ can be considered as the boundary conditions for tangential components required to formulate classical integral equations as discussed later.

The two types of sources are the equivalent electric and magnetic current densities, respectively. Based on the equivalence theorem, formulations like PMCHWT, Müller or combined field formulations can be derived that involve constructing integral equations associated with each domain and then imposing the requisite boundary conditions. The manner in which boundary conditions are used dictates the eventual formulation and its behavior in different frequency and discretization regimes. For the classical PMCHWT and Müller formulations, two unknown equivalent current sources are used, two boundary conditions that relate these

across boundaries are chosen, which then produce two different integral equations. This approach is called direct approach, in contrast to the indirect approach that starts from the boundary condition and then prepares well-chosen integral representations that usually involve quantities with nonphysical meaning [111,133].

Another type of integral equation for dielectric objects is based on current and charge unknowns [108], which introduces charge density in place of surface divergence of current densities. In that case, integrands in those operators include electric current, magnetic current, electric charge and magnetic charge, the unknown surface sources to be solved. As there are additional unknowns, one needs additional constraints on the system (in this case, the total number of constraints is four). To obtain these four equations, additional boundary conditions are imposed on the normal components of electromagnetic fields. Therefore, the following set of boundary conditions, will be used to set up the four integral equation, together with extra continuity and charge neutrality constraints:

$$\mathbf{n} \times \mathbf{E}_{1} = \mathbf{n} \times \mathbf{E}_{2}$$

$$\mathbf{n} \times \mathbf{H}_{1} = \mathbf{n} \times \mathbf{H}_{2}$$

$$\epsilon_{1} \mathbf{n} \cdot \mathbf{E}_{1} = \epsilon_{2} \mathbf{n} \cdot \mathbf{E}_{2}$$

$$\mu_{1} \mathbf{n} \cdot \mathbf{H}_{1} = \mu_{2} \mathbf{n} \cdot \mathbf{H}_{2}$$

$$(6.5)$$

In the next Section, we present a modified description of the problem based on the two commonly used potentials, one scalar and the other vector. The new boundary value problem will comprise a set of two decoupled boundary value problems.

6.3 Representations of the Decoupled Potential

6.3.1 Scalar and Vector Potentials

The starting point of our discussion is the well-known representation of the electric and magnetic fields in terms of the vector and scalar potentials, viz.,

$$\mathbf{E}_i = -j\omega \mathbf{A}_i - \nabla \Phi_i \tag{6.6}$$

$$\mathbf{H}_i = \frac{1}{\mu_i} \nabla \times \mathbf{A}_i \tag{6.7}$$

The governing partial differential equation (PDE) for the scalar potential Φ_i is the scalar Helmholtz equation

$$\left(\nabla^2 + k_i^2\right)\Phi_i(\mathbf{r}) = 0,\tag{6.8}$$

and the PDE for the vector potential \mathbf{A}_i is the vector Helmholtz equation

$$\left(\nabla^2 + k_i^2\right) \mathbf{A}_i(\mathbf{r}) = 0. \tag{6.9}$$

In the above equations, we have implicitly assumed that the Lorenz gauge is used. Using the above expressions, one obtains the boundary conditions in terms of the two potentials. Besides the radiation condition at infinity, the *coupled* description for the boundary conditions is as follows:

$$\mathbf{n} \times (-j\omega \mathbf{A}_{1} - \nabla \Phi_{1}) = \mathbf{n} \times (-j\omega \mathbf{A}_{2} - \nabla \Phi_{2})$$

$$\frac{1}{\mu_{1}} \mathbf{n} \times \nabla \times \mathbf{A}_{1} = \frac{1}{\mu_{2}} \mathbf{n} \times \nabla \times \mathbf{A}_{2}$$

$$\epsilon_{1} \mathbf{n} \cdot (-j\omega \mathbf{A}_{1} - \nabla \Phi_{1}) = \epsilon_{2} \mathbf{n} \cdot (-j\omega \mathbf{A}_{2} - \nabla \Phi_{2})$$

$$\mathbf{n} \cdot \nabla \times \mathbf{A}_{1} = \mathbf{n} \cdot \nabla \times \mathbf{A}_{2}$$

$$(6.10)$$

It's worth noting that the \mathbf{A} - Φ representation will lead to the same description of the original problem thanks to the Lorenz gauge. Though another similar pair of potentials, the electric vector potential (anti-potential) \mathbf{F} and magnetic scalar potential Ψ , are used when deriving formulations for dielectric objects, they have been used mainly for notational purpose only—to express integral operators involving magnetic currents and their divergence. Therefore, while we note the existence of a dual potential representation, neither this dual integral representation of fields no the use of the dual sources associated with these representations is used here. Such an alternative representation can be constructed using duality principles and eventually arrives at equations dual to (6.10). As an aside, one can use the pair \mathbf{F} - Ψ instead of \mathbf{A} - Φ to represent electric and magnetic fields. The steps for deriving decoupled potential integral equations for \mathbf{F} - Ψ are then dual to those for \mathbf{A} - Φ . As shown later, different components (trace information) of \mathbf{A} and Φ will be used as unknown sources in the

representations for them, and all the EM field quantities can be obtained through (6.6) and (6.7).

6.3.2 Representation of Scattering Potential

Using the Green's identity and the governing Helmholtz equation, the scattered scalar potential (denoted with superscript "s") representation could be written as

$$\Phi^{s}(\mathbf{r}) = -\mathcal{S}_{k} \left[\frac{\partial \Phi(\mathbf{r}')}{\partial n'} \right] + \mathcal{D}_{k} \left[\Phi(\mathbf{r}') \right]$$
(6.11)

where the double layer potential operator is defined as

$$\mathcal{D}_{k}[x](\mathbf{r}) = \int_{S} \frac{\partial G(\mathbf{r}, \mathbf{r}')}{\partial n'} x(\mathbf{r}') dS'$$
(6.12)

In the vector potential case, the dyadic Green's function can be written as

$$\bar{\mathbf{G}}(\mathbf{r}, \mathbf{r}') = \bar{\mathbf{I}} \frac{e^{-jk|\mathbf{r} - \mathbf{r}'|}}{4\pi|\mathbf{r} - \mathbf{r}'|} = \bar{\mathbf{I}}G(\mathbf{r}, \mathbf{r}')$$
(6.13)

With the Helmholtz equation and the Green's identity, $\mathbf{A}^{s}(\mathbf{r})$ can be represented as [130]

$$\mathbf{A}^{s} = \mathcal{S}_{k}[\mathbf{n}' \times \nabla' \times \mathbf{A}(\mathbf{r}')] + \nabla \times \mathcal{S}_{k}[\mathbf{n}' \times \mathbf{A}(\mathbf{r}')]$$

$$- \nabla \mathcal{S}_{k}[\mathbf{n}' \cdot \mathbf{A}(\mathbf{r}')] - \mathcal{S}_{k}[\mathbf{n}' \nabla' \cdot \mathbf{A}(\mathbf{r}')]$$
(6.14)

where there are four types of surface sources, associated with the total vector potential $\mathbf{A} = \mathbf{A}^i + \mathbf{A}^s$, to express the scattered vector potential. For notational simplicity, the following are used to denote surface sources that will be the unknown quantities in the integral equations derived later;

$$\mathbf{a}(\mathbf{r}) = \mathbf{n} \times \nabla \times \mathbf{A}(\mathbf{r}) \tag{6.15a}$$

$$\mathbf{b}(\mathbf{r}) = \mathbf{n} \times \mathbf{n} \times \mathbf{A}(\mathbf{r}) \tag{6.15b}$$

$$\gamma(\mathbf{r}) = \mathbf{n} \cdot \mathbf{A}(\mathbf{r}) \tag{6.15c}$$

$$\sigma(\mathbf{r}) = \nabla \cdot \mathbf{A}(\mathbf{r}) \tag{6.15d}$$

where ∇ is the 3D volume gradient operator. Using this notation, the integral representation of vector potential is rewritten as

$$\mathbf{A}^{s} = \mathcal{S}_{k}[\mathbf{a}] - \nabla \times \mathcal{S}_{k}[\mathbf{n}' \times \mathbf{b}] - \nabla \mathcal{S}_{k}[\gamma] - \mathcal{S}_{k}[\mathbf{n}'\sigma]$$
(6.16)

6.4 Decoupled Boundary Conditions

In this section, boundary conditions for the scalar potential and the vector potential will be derived. The development of these models will imitate success in framework used in both the Poggio-Miller-Chu-Harrington-Wu-Tsai (PMCHWT) and the Müller formulations wherein one poses the problems in terms of boundary conditions based on surface sources in associated operators in (6.11) and (6.14). To develop similar equations for the potentials it follows that one needs to set up boundary conditions on the scalar potential and its normal derivatives across the interface, so that one can set up two integral equations with two unknowns. Likewise, for vector potentials, one needs to impose four boundary conditions (two vector ones and two scalar ones) to be able to formulate four integral equations to solve the four unknown sources.

Next, although both [103] and [130] cover the PEC case, we will include a brief review and discussion for completeness.

6.4.1 Decoupled Boundary Conditions for the PEC case

For the PEC, one should have

$$\mathbf{n} \times (-j\omega \mathbf{A}_1 - \nabla \Phi_1) = 0 \tag{6.17a}$$

$$\mathbf{n} \cdot \frac{1}{\mu} \nabla \times \mathbf{A}_1 = 0 \tag{6.17b}$$

From (6.17a), a decoupled potential description of the boundary condition can be derived as

$$\mathbf{n} \times \mathbf{A}_1 = 0 \tag{6.18a}$$

$$\mathbf{n} \times \nabla \Phi_1 = 0 \tag{6.18b}$$

which is stronger than the original boundary condition.

To satisfy (6.18b), $\nabla_s \Phi_1 = 0$ has to be satisfied, which means the surface gradient of total scalar potential should vanish. Surface gradient data is not commonly used as a source, so another condition is used.

$$\Phi_1 = V_0 \tag{6.19}$$

where V_0 denotes a reference potential value. Both (6.18a) and (6.19) are used in both [103] and [130]. The difference is that [103] allows an extra set of DoFs to deal with the reference potential, whereas [130] does not deal with this (setting V_1 to zero).

One last but very interesting and important point about the PEC case is that the condition imposed by (6.17b) can be satisfied if (6.18a) holds. The proof is very straightforward, if the following manipulation is used:

$$\mathbf{n} \cdot (\nabla \times \mathbf{A}) = -\nabla \cdot (\mathbf{n} \times \mathbf{A}) \tag{6.20}$$

with $\nabla \times \mathbf{n} = 0$ being applied.

6.4.2 Decoupled Boundary Conditions for Dielectric Case

In the PEC case, finding the new boundary conditions involving both vector and scalar potentials is relatively straightforward. However, for the dielectric case, conditions on normal component quantities have to be satisfied, together with the requirement on tangential components of electromagnetic fields. A stronger boundary condition set (involving two potentials) has to be derived from the boundary condition on $\mathbf{n} \cdot \mathbf{E}$ (rather than $\mathbf{n} \cdot \mathbf{H}$). This anti-duality comes from the asymmetric nature of representations of \mathbf{E} and \mathbf{H} in (6.6) and

(6.7). Therefore, a new boundary condition set derived from (6.10) is as follows [130]:

$$\mathbf{n} \times \mathbf{A}_1 = \mathbf{n} \times \mathbf{A}_2 \tag{6.21a}$$

$$\mathbf{n} \times \nabla \Phi_1 = \mathbf{n} \times \nabla \Phi_2 \tag{6.21b}$$

$$\frac{1}{\mu_1} \mathbf{n} \times \nabla \times \mathbf{A}_1 = \frac{1}{\mu_2} \mathbf{n} \times \nabla \times \mathbf{A}_2 \tag{6.21c}$$

$$\epsilon_1 \mathbf{n} \cdot \mathbf{A}_1 = \epsilon_2 \mathbf{n} \cdot \mathbf{A}_2 \tag{6.21d}$$

$$\epsilon_1 \mathbf{n} \cdot \nabla \Phi_1 = \epsilon_2 \mathbf{n} \cdot \nabla \Phi_2 \tag{6.21e}$$

where the first two conditions are derived from the condition on $\mathbf{n} \times \mathbf{E}$ as in PEC case, the third one corresponds to the requirement on $\mathbf{n} \times \mathbf{H}$, and the last two are related with the conditions of normal components of the electric field. Similar to the PEC case, the requirement on the normal component of \mathbf{H} can be satisfied by considering the fact that $\mathbf{n} \cdot (\nabla \times \mathbf{X}) = -\nabla \cdot (\mathbf{n} \times \mathbf{X})$.

By separating vector potential \mathbf{A} and scalar potential Φ , and also introducing a constant jump term in Φ , one obtains the modified boundary conditions

$$\Phi_1 = \Phi_2 + V_1 \tag{6.22a}$$

$$\epsilon_1 \mathbf{n} \cdot \nabla \Phi_1 = \epsilon_2 \mathbf{n} \cdot \nabla \Phi_2 \tag{6.22b}$$

for the scalar potential Φ , where V_1 denotes a reference potential value, and boundary conditions

$$\mathbf{n} \times \mathbf{A}_1 = \mathbf{n} \times \mathbf{A}_2 \tag{6.23a}$$

$$\frac{1}{\mu_1} \mathbf{n} \times \nabla \times \mathbf{A}_1 = \frac{1}{\mu_2} \mathbf{n} \times \nabla \times \mathbf{A}_2 \tag{6.23b}$$

$$\epsilon_1 \mathbf{n} \cdot \mathbf{A}_1 = \epsilon_2 \mathbf{n} \cdot \mathbf{A}_2 \tag{6.23c}$$

for the vector potential.

At this point, only three boundary conditions are recovered for the vector potential, so another scalar boundary condition is required. The last one is the implicitly imposed condition that $\nabla \cdot \mathbf{E}$ vanishes; this condition on \mathbf{E} provides the necessary information on the divergence of \mathbf{A} and Φ , as

$$\nabla \cdot \mathbf{E} = -j\omega \nabla \cdot \mathbf{A} - \nabla^2 \Phi = -j\omega \nabla \cdot \mathbf{A} + k^2 \Phi = 0$$
 (6.24)

from the Lorenz gauge. Due to (6.22a), the additional boundary condition associated with the vector potential is $\nabla \cdot \mathbf{A}_1 = \nabla \cdot \mathbf{A}_2 + V_2$, where V_2 is a reference scalar (potential) that is constant over the surface of a isolated object. The two surface reference potentials (reference voltages) can be chosen as unknown quantities to be solved.

For the electromagnetic problem, the charge neutrality constraint has to be imposed as well. This requirement can be satisfied by setting up stronger conditions on both scalar and vector potential. The idea is to impose zero-mean constraints on both $\mathbf{n} \cdot \nabla \Phi$ and $\mathbf{n} \cdot \mathbf{A}$. These two requirements come directly from examining the physics of the problem and match a mathematical approach used in [103]. Using the afore-developed conditions, the boundary condition set for scalar potential would be written as follows:

$$\Phi_1 = \Phi_2 + V_1 \tag{6.25a}$$

$$\epsilon_1 \mathbf{n} \cdot \nabla \Phi_1 = \epsilon_2 \mathbf{n} \cdot \nabla \Phi_2 \tag{6.25b}$$

$$\int_{S} \frac{\partial \Phi_1}{\partial n'} dS' = 0 \tag{6.25c}$$

For vector potential, one would get

$$\mathbf{n} \times \mathbf{A}_1 = \mathbf{n} \times \mathbf{A}_2 \tag{6.26a}$$

$$\frac{1}{\mu_1} \mathbf{n} \times \nabla \times \mathbf{A}_1 = \frac{1}{\mu_2} \mathbf{n} \times \nabla \times \mathbf{A}_2 \tag{6.26b}$$

$$\epsilon_1 \mathbf{n} \cdot \mathbf{A}_1 = \epsilon_2 \mathbf{n} \cdot \mathbf{A}_2 \tag{6.26c}$$

$$\nabla \cdot \mathbf{A}_1 = \nabla \cdot \mathbf{A}_2 + V_2 \tag{6.26d}$$

$$\int_{S} \mathbf{n} \cdot \mathbf{A}_1 dS' = 0 \tag{6.26e}$$

Due to the gauge freedom, it is known that **E-H** cannot uniquely determine \mathbf{A} - Φ , whereas the reverse is true. Following the same philosophy (choosing specific boundary value descriptions involving \mathbf{A} - Φ to represent the Maxwell's boundary value problem), one can also use an even stronger constraint by setting the reference terms V_1 and V_2 to zero. It can be shown that for this choice the solutions to (6.25) and (6.26) are unique and do not admit any gauge nullspaces. In the rest of the paper, the formulation and discussions presented later are under this assumption. Though solutions satisfy the Maxwell's equation with the scalar and potentials being auxiliary quantities, effects of the assumption on the true vector or scalar potential problem are not known and worth being studied to answer a more fundamental question—whether a description using scalar-vector potential \mathbf{A} - Φ rather than \mathbf{E} - \mathbf{H} is possible [134, 135]. If a potential-only description is possible, then there is another open problem: can we derive an additional physics-based constraint to augment (6.25) and (6.26) such that they admit unique solutions without setting the reference terms V_1 and V_2 to zero.

It's worth noting that several pairs of the decoupled potential boundary conditions such as (6.22a) and (6.23a) are much stronger than their electric and magnetic fields counterparts (6.10). This is a fundamental assumption in all of the existing decoupled potential-based formulations. If the solution satisfies the decoupled boundary value problem, then the solution is also the solution to the original Maxwell's equations. The existence and uniqueness of the decoupled potential-based boundary value problems are essential to set up the decoupled potential integral equations; see discussions in [103, 132].

6.5 Formulation of Decoupled Potential Integral Equations

In this section, decoupled potential integral equations will be derived based on the representation theorems and corresponding decoupled boundary condition sets.

6.5.1 Scalar Potential Integral Equation (SPIE)

From the representation theorem for scalar potentials, one can choose Φ and its normal derivative $\frac{\partial \Phi}{\partial n}$ as the sources and observables to construct the integral equations. Therefore, one needs the information about the two corresponding incident fields, denoted by $\Phi^i(\mathbf{r})$ and $\frac{\partial \Phi^i(\mathbf{r})}{\partial n}$ respectively.

On the surface, two integral equations corresponding to the exterior and interior domain can be written as follows.

$$\Phi_1 = \Phi^i - \mathcal{S}_{k_1} \left[\frac{\partial \Phi_1(\mathbf{r}')}{\partial n'} \right] + \mathcal{D}_{k_1} \left[\Phi_1(\mathbf{r}') \right]$$
 (6.27a)

$$\Phi_2 = \mathcal{S}_{k_2} \left[\frac{\partial \Phi_2(\mathbf{r}')}{\partial n'} \right] - \mathcal{D}_{k_2} \left[\Phi_2(\mathbf{r}') \right]$$
 (6.27b)

In the integrals of the first (second) IE, the observation point approaches the surface from the exterior (interior) domain. Usually, Cauchy principal values will be taken when working with operators with singularity order higher than $\frac{1}{R}$.

One needs another two singular integral equations to have the same number of equations as the unknowns.

$$\frac{\partial \Phi_1}{\partial n} = \frac{\partial \Phi^i}{\partial n} - \mathcal{D}'_{k_1} \left[\frac{\partial \Phi_1(\mathbf{r}')}{\partial n'} \right] + \mathcal{N}_{k_1} \left[\Phi_1(\mathbf{r}') \right]$$
 (6.28a)

$$\frac{\partial \Phi_2}{\partial n} = \mathcal{D}'_{k_2} \left[\frac{\partial \Phi_2(\mathbf{r}')}{\partial n'} \right] - \mathcal{N}_{k_2} \left[\Phi_1(\mathbf{r}') \right]$$
 (6.28b)

where the normal derivatives of operators \mathcal{S}_k and \mathcal{D}_k are denoted by \mathcal{D}'_k and \mathcal{N}_k respectively.

By linearly combining the two equations in (6.27) and the two equations in (6.28) and applying the boundary conditions in (6.25), one obtains the following scalar potential integral equation (SPIE):

$$\begin{pmatrix}
\frac{\alpha_1 + \alpha_2}{2} \mathcal{I} + \mathcal{C}_{11} & \mathcal{C}_{12} \\
\mathcal{C}_{21} & \frac{\beta_1 + \beta_2}{2} \mathcal{I} + \mathcal{C}_{22}
\end{pmatrix}
\begin{pmatrix}
\Phi \\
\frac{\epsilon_1}{k_0 \epsilon_0} \frac{\partial \Phi}{\partial n}
\end{pmatrix} = \begin{pmatrix}
\Phi^i \\
\frac{\epsilon_1}{k_0 \epsilon_0} \frac{\partial \Phi^i}{\partial n}
\end{pmatrix}$$
(6.29)

where the scale factor $\frac{\epsilon_1}{k_0\epsilon_0}$ on the $\frac{\partial\Phi}{\partial n}$ is used to get the same dimensionality as in Φ and

$$C_{11} = -\alpha_1 \tilde{\mathcal{D}}_{k_1} + \alpha_2 \tilde{\mathcal{D}}_{k_2}, \tag{6.30a}$$

$$C_{12} = \frac{\alpha_1 k_0 \epsilon_0}{\epsilon_1} S_{k_1} - \frac{\alpha_2 k_0 \epsilon_0}{\epsilon_2} S_{k_2}, \tag{6.30b}$$

$$C_{21} = -\frac{\beta_1 \epsilon_1}{k_0 \epsilon_0} \mathcal{N}_{k_1} + \frac{\beta_2 \epsilon_2}{k_0 \epsilon_0} \mathcal{N}_{k_2}, \tag{6.30c}$$

$$C_{22} = \beta_1 \tilde{\mathcal{D}}'_{k_1} - \beta_2 \tilde{\mathcal{D}}'_{k_2}. \tag{6.30d}$$

In (6.30) and equations later, operators with tildes mean the integral is taken in the Cauchy principal value sense. Following a similar manner as in the Müller system of equations, the constraint $\beta_1 \epsilon_1 = \beta_2 \epsilon_2$ has to be imposed in order to remove the hyper-singularity in \mathcal{C}_{21} . The impact of choices of other parameters on invertibility and actual conditioning is worth being studied theoretically and numerically, especially when lossy medium is involved. With that choice, all the operators are bounded and compact. Since the two operators in the diagonal in (6.30) are in the form of an identity operator plus compact operators (\mathcal{C}_{11} and \mathcal{C}_{22}) when the surface is smooth, the integral equation (6.30) is of the second kind.

6.5.2 Vector Potential Integral Equation (VPIE)

The vector potential integral equation corresponding to the vector potential boundary value problem can be derived in a manner similar to that used for the scalar potential, but it involves choosing suitable observables and different scalings.

Since the goal is to construct a well-conditioned formulation, it is very natural to choose the same set of trace information of the vector potential as the observables. As in the scalar potential case, incident field information including $\mathbf{n} \times \nabla \times \mathbf{A}^i$, $\mathbf{n} \times \mathbf{n} \times \mathbf{A}^i$, $\mathbf{n} \cdot \mathbf{A}^i$ and $\nabla \cdot \mathbf{A}^i$ must be available.

From (6.16), one can write the representations for the four types of observables in the following two sets (one for the exterior and the other for the interior) of integral equations. The first set is obtained by allowing the observation point to approach the surface from the exterior, yielding the following exterior vector potential integral equation (VPIE) set:

$$\begin{pmatrix}
\mathbf{a}_{1} \\
\mathbf{b}_{1} \\
\gamma_{1} \\
\sigma_{1}
\end{pmatrix} = \begin{pmatrix}
\mathbf{a}^{i} \\
\mathbf{b}^{i} \\
\gamma^{i} \\
\sigma^{i}
\end{pmatrix} + \begin{pmatrix}
\mathcal{K}_{k_{1}} & -\mathcal{T}_{k_{1}} & 0 & -\mathcal{Q}_{k_{1}}^{1} \\
\mathcal{S}_{k_{1}}^{t} & -\mathcal{K}_{k_{1}}^{\prime} & -\mathcal{P}_{k_{1}}^{2} & -\mathcal{Q}_{k_{1}}^{2} \\
\mathcal{S}_{k_{1}}^{r} & -\mathcal{M}_{k_{1}}^{3} & -\mathcal{D}_{k_{1}}^{\prime} & -\mathcal{Q}_{k_{1}}^{3} \\
\nabla \cdot \mathcal{S}_{k_{1}} & 0 & k_{1}^{2} \mathcal{S}_{k_{1}} & \mathcal{D}_{k_{1}}
\end{pmatrix} \begin{pmatrix}
\mathbf{a}_{1} \\
\mathbf{b}_{1} \\
\gamma_{1} \\
\gamma_{1} \\
\sigma_{1}
\end{pmatrix} (6.31)$$

The operators \mathcal{T} , \mathcal{K} and \mathcal{K}' , respectively, denote the electromagnetic hyper-singular operator, the MFIE operator and its adjoint operator. \mathcal{D} and \mathcal{D}' are scalar double layer potential

operator and its adjoint, respectively. Their explicit definitions and properties are given in the Appendix for completeness. The other operators in (6.31) are less well-known and are defined as follows:

$$\mathcal{M}_{k}^{3}[\mathbf{b}] = \mathbf{n} \cdot \nabla \times \mathcal{S}_{k}[\mathbf{n}' \times \mathbf{b}]$$

$$\mathcal{P}_{k}^{2}[\gamma] = \mathbf{n} \times \mathbf{n} \times \nabla \mathcal{S}_{k}[\gamma]$$

$$\mathcal{Q}_{k}^{1}[\sigma] = \mathbf{n} \times \nabla \times \mathcal{S}_{k}[\mathbf{n}'\sigma]$$

$$\mathcal{Q}_{k}^{2}[\sigma] = \mathbf{n} \times \mathbf{n} \times \mathcal{S}_{k}[\mathbf{n}'\sigma]$$

$$\mathcal{Q}_{k}^{3}[\sigma] = \mathbf{n} \cdot \mathcal{S}_{k}[\mathbf{n}'\sigma]$$

$$\mathcal{Q}_{k}^{3}[\sigma] = \mathbf{n} \cdot \mathcal{S}_{k}[\mathbf{n}'\sigma]$$
(6.32)

Among these, all the operators in the diagonal can be written in the form of identity plus a compact operator (as shown in the appendix). \mathcal{T}_k is a hyper-singular operator, and has the same properties as that of the EFIE. Each operator in the skew-diagonal is bounded but not compact.

A second, interior VPIE set is obtained by allowing the observation point to approach the surface from the interior. Using the same operator definitions as in (6.31) and (6.32), but with subscripts k_2 to denote use of the interior region wavenumber in the Green's function, the same notation can be used to express the observables as

$$\begin{pmatrix}
\mathbf{a}_{2} \\
\mathbf{b}_{2} \\
\gamma_{2} \\
\sigma_{2}
\end{pmatrix} = - \begin{pmatrix}
\mathcal{K}_{k_{2}} & -\mathcal{T}_{k_{2}} & 0 & -\mathcal{Q}_{k_{2}}^{1} \\
\mathcal{S}_{k_{2}}^{t} & -\mathcal{K}_{k_{2}}^{\prime} & -\mathcal{P}_{k_{2}}^{2} & -\mathcal{Q}_{k_{2}}^{2} \\
\mathcal{S}_{k_{2}}^{r} & -\mathcal{M}_{k_{2}}^{3} & -\mathcal{D}_{k_{2}}^{\prime} & -\mathcal{Q}_{k_{2}}^{3} \\
\nabla \cdot \mathcal{S}_{k_{2}} & 0 & k_{2}^{2} \mathcal{S}_{k_{2}} & \mathcal{D}_{k_{2}}
\end{pmatrix} \begin{pmatrix}
\mathbf{a}_{2} \\
\mathbf{b}_{2} \\
\gamma_{2} \\
\sigma_{2}
\end{pmatrix} \tag{6.33}$$

For convenience, Z_1 and Z_2 are used to denote the operator matrices in (6.31) and (6.33) respectively.

In order to simplify application of the boundary conditions and further improve the conditioning of the system, the following scaled quantities (as in scalar potential case) are

used. That is,

$$\mathbf{a'} = \frac{\sqrt{\mu_0}}{\mu} \mathbf{a} = \frac{\sqrt{\mu_0}}{\mu} \mathbf{n} \times \nabla \times \mathbf{A}$$
 (6.34a)

$$\mathbf{b'} = -j\omega\sqrt{\epsilon_0}\mathbf{b} = -j\omega\sqrt{\epsilon_0}\mathbf{n} \times \mathbf{n} \times \mathbf{A}$$
 (6.34b)

$$\gamma' = -\frac{j\omega\epsilon}{\sqrt{\epsilon_0}}\gamma = -\frac{j\omega\epsilon}{\sqrt{\epsilon_0}}\mathbf{n} \cdot \mathbf{A}$$
 (6.34c)

$$\sigma' = \frac{1}{\sqrt{\mu_0}}\sigma = \frac{1}{\sqrt{\mu_0}}\nabla \cdot \mathbf{A} \tag{6.34d}$$

A careful dimensional analysis shows that all the above quantities $(\mathbf{a}', \mathbf{b}', \gamma', \sigma')$ have the same units. It is not difficult to realize that the first three terms represent scaled electric current density, scaled tangential electric field and scaled electric charge density, whereas the last one is scaled potential. Hence the unknown quantities presented in this chapter can be related to physical quantities, which is an advantage of the direct approach over the indirect approach in setting up integral equations [101,111]. In light of this interpretation, the boundary conditions are tantamount to all the four fields being continuous across the interface. It is also worth noting that the first two unknowns are part of the scaled electric current and scaled tangential electric field. The presence of the other two quantities (one of them is a scaled charge density term), together with the suitable linear combination of equations for both domains, leads to stability properties as discussed later.

To reflect the changes in the scaling while keeping the identity operator unchanged, one can define the following block diagonal left and right preconditioners. Since later analysis will involve objects with electrical size kd, all of these scaling factors are written in terms of k_i , ϵ_i and/or μ_i , with i = 0, 1, 2 denoting free space, exterior medium and interior medium, respectively.

$$P_{l,i} = \operatorname{diag}(\frac{\sqrt{\mu_0}}{\mu_i}, -\frac{jk_0}{\sqrt{\mu_0}}, -\frac{jk_0\epsilon_i}{\epsilon_0\sqrt{\mu_0}}, \frac{1}{\sqrt{\mu_0}})$$
(6.35)

and

$$P_{r,i} = \operatorname{diag}(\frac{\mu_i}{\sqrt{\mu_0}}, -\frac{\sqrt{\mu_0}}{jk_0}, -\frac{\epsilon_0\sqrt{\mu_0}}{jk_0\epsilon_i}, \sqrt{\mu_0}).$$
 (6.36)

Thus the scaled form of the exterior VPIE (6.31) becomes

$$\begin{pmatrix} \frac{\mathcal{I}}{2} - \mathcal{Z}_1' \end{pmatrix} \begin{pmatrix} \mathbf{a}_1' \\ \mathbf{b}_1' \\ \gamma_1' \\ \sigma_1' \end{pmatrix} = P_{l,1} \begin{pmatrix} \mathbf{a}^i \\ \mathbf{b}^i \\ \gamma^i \\ \sigma^i \end{pmatrix}$$
(6.37)

where \mathcal{Z}'_1 denotes the new operator matrix after introducing Cauchy principal value integrals for the operators in the diagonal of $P_{l,1}\mathcal{Z}_1P_{r,1}$. Similarly, the scaled form of the interior VPIE (6.33) becomes

$$\left(\frac{\mathcal{I}}{2} + \mathcal{Z}_2'\right) \begin{pmatrix} \mathbf{a}_2' \\ \mathbf{b}_2' \\ \gamma_2' \\ \sigma_2' \end{pmatrix} = 0$$
(6.38)

The explicit form for \mathcal{Z}_i' (i=1,2) in (6.37) and (6.38) is

$$\begin{pmatrix}
\tilde{\mathcal{K}}_{k_{i}} & \frac{1}{jk_{0}\mu_{r}}\mathcal{T}_{k_{i}} & 0 & -\frac{1}{\mu_{r}}\mathcal{Q}_{k_{i}}^{1} \\
-jk_{0}\mu_{r}\mathcal{S}_{k_{i}}^{t} & -\tilde{\mathcal{K}}_{k_{i}}^{\prime} & -\frac{1}{\epsilon_{r}}\mathcal{P}_{k_{i}}^{2} & jk_{0}\mathcal{Q}_{k_{i}}^{2} \\
-\frac{jk_{0}}{c_{r}}\mathcal{S}_{k_{i}}^{r} & -\epsilon_{r}\mathcal{M}_{k_{i}}^{3} & -\tilde{\mathcal{D}}_{k_{i}}^{\prime} & jk_{0}\epsilon_{r}\mathcal{Q}_{k_{i}}^{3} \\
\mu_{r}\nabla \cdot \mathcal{S}_{k_{i}} & 0 & -\frac{k_{i}^{2}}{jk_{0}\epsilon_{r}}\mathcal{S}_{k_{i}} & \tilde{\mathcal{D}}_{k_{i}}
\end{pmatrix} (6.39)$$

where the relative light speed c_r is defined as $c_r = \frac{1}{\sqrt{\epsilon_r \mu_r}}$. By linearly combining the two VPIEs for exterior and interior domains, one obtains the final VPIE,

$$\left(\frac{Q_1 + Q_2}{2} - Q_1 \mathcal{Z}_1' + Q_2 \mathcal{Z}_2'\right) \begin{pmatrix} \mathbf{a}_1' \\ \mathbf{b}_1' \\ \gamma_1' \\ \sigma_1' \end{pmatrix} = Q_1 P_{l,1} \begin{pmatrix} \mathbf{a}^i \\ \mathbf{b}^i \\ \gamma^i \\ \sigma^i \end{pmatrix}$$
(6.40)

where the linear factors are defined by

$$Q_1 = \operatorname{diag}\left(\frac{1}{\mu_{r2}}, \frac{1}{\epsilon_{r2}}, \epsilon_{r2}, \mu_{r2}\right) \tag{6.41a}$$

$$Q_2 = \operatorname{diag}\left(\frac{1}{\mu_{r1}}, \frac{1}{\epsilon_{r1}}, \epsilon_{r1}, \mu_{r1}\right) \tag{6.41b}$$

The choice for linear factors is determined by requiring the cancellation of singularities beyond $\frac{1}{R}$, that is, to cancel the singularity in those non-compact operators as done in Müller formulation [122]. This particular linear combination not only has the advantage of eliminating non-compact operators for increased numerical stability, but of also allowing an expanded choice of basis and testing functions with considerably relaxed continuity/conformability requirements.

6.6 Analytical Properties

In this section, we investigate the analytical properties of the presented SPIE and VPIE by studying scattering from a sphere of radius a. The resulting linear system from both integrals can be analytically evaluated if scalar and vector spherical harmonics are used to represent the unknowns associated in each integral equation. Due to the orthogonality between basis functions, a block diagonal system will be generated, making it possible to study the spectral properties of the discrete system. This approach has been used widely as an efficient tool to understand/capture some of the essential signatures of integral operators associated with three-dimensional time harmonic or time-dependent acoustic or electromagnetic problems [2, 3, 51, 91, 103].

Unknown scalar (u) and vector (\mathbf{u}) quantities are represented using scalar and vector spherical harmonics [2] such that

$$u = \sum u_{nm} Y_n^m \tag{6.42}$$

$$\mathbf{u} = \sum u_{nm}^1 \mathbf{\Psi}_n^m + u_{nm}^2 \mathbf{\Phi}_n^m \tag{6.43}$$

where

$$Y_n^m(\theta, \Phi) = \sqrt{\frac{2n+1}{4\pi} \frac{(n-m)!}{(n+m)!}} P_n^m(\cos \theta) e^{jm\phi}$$
 (6.44)

$$\Psi_n^m(\theta,\phi) = \frac{r}{\sqrt{n(n+1)}} \nabla^t Y_n^m(\theta,\phi) = \frac{\tilde{\Psi}_n^m(\theta,\phi)}{\sqrt{n(n+1)}}$$
(6.45)

$$\mathbf{\Phi}_n^m(\theta,\phi) = \frac{r}{\sqrt{n(n+1)}}\hat{\mathbf{r}} \times \nabla^t Y_n^m(\theta,\phi) = \frac{\tilde{\mathbf{\Phi}}_n^m(\theta,\phi)}{\sqrt{n(n+1)}}$$
(6.46)

where r=a and $\hat{\mathbf{r}}$ is the unit vector pointing in the radial direction. The vector spherical harmonics satisfy the relations $\mathbf{\Psi}_{n}^{m}(\theta, \Phi) = -\hat{\mathbf{r}} \times \mathbf{\Phi}_{n}^{m}(\theta, \Phi)$ and $\mathbf{\Phi}_{n}^{m}(\theta, \Phi) = \hat{\mathbf{r}} \times \mathbf{\Psi}_{n}^{m}(\theta, \Phi)$. The linear system elements are evaluated as integrals of several types: (1) scalar-scalar integral $< Y_{n'}^{m'}, \mathcal{OP}[Y_{n}^{m}] >$, (2) scalar-vector integral $< Y_{n'}^{m'}, \mathcal{OP}[\mathbf{\Psi}_{n}^{m}(\mathbf{\Psi}_{n'}^{m})] >$, (3) vector-scalar integral $< \mathbf{\Psi}_{n'}^{m'}(\mathbf{\Psi}_{n'}^{m'}), \mathcal{OP}[Y_{n}^{m}] >$ and (4) vector-vector integral $< \mathbf{\Psi}_{n'}^{m'}(\mathbf{\Psi}_{n'}^{m'}), \mathcal{OP}[\mathbf{\Psi}_{n}^{m}(\mathbf{\Psi}_{n'}^{m})] >$, where \mathcal{OP} denotes an appropriate operator.

6.6.1 Stability Properties of SPIE

The scalar potential integral equation is well-conditioned and doesn't suffer from the dense mesh breakdown problem. The formulation for the scalar potential integral equation is similar to that for the transmission problem in acoustics [111], hence it is immune to spurious resonances. The detailed analysis will be not be presented; the analysis procedure is very similar to that for VPIE, which will be given next.

6.6.2 Stability Properties of VPIE

Except for the identity operators along the diagonal, the vector potential integral equation involves only compact operators. At high frequency, one should avoid allowing the system element to grow as ka. As $ka \to \infty$, the asymptotic behavior for the system elements in \mathcal{Z}'_i is of the following form:

$$a^{2} \begin{pmatrix} \frac{1}{2} & \frac{\sqrt{\mu_{r}\epsilon_{r}}}{\mu_{r}} & 0 & \frac{1}{\mu_{r}\sqrt{\epsilon_{r}\mu_{r}}} \\ \frac{\mu_{r}}{\sqrt{\mu_{r}\epsilon_{r}}} & \frac{1}{2} & \frac{1}{\epsilon_{r}\sqrt{\mu_{r}\epsilon_{r}}} & \mathcal{O}((ka)^{-2}) \\ \mathcal{O}((ka)^{-1}) & \frac{\epsilon_{r}}{\sqrt{\mu_{r}\epsilon_{r}}} & \frac{1}{2} & \frac{1}{\mu_{r}\sqrt{\epsilon_{r}\mu_{r}}} \\ \frac{\mu_{r}}{\sqrt{\mu_{r}\epsilon_{r}}} & 0 & \frac{\sqrt{\mu_{r}\epsilon_{r}}}{\epsilon_{r}} & \frac{1}{2} \end{pmatrix}$$

$$(6.47)$$

It should be noted that the asymptotic analysis focuses on ka, assuming the mesh resolution is proportional to the wavenumber set by the spatial Nyquist sampling rate (ka and mesh density approaching infinity at the same time is not practical in numerical analysis). As seen

from (6.47), in each row, operators in the off-diagonal have different scalings in terms of material properties, therefore it is not possible to have all the off-diagonal elements approach zero at the same time. Actually, numerical examples show that at high frequencies, due to the oscillatory nature of each operator, the spectral properties (such as eigenvalues and eigen-radius) for the system are also oscillatory.

At low frequencies, when $ka \to 0$, one should avoid terms such as $\mathcal{O}(\frac{1}{ka})$ that would lead to catastrophic cancellations. It is easy to find that $\frac{1}{jk_0\mu_r}\mathcal{T}_{k_i}$ in Z_i' has the same problem as regular EFIE. The situation can be easily fixed thanks to the fact that at very low frequencies, the electric and magnetic fields become decoupled. The frequency scaling in (6.35) and (6.36) should be removed be removed at low frequencies (i.e., sub-domains become electrically small), with the resulting system matrix modified to

$$\begin{pmatrix}
\tilde{\mathcal{K}}_{k_{i}} & \frac{1}{j\mu_{r}}\mathcal{T}_{k_{i}} & 0 & -\frac{1}{\mu_{r}}\mathcal{Q}_{k_{i}}^{1} \\
-j\mu_{r}\mathcal{S}_{k_{i}}^{t} & -\tilde{\mathcal{K}}_{k_{i}}^{\prime} & -\frac{1}{\epsilon_{r}}\mathcal{P}_{k_{i}}^{2} & j\mathcal{Q}_{k_{i}}^{2} \\
-\frac{j}{c_{r}}\mathcal{S}_{k_{i}}^{r} & -\epsilon_{r}\mathcal{M}_{k_{i}}^{3} & -\tilde{\mathcal{D}}_{k_{i}}^{\prime} & j\epsilon_{r}\mathcal{Q}_{k_{i}}^{3} \\
\mu_{r}\nabla \cdot \mathcal{S}_{k_{i}} & 0 & -\frac{k_{i}^{2}}{j\epsilon_{r}}\mathcal{S}_{k_{i}} & \tilde{\mathcal{D}}_{k_{i}}
\end{pmatrix} (6.48)$$

Low-frequency stability properties can be studied by looking at the asymptotic behavior as $ka \to 0$ for fixed resolution (indicated by fixing the highest mode degree n). The asymptotic scaling of \mathcal{Z}'_i in (6.48) behaves like

$$a^{2} \begin{pmatrix} \mathcal{O}(1) & \frac{1}{\mu_{r}} \mathcal{O}(1) & 0 & \frac{1}{\mu_{r}} \mathcal{O}(1) \\ 0 & \mathcal{O}(1) & \frac{1}{\epsilon_{r}} \mathcal{O}(1) & 0 \\ 0 & \epsilon_{r} \mathcal{O}(1) & \mathcal{O}(1) & 0 \\ \mu_{r} \mathcal{O}(1) & 0 & 0 & \mathcal{O}(1) \end{pmatrix}$$
(6.49)

where each of the $\mathcal{O}(1)$ terms is only in terms of spatial resolution parameter n, unit imaginary number j and possibly a, but shows no dependence on constitutive parameters. Apparently, after the frequency scaling, all the terms are bounded and no serious cancellation will occur. Furthermore, by choosing the linear combination factors as in (6.41), one obtains

vanishing off-diagonal elements in (6.40). It is worth noting that choosing correct boundary conditions for $\mathbf{b'}$ and σ' is essential to achieving this goal, because it leads to the same scaling factor in front of the second and fourth operators of the first row in (6.49). At low frequencies, the system is diagonally dominant.

Another important issue in EFIE or EFIE-like formulations is dense mesh breakdown when element size h is close to zero or the spatial resolution (mode degree) is very high. For fixed ka, the dependence of the system elements on spatial resolution n (proportional to $\frac{1}{h}$ in piecewise discretization) can be derived as

$$a^{2} \begin{pmatrix} \mathcal{O}(1/n) & \frac{1}{\mu_{r}} \mathcal{O}(n) & 0 & \frac{1}{\mu_{r}} \mathcal{O}(1) \\ 0 & \mathcal{O}(1/n) & \frac{1}{\epsilon_{r}} \mathcal{O}(1) & 0 \\ 0 & \epsilon_{r} \mathcal{O}(1) & \mathcal{O}(1/n) & 0 \\ \mu_{r} \mathcal{O}(1) & 0 & 0 & \mathcal{O}(1/n) \end{pmatrix}$$
(6.50)

Again, all the $\mathcal{O}(\cdot)$ terms are independent of the material constitutive coefficients that explicitly appear in front of the operators. From the asymptotic result, one sees that the only term that can possibly cause density breakdown is the hyper-singular operator. However, after combining two equations for both interior and exterior domain with the help of (6.41), all the $\mathcal{O}(1)$ and $\mathcal{O}(n)$ terms are canceled exactly at low frequencies, owing to the fact that the resulting operators in the off-diagonal are compact.

6.7 Perfectly Electrical Conductor Case

The presented formulation can be reduced to a simpler one for scattering analysis of PECs. In this section, several integral equations for PECs will be given briefly, and comparison will be made to results presented in [103, 130, 131].

Using the condition $\Phi = 0$, one can reduce the SPIE to an equation that has only Φ (and V_1 if necessary) as the unknown quantity,

$$S_{k_1}\left[\frac{\partial \Phi_1(\mathbf{r}')}{\partial n'}\right] = \Phi^i \tag{6.51}$$

where charge neutrality $\int \frac{\partial \Phi_1(\mathbf{r}')}{\partial n'} dS' = 0$ is imposed. The resulting formulation will suffer from spurious resonances; by combining the equation with its normal derivative (as in the Burton-Miller [136] approach), one can make the SPIE for PECs immune to spurious resonances. The indirect approach used in [101, 103] can be also used.

By setting $\mathbf{n} \times \mathbf{n} \times \mathbf{A}$ and $\nabla \cdot \mathbf{A}$ to zero, the VPIE in (6.31) is reduced to

$$\begin{pmatrix}
\mathbf{a}_{1} \\
0 \\
\gamma_{1} \\
0
\end{pmatrix} = \begin{pmatrix}
\mathbf{a}^{i} \\
\mathbf{b}^{i} \\
\gamma^{i} \\
\sigma^{i}
\end{pmatrix} + \begin{pmatrix}
\mathcal{K}_{k_{1}} & 0 \\
\mathcal{S}_{k_{1}}^{t} & -\mathcal{P}_{k_{1}}^{2} \\
\mathcal{S}_{k_{1}}^{r} & -\mathcal{D}_{k_{1}}' \\
\nabla \cdot \mathcal{S}_{k_{1}} & k_{1}^{2} \mathcal{S}_{k_{1}}
\end{pmatrix} \begin{pmatrix}
\mathbf{a}_{1} \\
\gamma_{1}
\end{pmatrix}$$
(6.52)

with two unknowns (\mathbf{a}_1 and γ_1) governed by four integral equations. There are several options for choosing two equations from them. One choice is to formulate a second kind integral equation,

$$\begin{pmatrix} \mathbf{a}_1 \\ \gamma_1 \end{pmatrix} - \begin{pmatrix} \mathcal{K}_{k_1} & 0 \\ \mathcal{S}_{k_1}^r & -\mathcal{D}_{k_1}' \end{pmatrix} \begin{pmatrix} \mathbf{a}_1 \\ \gamma_1 \end{pmatrix} = \begin{pmatrix} \mathbf{a}^i \\ \gamma^i \end{pmatrix}$$
(6.53)

which suffers neither the low-frequency breakdown nor the dense mesh breakdown, but has the spurious resonance problems at high frequencies.

Another choice is to choose the second and fourth equations,

$$-\begin{pmatrix} \mathcal{S}_{k_1}^t & -\mathcal{P}_{k_1}^2 \\ \nabla \cdot \mathcal{S}_{k_1} & k_1^2 \mathcal{S}_{k_1} \end{pmatrix} \begin{pmatrix} \mathbf{a}_1 \\ \gamma_1 \end{pmatrix} = \begin{pmatrix} \mathbf{b}^i \\ \sigma^i \end{pmatrix}$$
(6.54)

This formulation also suffers from the resonance problem. $k_1^2 S_{k_1}$ will vanish as the frequency approaches zero, and the system leads to a saddle point problem that needs special care [131]. At high frequency, a frequency scaling has to be made to fix the ka dependence of the same operator.

A linear combination of the above two sets of VPIEs (6.53) and (6.54) should be helpful in avoiding resonances. Besides those two formulations, other options of choosing two different equations from the four in (6.52) are possible, and they might have different spectral properties and different immunities against spurious resonances.

6.8 Numerical Results

In this section, numerical examples are given to demonstrate the stability properties of the presented integral equations. For simplicity, the scalar potential Φ is assumed to be zero, and only the vector potential integral equation is left to be solved. Thus the DPIE solution only involves the VPIE. This is done for two reasons; (a) the operators involved in the SPIE are well studied in the context of acoustics [101,111] and (b) since the operators involved in the VPIE are are more complex, this approach highlights their behavior. In the general case, the SPIE and VPIE must be solved simultaneously to recover both the electric and magnetic fields.

In the first test, the linear system for a spherical object is studied for the condition numbers and eigenvalue distributions. The transmission problem has the following setup: $\epsilon_2 = 2\epsilon_1 = 2\epsilon_0$, and $\mu_2 = \mu_1 = \mu_0$. Modes up to 30th degree are used and the system size is about 1800 × 1800. The condition numbers of the new formulation for a 1m sphere are very low across the low-frequency band, and remain near 1.25 for frequencies from 1 Hz to 10^7 Hz. The stable condition numbers are due to the second kind nature of the integral equation.

Figs. 6.1 and 6.2 show the eigenvalues of the system at 1.0 Hz and 10⁷ Hz, respectively. All of the eigenvalues are clustered around 0.5 in the complex plane, both figures illustrating the nice spectral properties. As a result, an iterative solver will be very efficient for systems such as this one.

The following test is to study the behavior of conditioning at high frequencies where the spatial resolution must grow proportional to the frequency. In the implementation, the highest degree of the basis functions is set to [2ka] + 1. The condition number of the VPIE versus frequency is demonstrated in Fig. 6.3. For comparison, the condition number for the case of the Müller formulation is given in Fig. 6.4. For reference, the dashed curves in both figures indicate the trend that a linearly varying condition number would follow. It's observed that both formulations lead to an oscillatory increase in condition

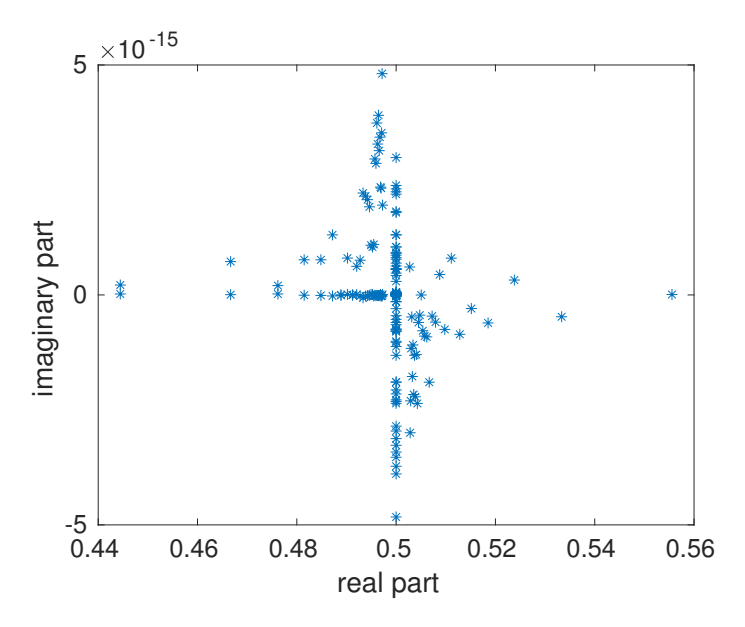


Figure 6.1: Real and imaginary parts of eigenvalues at 1 Hz

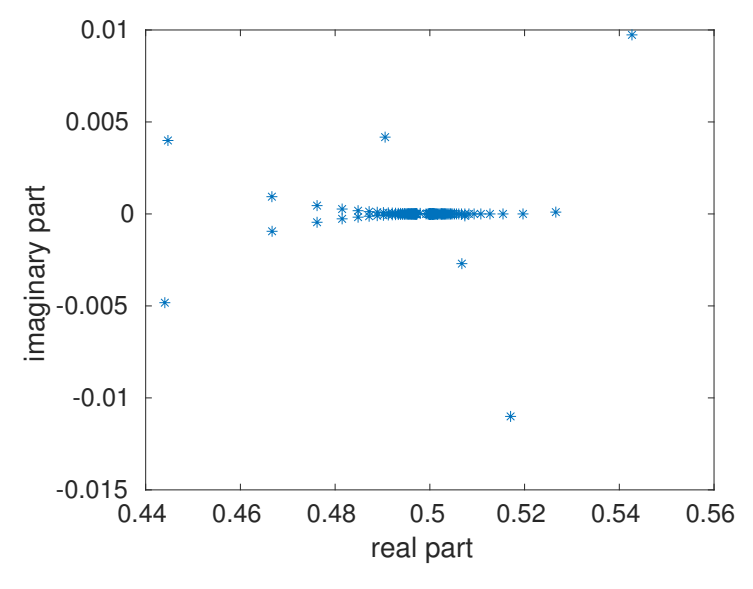


Figure 6.2: Real and imaginary parts of eigenvalues at $1\times10^7~\mathrm{Hz}$

number with frequency. Though the high frequency behavior may not be as ideal as at low frequency, a growing condition number proportional to the electrical size does not necessarily lead to the same situation for the iteration count. As in other extant approaches, the convergence of iterative solvers in the high frequency regime can be accelerated using effective preconditioning techniques [137–139]. This could be a future topic worth more study and discussions.

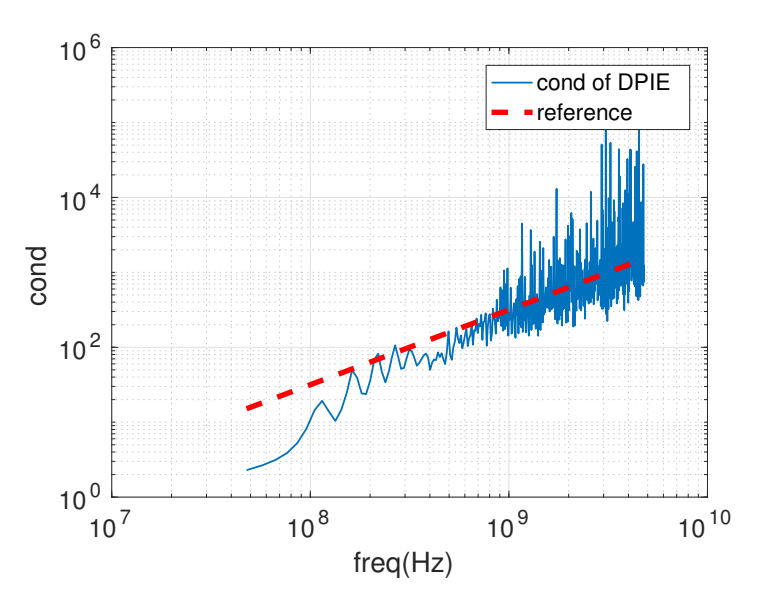


Figure 6.3: Condition number of VPIE formulation versus frequency

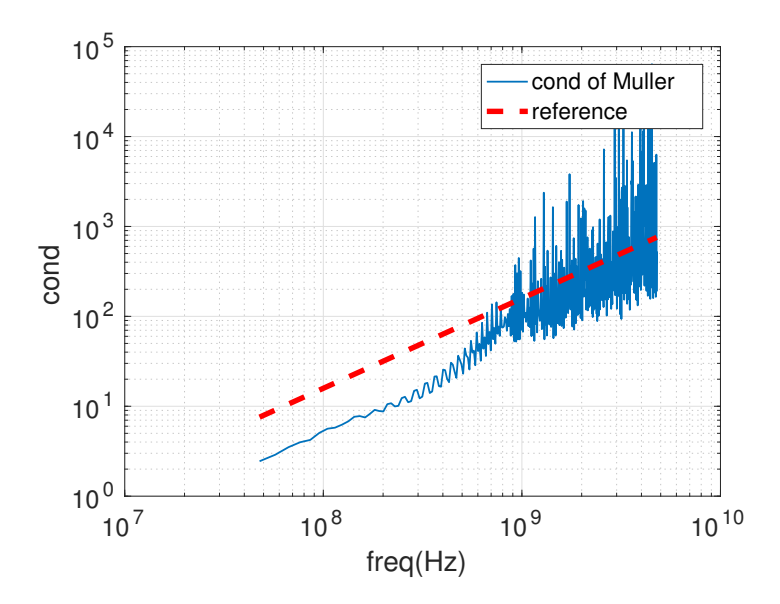


Figure 6.4: Condition number of Müller formulation versus frequency

In order to show the validity of the formulation, comparison is made between the solution of the VPIE and that using the Mie series approach. Figs. 6.5 and Fig. 6.6, respectively, give the real part of the coefficients of mode Ψ^1_{30} and Φ^1_{30} in the tangential components of the electric field (twisted magnetic current density). The error between the Mie series and the DPIE solution is close to machine precision, thanks to the fact that the basis functions used are eigenfunctions of the vector Laplace-Beltrami operator. From each of the plots, one

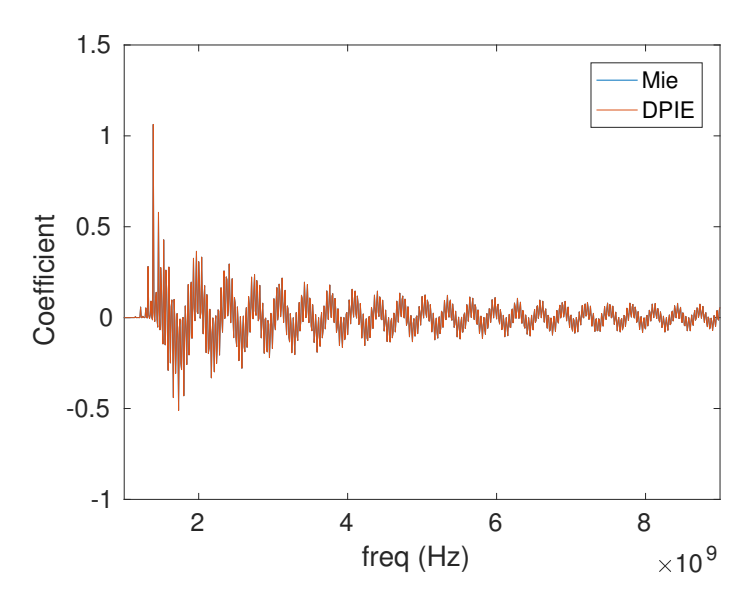


Figure 6.5: Real part of the coefficients for Ψ^1_{30} mode in the tangential component of the electric field

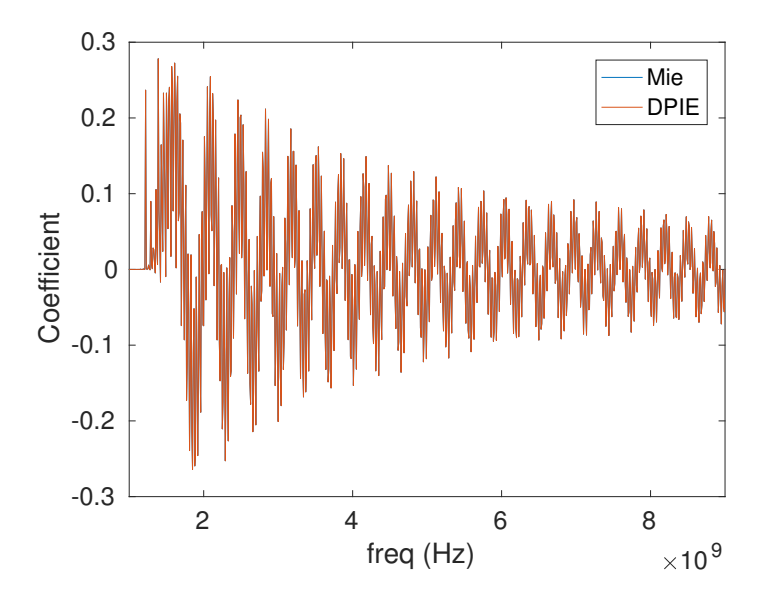


Figure 6.6: Real part of the coefficients for Φ^1_{30} mode in the tangential component of the electric field

observes that the frequency response of the transmission problem is very oscillatory. As the frequency decreases, tending to the static limit, the response can still be recovered accurately by the new formulation.

6.9 Conclusion and Future Work

Decoupled potential integral equations for electromagnetic scattering from homogeneous dielectric objects have been proposed. The resulting formulations are well-conditioned second kind integral equations without low frequency or dense mesh breakdown problems. When reducing the formulation to solve PEC problems, several options are available. Observables and integral equations must be carefully chosen from (6.52) to obtain formulations avoiding resonance, low-frequency breakdown or saddle point phenomena.

When setting the scalar potential Φ to zero, the vector potential boundary value problem becomes an exact (scaled) electric field-based description of the original Maxwell's transmission problem. Interestingly, this special case of our formulation is also a direct approach and is dual to that presented by Vico et al. [132] almost at the same time as this manuscript was submitted. Their work starts from an indirect approach with rigorous mathematical proof linking the solution to the resulting integral equation with that of the original transmission problem. With slight changes, the two formulations can be considered as adjoint to one another. Therefore, [132] provides mathematical insights on interpreting the uniqueness of the new vector potential integral equation. From the physical point of view, it's worthing asking the question as to whether a constraint on the potential exists that guarantees the uniqueness of the solutions to the potential-based integral equation. In this chapter, two scalar potential jumps (V_1 and V_2) in the decoupled boundary conditions (6.25) and (6.26) are set to zero.

In terms of using the new set of unknowns (two tangential vectors and two scalars), the VPIE in the new formulation is also similar to the current-charge integral equation. The difference lies in that, in our formulation, (1) no continuity constraint is needed and (2) one charge term and one scalar potential term (rather than two charge terms) are used in addition to the two tangential terms. In addition, the SPIE involves another two scalar unknowns (one is the potential and other one is its normal derivative), again very similar to the acoustics case.

It should be pointed out that both the number of integral operators to be discretized and the number of unknowns involved in the DPIE equations exceed that of conventional integral equations. However, the stability properties of the new integral equations and the availability of fast methods (e.g. fast multipole, adaptive integral, and algebraic-based compression methods) make the investigation of these new formulations attractive. Discretization issues, numerical implementations, and performance, especially at high frequencies, will be studied and presented in an upcoming communication.

APPENDICES

APPENDIX A

SPHERICAL EXPANSIONS

A.1 Vector Spherical Harmonics (VSH) and Wave Functions (VSWF)

The two vector spherical wave functions used in conventional expansion of dyadic Green's function are defined as follows.

$$\mathbf{M}_{nm}^{(i)}(k,\bar{r}) = -z_n^{(i)}(kr)\mathbf{\Phi}_{nm}(\theta,\phi) \tag{A.1}$$

$$\mathbf{N}_{nm}^{(i)}(k,\bar{r}) = \frac{\left[krz_n^{(i)}(kr)\right]'}{kr} \mathbf{\Psi}_{nm}(\theta,\phi) + \frac{\sqrt{n(n+1)}}{kr} z_n^{(i)}(kr) \mathbf{Y}_n^m(\theta,\phi)$$
(A.2)

where $\mathbf{Y}_n^m(\theta,\phi) = Y_n^m(\theta,\phi)\hat{r}$.

In order to derive the spherical harmonics expansion of the tangential trace of the dyadic Green's function, the mapping relations between VSH and VSWF should be used.

$$\hat{r} \times \mathbf{M}_{nm}^{(i)}(k,\bar{r}) = z_n^{(i)}(kr)\mathbf{\Psi}_{nm}(\theta,\phi) \tag{A.3}$$

$$\hat{r} \times \hat{r} \times \mathbf{M}_{nm}^{(i)}(k, \bar{r}) = z_n^{(i)}(kr)\mathbf{\Phi}_{nm}(\theta, \phi)$$
(A.4)

$$\hat{r} \times \mathbf{N}_{nm}^{(i)}(k,\bar{r}) = \frac{[krz_n^{(i)}(kr)]'}{kr} \mathbf{\Phi}_{nm}(\theta,\phi)$$
(A.5)

$$\hat{r} \times \hat{r} \times \mathbf{N}_{nm}^{(i)}(k,\bar{r}) = -\frac{[krz_n^{(i)}(kr)]'}{kr} \mathbf{\Psi}_{nm}(\theta,\phi)$$
(A.6)

A.2 Spherical expansion of the time domain magnetic dyadic Green's function

Frequency-domain dyadic Green's function of magnetic field is the solution to the wave equation.

$$\nabla \times \nabla \times \tilde{\mathbf{G}}_{m0} - k^2 \tilde{\mathbf{G}}_{m0} = \nabla \times [\tilde{I}\delta(\bar{r} - \bar{r}')], \tag{A.7}$$

The dyadic Green's function can be written in terms of the scalar Green's function in free space.

$$\tilde{\mathbf{G}}_{m0}(\bar{r}, \bar{r}', \omega) = \nabla \times [\tilde{I}G_o(\bar{r}, \bar{r}')] = \nabla G_0(\bar{r}, \bar{r}') \times \tilde{I}$$
(A.8)

As in electric field case, the dyadic Green's function can be expanded using a series of vector spherical wave functions.

$$\tilde{\mathbf{G}}_{m0}(\bar{r}, \bar{r}', \omega) = jk^{2} \sum_{n,m} \left[\mathbf{M}_{nm}^{(4)}(k, \bar{r}) \mathbf{N}_{nm}^{(1)*}(k, \bar{r}') + \mathbf{N}_{nm}^{(4)}(k, \bar{r}) \mathbf{M}_{nm}^{(1)*}(k, \bar{r}') \right]$$
(A.9)

By taking the tangential trace of this dyadic Green's function, one can get a modified Green's function expanded purely by vector spherical harmonics, separating the explicit radial dependence from non-radial dependence.

$$\tilde{\mathbf{G}}_{m0}^{tt}(\bar{r}, \bar{r}', \omega) = \hat{r} \times \tilde{\mathbf{G}}_{m0}(\bar{r}, \bar{r}', \omega) \times \hat{r}' \times \hat{r}'$$

$$= jk^{2} \sum_{n,m} \left[\frac{\left[kr z_{n}^{(4)}(kr) \right]'}{kr} z_{n}^{(1)*}(kr') \mathbf{\Phi}_{nm}(\hat{r}) \mathbf{\Phi}_{nm}(\hat{r}') \right]$$

$$- z_{n}^{(4)}(kr) \frac{\left[kr' z_{n}^{(1)*}(kr') \right]'}{kr'} \mathbf{\Psi}_{nm}(\hat{r}) \mathbf{\Psi}_{nm}(\hat{r}') \right]$$
(A.10)

The reason that $\hat{r} \times$ instead of $\hat{r} \times \hat{r} \times$ is chosen in the left side is due to the fact that there is already one tangential operator $\hat{r} \times$ in the \mathcal{K} operator. Similar as in electric field case, the modified dyadic Green's function has the following properties.

$$\tilde{\mathbf{G}}_{m0}^{tt}(\bar{r}, \bar{r}', \omega) \cdot \mathbf{X} = -\tilde{\mathbf{G}}_{m0}(\bar{r}, \bar{r}', \omega) \cdot \mathbf{X}$$
(A.11a)

$$\mathbf{X} \cdot \hat{r} \times \tilde{\mathbf{G}}_{m0}^{tt}(\bar{r}, \bar{r}', \omega) = -\mathbf{X} \cdot \hat{r} \times \tilde{\mathbf{G}}_{m0}(\bar{r}, \bar{r}', \omega) \tag{A.11b}$$

In order to get the time-domain expansion, inverse Fourier transform of the above equation gives the following formula.

$$\tilde{\mathbf{G}}_{m0}^{tt}(\bar{r}, \bar{r}', t) =
\sum_{n,m} \left[\mathcal{F}^{-1} \left\{ jk \frac{\partial}{r \partial r} \left[rz_n^{(4)}(kr) \right] z_n^{(1)}(kr') \right\} \boldsymbol{\Phi}_{nm}(\hat{r}) \boldsymbol{\Phi}_{nm}(\hat{r}') \right.
\left. - \mathcal{F}^{-1} \left\{ jk \frac{\partial}{r' \partial r'} \left[r'z_n^{(1)}(kr') \right] z_n^{(4)}(kr) \right\} \boldsymbol{\Psi}_{nm}(\hat{r}) \boldsymbol{\Psi}_{nm}(\hat{r}') \right]$$
(A.12)

Due to the linearity of (inverse) Fourier transform, one can get the following results.

$$\mathcal{F}^{-1}\left\{jk\frac{\partial}{r'\partial r'}\left[r'z_n^{(1)}(kr')\right]z_n^{(4)}(kr)\right\} = -\frac{\partial_{r'}}{r'}\left[r'K_n^{(0)}(r,r',t)\right]$$
(A.13)

$$\mathcal{F}^{-1}\{jk\frac{\partial}{r\partial r}\left[rz_n^{(4)}(kr)\right]z_n^{(1)}(kr')\} = -\frac{\partial_r}{r}\left[rK_n^{(0)}(r,r',t)\right]$$
(A.14)

By using above two kernels in (A.12), one can get the spherical expansion for the timedomain dyadic Green's function as in (2.26).

APPENDIX B

BOUNDARY INTEGRAL OPERATORS

The following are integral operators commonly used in integral equations for Helmholtz and Maxwell's equations. Limiting cases for some of them are also given to help the analysis of properties of the presented integral equation based formulation.

$$S[\sigma] = \int G(\mathbf{r}, \mathbf{r}') \sigma(\mathbf{r}') dS'$$
(B.1)

$$\mathcal{D}[\sigma] = \int \frac{\partial G(\mathbf{r}, \mathbf{r}')}{\partial n'} \sigma(\mathbf{r}') dS' \stackrel{\mathbf{r} \to \mathbf{r}^{\pm}}{==} \pm \frac{1}{2} \sigma + \tilde{\mathcal{D}}[\sigma]$$
(B.2)

$$\mathcal{D}'[\sigma] = \int \frac{\partial G(\mathbf{r}, \mathbf{r}')}{\partial n} \sigma(\mathbf{r}') dS' \stackrel{\mathbf{r} \to \mathbf{r}^{\pm}}{=} \mp \frac{1}{2} \sigma + \tilde{\mathcal{D}}'[\sigma]$$
(B.3)

$$\mathcal{N}[\sigma] = \frac{\partial}{\partial n} \mathcal{D}[\sigma] = \frac{\partial}{\partial n} \int \frac{\partial G(\mathbf{r}, \mathbf{r})}{\partial n'} \sigma(\mathbf{r}') dS'$$
(B.4)

$$\mathcal{K}[\mathbf{a}] = \mathbf{n} \times \nabla \times \int G(\mathbf{r}, \mathbf{r}') \mathbf{a}(\mathbf{r}') dS' \stackrel{\mathbf{r} \to \mathbf{r}^{\pm}}{=} \pm \frac{1}{2} \mathbf{a} + \tilde{\mathcal{K}}[\mathbf{a}]$$
(B.5)

$$\mathcal{K}'[\mathbf{a}] = \mathbf{n} \times \mathbf{n} \times \nabla \times \int G(\mathbf{r}, \mathbf{r}') \mathbf{n} \times \mathbf{a}(\mathbf{r}') dS' \stackrel{\mathbf{r} \to \mathbf{r}^{\pm}}{=} \mp \frac{1}{2} \mathbf{a} + \tilde{\mathcal{K}}'[\mathbf{a}]$$
(B.6)

$$\mathcal{T}[\mathbf{a}] = \mathbf{n} \times \nabla \times \nabla \times \int G(\mathbf{r}, \mathbf{r}') \mathbf{n} \times \mathbf{a}(\mathbf{r}') dS'$$
(B.7)

In the above, $\mathbf{r} \to \mathbf{r}^{\pm}$ means that the position vector is approaching the surface from the exterior (+) or interior (-) domain. \mathcal{T} and \mathcal{N} are hypersingular and unbounded integral operators, both of which are self-adjoint operators. \mathcal{S} , $\tilde{\mathcal{K}}$, $\tilde{\mathcal{K}}'$, $\tilde{\mathcal{D}}$ and $\tilde{\mathcal{D}}'$ are compact (also bounded) operators, with the adjoint operators of $\tilde{\mathcal{K}}$ and $\tilde{\mathcal{D}}$ being $\tilde{\mathcal{K}}'$ and $\tilde{\mathcal{D}}'$ respectively [101]. It is straightforward that \mathcal{D} , \mathcal{D}' , \mathcal{K} and \mathcal{K}' can be used to construct integral equations of the second type.

Also we have the following convention for denoting different traces of one operator: $S^n = \mathbf{n} \times S$, $S^t = \mathbf{n} \times \mathbf{n} \times S$ and $S^r = \mathbf{n} \cdot S$.

BIBLIOGRAPHY

BIBLIOGRAPHY

- [1] J. Li and B. Shanker, "Time-dependent lorentz-mie-debye formulation for electromagnetic scattering from dielectric spheres," *Progress In Electromagnetics Research*, vol. 154, pp. 195–208, 2015.
- [2] —, "Time-dependent debye-mie series solutions for electromagnetic scattering," *IEEE Transactions on Antennas and Propagation*, vol. 63, no. 8, pp. 3644–3653, Aug 2015.
- [3] J. Li, D. Dault, and B. Shanker, "A quasianalytical time domain solution for scattering from a homogeneous sphere," *The Journal of the Acoustical Society of America*, vol. 135, no. 4, pp. 1676–1685, 2014.
- [4] J. Li and B. Shanker, "Isogeometric analysis of em scattering on multiply-connected subdivision surfaces," in 2017 IEEE International Symposium on Antennas and Propagation USNC/URSI National Radio Science Meeting, July 2017, pp. 1557–1558.
- [5] J. Li, D. Dault, B. Liu, Y. Tong, and B. Shanker, "Subdivision based Isogeometric Analysis Technique for Electric Field Integral Equations for Simply Connected Structures," *Journal of Computational Physics*, vol. 319, pp. 145–162, 2016.
- [6] J. A. Stratton, *Electromagnetic theory*. John Wiley and Sons, 1941.
- [7] A. Ishimaru, Electromagnetic Wave Propagation, Radiation, and Scattering. Prentice Hall, Dec 1990.
- [8] M. Kerker, The scattering of light and other electromagnetic radiation. Academic Press, 1 1969.
- [9] W. Hergert and T. Wriedt, Eds., The Mie Theory: Basics and Applications (Springer Series in Optical Sciences), 2012th ed. Springer, 7 2012.
- [10] M. I. Mishchenko, L. D. Travis, and A. A. Lacis, Scattering, Absorption, and Emission of Light by Small Particles, 1st ed. Cambridge University Press, 6 2002.
- [11] O. Gulder, G. Smallwood, R. Wong, D. Snelling, R. Smith, B. Deschamps, and J.-C. Sautet, "Flame front surface characteristics in turbulent premixed propane/air combustion," *Combustion and Flame*, vol. 120, no. 4, pp. 407 416, 2000.
- [12] J. Hansen, Spherical Near-Field Antenna Measurement. London: Peter Peregrinus, 1988.
- [13] J. A. Schuller and M. L. Brongersma, "General properties of dielectric optical antennas," *Opt. Express*, vol. 17, no. 26, pp. 24084–24095, Dec 2009.
- [14] D. Deirmendjian, "Scattering and polarization properties of water clouds and hazes in the visible and infrared," *Appl. Opt.*, vol. 3, no. 2, pp. 187–196, Feb 1964.

- [15] M. V. Rybin, A. B. Khanikaev, M. Inoue, K. B. Samusev, M. J. Steel, G. Yushin, and M. F. Limonov, "Fano resonance between mie and bragg scattering in photonic crystals," *Phys. Rev. Lett.*, vol. 103, p. 023901, Jul 2009.
- [16] P. Bassan, A. Kohler, H. Martens, J. Lee, H. J. Byrne, P. Dumas, E. Gazi, M. Brown, N. Clarke, and P. Gardner, "Resonant mie scattering (rmies) correction of infrared spectra from highly scattering biological samples," *Analyst*, vol. 135, pp. 268–277, 2010.
- [17] O. M. Buyukdura and S. S. Koc, "Two alternative expressions for the spherical wave expansion of the time domain scalar free-space Green's function and an application: Scattering by a soft sphere," *Journal of the Acoustical Society of America*, vol. 101, no. 1, pp. 87–91, 1997.
- [18] B. Liu, A. Yamilov, Y. Ling, J. Y. Xu, and H. Cao, "Dynamic nonlinear effect on lasing in a random medium," *Phys. Rev. Lett.*, vol. 91, p. 063903, Aug 2003.
- [19] P. K. Jain, K. S. Lee, I. H. El-Sayed, and M. A. El-Sayed, "Calculated absorption and scattering properties of gold nanoparticles of different size, shape, and composition: Applications in biological imaging and biomedicine," *The Journal of Physical Chemistry B*, vol. 110, no. 14, pp. 7238–7248, 2006, pMID: 16599493.
- [20] K. Leung, K. Luk, K. Lai, and D. Lin, "Theory and experiment of a coaxial probe fed hemispherical dielectric resonator antenna," *Antennas and Propagation, IEEE Transactions on*, vol. 41, no. 10, pp. 1390–1398, Oct 1993.
- [21] A. Shlivinski, E. Heyman, and A. J. Devaney, "Time domain radiation by scalar sources: Plane wave to multipole transform," *Journal of Mathematical Physics*, vol. 42, no. 12, p. 5915, Dec. 2001.
- [22] E. Heyman, "Time-dependent plane-wave spectrum representations for radiation from volume source distributions," *Journal of Mathematical Physics*, vol. 37, no. 2, p. 658, 1996.
- [23] K. D. Granzow, "Multipole Theory in the Time Domain," *Journal of Mathematical Physics*, vol. 7, no. 4, p. 634, Dec. 1966.
- [24] W. C. Davidon, "Time-dependent multipole analysis," *Journal of Physics A: Mathematical, Nuclear and General*, vol. 6, no. 11, pp. 1635–1646, Nov. 1973.
- [25] E. A. Marengo and A. J. Devaney, "Time-dependent plane wave and multipole expansions of the electromagnetic field," *Journal of Mathematical Physics*, vol. 39, no. 7, p. 3643, 1998.
- [26] A. J. Devaney, "Multipole expansions and plane wave representations of the electromagnetic field," *Journal of Mathematical Physics*, vol. 15, no. 2, p. 234, Nov. 1974.
- [27] E. Heyman and A. J. Devaney, "Time-dependent multipoles and their application for radiation from volume source distributions," *Journal of Mathematical Physics*, vol. 37, no. 2, pp. 682–692, 1996.

- [28] A. Shlivinski and E. Heyman, "Time-domain near-field analysis of short-pulse antennas .I. Spherical wave (multipole) expansion," *IEEE Transactions on Antennas and Propagation*, vol. 47, no. 2, pp. 271–279, 1999.
- [29] C.-C. Oetting and L. Klinkenbusch, "Near-to-far-field transformation by a time-domain spherical-multipole analysis," *IEEE Transactions on Antennas and Propagation*, vol. 53, no. 6, pp. 2054–2063, Jun. 2005.
- [30] E. Whittaker, "On the partial differential equations of mathematical physics," *Mathematische Annalen*, vol. 57, no. 3, pp. 333–355, 1903.
- [31] A. A. Ergin, B. Shanker, and E. Michielssen, "Fast analysis of transient acoustic wave scattering from rigid bodies using the multilevel plane wave time domain algorithm," *The Journal of the Acoustical Society of America*, vol. 107, no. 3, pp. 1168–1178, 2000.
- [32] B. Shanker, A. Ergin, and E. Michielssen, "Fast analysis of transient electromagnetic scattering phenomena using the multilevel plane wave time domain algorithm," *IEEE Transactions on Antennas and Propagation*, vol. 51, no. 3, pp. 628–641, Mar. 2003.
- [33] L. Greengard, T. Hagstrom, and S. Jiang, "The solution of the scalar wave equation in the exterior of a sphere," *Journal of Computational Physics*, vol. 274, pp. 191–207, Oct. 2014.
- [34] S. Azizoglu, S. Koc, and O. Buyukdura, "Spherical Wave Expansion of the Time-Domain Free-Space Dyadic Green's Function," *IEEE Transactions on Antennas and Propagation*, vol. 52, no. 3, pp. 677–683, Mar. 2004.
- [35] C.-T. Tai, *Dyadic green functions in electromagnetic theory*, 2nd ed. Piscataway: IEEE Press, 1994.
- [36] E. L. Hill, "The Theory of Vector Spherical Harmonics," *American Journal of Physics*, vol. 22, no. 4, p. 211, Apr. 1954.
- [37] B. Carrascal, G. A. Estevez, P. Lee, and V. Lorenzo, "Vector spherical harmonics and their application to classical electrodynamics," *European Journal of Physics*, vol. 12, no. 4, pp. 184–191, Jul. 1991.
- [38] A. J. Pray, Y. Beghein, N. V. Nair, K. Cools, H. Bağcı, and B. Shanker, "A higher order space-time galerkin scheme for time domain integral equations," *IEEE Transactions on Antennas and Propagation*, vol. 62, no. 12, pp. 6183–6191, 2014.
- [39] H. Brunner, P. J. Davies, and D. B. Duncan, "Global convergence and local super-convergence of first-kind volterra integral equation approximations," *IMA Journal of Numerical Analysis*, 2011.
- [40] A. Pray, N. Nair, and B. Shanker, "Stability Properties of the Time Domain Electric Field Integral Equation Using a Separable Approximation for the Convolution With the Retarded Potential," *IEEE Transactions on Antennas and Propagation*, vol. 60, no. 8, pp. 3772–3781, Aug. 2012.

- [41] D. Weile, G. Pisharody, N.-W. Chen, B. Shanker, and E. Michielssen, "A Novel Scheme for the Solution of the Time-Domain Integral Equations of Electromagnetics," *IEEE Transactions on Antennas and Propagation*, vol. 52, no. 1, pp. 283–295, Jan. 2004.
- [42] S. P. Walker, M. J. Bluck, and I. Chatzis, "The stability of integral equation time-domain scattering computations for three-dimensional scattering; similarities and differences between electrodynamic and elastodynamic computations," *International Journal of Numerical Modelling: Electronic Networks, Devices and Fields*, vol. 15, no. 5-6, pp. 459–474, 2002.
- [43] L. Valle, F. Rivas, and M. F. Catedra, "Combining the moment method with geometrical modelling by nurbs surfaces and bezier patches," *IEEE Transactions on Antennas and Propagation*, vol. 42, no. 3, pp. 373–381, Mar 1994.
- [44] T. J. R. Hughes, J. A. Cottrell, and Y. Bazilevs, "Isogeometric analysis: CAD, finite elements, NURBS, exact geometry and mesh refinement," *Comput. Methods Appl. Mech. Eng.*, vol. 194, no. 39-41, pp. 4135–4195, 2005.
- [45] D. L. Dault, N. V. Nair, J. Li, and B. Shanker, "The generalized method of moments for electromagnetic boundary integral equations," *IEEE Transactions on Antennas and Propagation*, vol. 62, no. 6, pp. 3174–3188, June 2014.
- [46] M. Feischl, G. Gantner, and D. Praetorius, "Reliable and efficient a posteriori error estimation for adaptive {IGA} boundary element methods for weakly-singular integral equations," Computer Methods in Applied Mechanics and Engineering, vol. 290, pp. 362 386, 2015.
- [47] A. F. Peterson and A. F., "Cell Curvature and Far-Field Superconvergence in Numerical Solutions of Electromagnetic Integral Equations," *International Journal of Antennas and Propagation*, vol. 2016, pp. 1–7, 2016.
- [48] C. Loop, "Smooth Subdivision Surfaces Based on Triangles," M.S. thesis, University of Utah, 1987.
- [49] J. Stam, "Evaluation of loop subdivision surfaces," in *Computer Graphics Proceedings ACM SIGGRAPH*, 1998.
- [50] F. Cirak, M. Ortiz, and P. Schröder, "Subdivision surfaces: a new paradigm for thin-shell finite-element analysis," *International Journal for Numerical Methods in Engineering*, vol. 47, no. 12, pp. 2039–2072, Apr. 2000.
- [51] G. C. Hsiao and R. E. Kleinman, "Mathematical foundations for error estimation in numerical solutions of integral equations in electromagnetics," *IEEE Transactions on Antennas and Propagation*, vol. 45, no. 3, pp. 316–328, Mar 1997.
- [52] S. Rao, D. Wilton, and A. Glisson, "Electromagnetic scattering by surfaces of arbitrary shape," *IEEE Trans. Antennas Propag.*, vol. 30, no. 3, pp. 409–418, May 1982.

- [53] W. Cai, T. Yu, H. Wang, and Y. Yu, "High-order mixed RWG basis functions for electromagnetic applications," *IEEE Transactions on Microwave Theory and Techniques*, vol. 49, no. 7, pp. 1295–1303, Jul. 2001.
- [54] A. D. Hellicar, J. S. Kot, G. James, and G. K. Cambrell, "A Comparison of Higher Order Nodal- and Edge-Basis Functions in the MFIE on Rational BÉzier Geometries," *IEEE Transactions on Antennas and Propagation*, vol. 56, no. 6, pp. 1812–1818, Jun. 2008.
- [55] R. Rieben, G. Rodrigue, and D. White, "A high order mixed vector finite element method for solving the time dependent Maxwell equations on unstructured grids," *Journal of Computational Physics*, vol. 204, no. 2, pp. 490–519, Apr. 2005.
- [56] E. Jorgensen, J. L. Volakis, P. Meincke, and O. Breinbjerg, "Higher order hierarchical legendre basis functions for electromagnetic modeling," *IEEE Transactions on Antennas and Propagation*, vol. 52, no. 11, pp. 2985–2995, Nov 2004.
- [57] R. D. Graglia, D. R. Wilton, and A. F. Peterson, "Higher order interpolatory vector bases for computational electromagnetics," *IEEE Transactions on Antennas and Propagation*, vol. 45, no. 3, pp. 329–342, Mar 1997.
- [58] R. Sevilla, S. Fernández-Méndez, and A. Huerta, "3D NURBS-enhanced finite element method (NEFEM)," *International Journal for Numerical Methods in Engineering*, vol. 88, no. 2, pp. 103–125, Oct. 2011.
- [59] J. Nedelec, "Mixed finite elements in \mathbb{R}^3 ," Numerische Mathematik, vol. 35, no. 3, pp. 315–341, 1980.
- [60] J. Cottrell, A. Reali, Y. Bazilevs, and T. Hughes, "Isogeometric analysis of structural vibrations," *Computer Methods in Applied Mechanics and Engineering*, vol. 195, no. 41-43, pp. 5257–5296, Aug. 2006.
- [61] Y. Bazilevs, M.-C. Hsu, and M. A. Scott, "Isogeometric fluid-structure interaction analysis with emphasis on non-matching discretizations, and with application to wind turbines," *Computer Methods in Applied Mechanics and Engineering*, vol. 249–252, no. 0, pp. 28–41, 2012.
- [62] L. De Lorenzis, J. Evans, T. Hughes, and A. Reali, "Isogeometric collocation: Neumann boundary conditions and contact," *Computer Methods in Applied Mechanics and Engineering*, vol. 284, pp. 21–54, Feb. 2015.
- [63] K. Nordanger, R. Holdahl, A. M. Kvarving, A. Rasheed, and T. Kvamsdal, "Implementation and comparison of three isogeometric Navier–Stokes solvers applied to simulation of flow past a fixed 2D NACA0012 airfoil at high Reynolds number," Computer Methods in Applied Mechanics and Engineering, vol. 284, pp. 664–688, Feb. 2015.
- [64] P. Kang and S.-K. Youn, "Isogeometric analysis of topologically complex shell structures," *Finite Elements in Analysis and Design*, vol. 99, pp. 68–81, Jul. 2015.

- [65] R. Bouclier, T. Elguedj, and A. Combescure, "An isogeometric locking-free NURBS-based solid-shell element for geometrically nonlinear analysis," *International Journal for Numerical Methods in Engineering*, vol. 101, no. 10, pp. 774–808, Mar. 2015.
- [66] R. Simpson, M. Scott, M. Taus, D. Thomas, and H. Lian, "Acoustic isogeometric boundary element analysis," *Computer Methods in Applied Mechanics and Engineering*, vol. 269, pp. 265–290, Feb. 2014.
- [67] A. Buffa, G. Sangalli, and R. Vázquez, "Isogeometric analysis in electromagnetics: B-splines approximation," *Computer Methods in Applied Mechanics and Engineering*, vol. 199, no. 17-20, pp. 1143–1152, Mar. 2010.
- [68] K. Kostas, A. Ginnis, C. Politis, and P. Kaklis, "Ship-hull shape optimization with a T-spline based BEM-isogeometric solver," *Computer Methods in Applied Mechanics and Engineering*, Oct. 2014.
- [69] G. Kuru, C. V. Verhoosel, K. G. van der Zee, and E. H. van Brummelen, "Goal-adaptive Isogeometric Analysis with hierarchical splines," *Computer Methods in Applied Mechanics and Engineering*, vol. 270, no. 0, pp. 270–292, 2014.
- [70] J. Kiendl, R. Schmidt, R. Wüchner, and K.-U. Bletzinger, "Isogeometric shape optimization of shells using semi-analytical sensitivity analysis and sensitivity weighting," Computer Methods in Applied Mechanics and Engineering, vol. 274, no. 0, pp. 148–167, 2014.
- [71] T. DeRose, M. Kass, and T. Truong, "Subdivision surfaces in character animation," in *Proceedings of the 25th Annual Conference on Computer Graphics and Interactive Techniques*, ser. SIGGRAPH '98. New York, NY, USA: ACM, 1998, pp. 85–94.
- [72] Y. Bazilevs, V. M. Calo, J. A. Cottrell, J. A. Evans, T. J. R. Hughes, S. Lipton, M. A. Scott, and T. W. Sederberg, "Isogeometric analysis using T-splines," *Comput. Methods Appl. Mech. Eng.*, vol. 199, no. 5-8, pp. 229–263, 2010.
- [73] M. R. Dörfel, B. Jüttler, and B. Simeon, "Adaptive isogeometric analysis by local hrefinement with T-splines," *Computer Methods in Applied Mechanics and Engineering*, vol. 199, no. 5-8, pp. 264–275, Jan. 2010.
- [74] P. J. Barendrecht, "IsoGeometric Analysis with Subdivision Surfaces," Ph.D. dissertation, Eindhoven University of Technology, 2013.
- [75] R. Simpson, S. Bordas, J. Trevelyan, and T. Rabczuk, "A two-dimensional Isogeometric Boundary Element Method for elastostatic analysis," *Computer Methods in Applied Mechanics and Engineering*, vol. 209-212, pp. 87–100, Feb. 2012.
- [76] M. Scott, R. Simpson, J. Evans, S. Lipton, S. Bordas, T. Hughes, and T. Sederberg, "Isogeometric boundary element analysis using unstructured T-splines," Computer Methods in Applied Mechanics and Engineering, vol. 254, pp. 197–221, Feb. 2013.

- [77] R. Vazquez, A. Buffa, and L. Di Rienzo, "NURBS-Based BEM Implementation of High-Order Surface Impedance Boundary Conditions," *IEEE Transactions on Magnetics*, vol. 48, no. 12, pp. 4757–4766, Dec. 2012.
- [78] J. Mautz and R. F. Harrington, "H-field, e-field and combined field solution for conducting bodies of revolution," *Arch. Elektron. Übertragung.tech.*, vol. 32, no. 4, pp. 157–164, 1978.
- [79] J. Mautz and R. Harrington, "A combined-source solution for radiation and scattering from a perfectly conducting body," *IEEE Transactions on Antennas and Propagation*, vol. 27, no. 4, pp. 445–454, Jul 1979.
- [80] A. D. Yaghjian, "Augmented electric- and magnetic-field integral equations," *Radio Science*, vol. 16, no. 6, pp. 987–1001, 1981.
- [81] M. Taskinen and P. Yla-Oijala, "Current and charge integral equation formulation," Antennas and Propagation, IEEE Transactions on, vol. 54, no. 1, pp. 58–67, Jan 2006.
- [82] Q. Pan, G. Xu, G. Xu, and Y. Zhang, "Isogeometric analysis based on extended loop's subdivision," *Journal of Computational Physics*, vol. 299, pp. 731 746, 2015.
- [83] A. Bendali, "Numerical analysis of the exterior boundary value problem for the time-harmonic maxwell equations by a boundary finite element method part 1: The continuous problem," *Mathematics of Computation*, vol. 43, no. 167, pp. 29–46, 1984.
- [84] —, "Numerical analysis of the exterior boundary value problem for the time- harmonic maxwell equations by a boundary finite element method part 2: The discrete problem," *Mathematics of Computation*, vol. 43, no. 167, pp. 47–68, 1984.
- [85] A. Bespalov and N. Heuer, "The hp-bem with quasi-uniform meshes for the electric field integral equation on polyhedral surfaces: A priori error analysis," *Applied Numerical Mathematics*, vol. 60, no. 7, pp. 705 718, 2010.
- [86] W.-L. Wu, A. W. Glisson, and D. Kajfez, "A study of two numerical solution procedures for the electric field integral equation at low frequency," *Applied Computational Electromagnetics Society Journal*, vol. 10, no. 3, pp. 69–80, 1995.
- [87] G. Vecchi, "Loop-star decomposition of basis functions in the discretization of the EFIE," *IEEE Transactions on Antennas and Propagation*, vol. 47, no. 2, pp. 339–346, 1999.
- [88] F. P. Andriulli, "Loop-Star and Loop-Tree Decompositions: Analysis and Efficient Algorithms," *IEEE Transactions on Antennas and Propagation*, vol. 60, no. 5, pp. 2347–2356, May 2012.
- [89] J.-F. Lee and R. Burkholder, "Loop star basis functions and a robust preconditioner for efie scattering problems," *Antennas and Propagation, IEEE Transactions on*, vol. 51, no. 8, pp. 1855–1863, Aug 2003.

- [90] Z.-G. Qian and W. C. Chew, "Enhanced A-EFIE With Perturbation Method," *IEEE Transactions on Antennas and Propagation*, vol. 58, no. 10, pp. 3256–3264, Oct. 2010.
- [91] C. L. Epstein and L. Greengard, "Debye Sources and the Numerical Solution of the Time Harmonic Maxwell Equations," *COMMUNICATIONS ON PURE AND AP-PLIED MATHEMATICS*, vol. 63, no. 4, pp. 413–463, APR 2010.
- [92] C. L. Epstein, Z. Gimbutas, L. Greengard, A. Klockner, and M. O'Neil, "A consistency condition for the vector potential in multiply-connected domains," *IEEE Transactions on Magnetics*, vol. 49, no. 3, pp. 1072–1076, March 2013.
- [93] X. Y. Z. Xiong, L. J. Jiang, W. E. I. Sha, and Y.-H. Lo, "A New Efie Method Based on Coulomb Gauge for the Low-Frequency Electromagnetic Analysis," *Prog. Electromagn. Res.*, vol. 140, no. April, pp. 613–631, 2013.
- [94] F. Vipiana, P. Pirinoli, and G. Vecchi, "Spectral properties of the effe-mom matrix for dense meshes with different types of bases," *Antennas and Propagation*, *IEEE Transactions on*, vol. 55, no. 11, pp. 3229–3238, Nov 2007.
- [95] F. Andriulli, "Well-posed boundary element formulations in electromagnetics," Ph.D. dissertation, University of Michigan, 2008, copyright Copyright ProQuest, UMI Dissertations Publishing 2008; Last updated 2014-01-08; First page n/a.
- [96] S. H. Christiansen and J.-C. Nédélec, "A Preconditioner for the Electric Field Integral Equation Based on Calderon Formulas," *SIAM Journal on Numerical Analysis*, vol. 40, no. 3, pp. 1100–1135, Jan. 2002.
- [97] F. P. Andriulli, K. Cools, H. Bagci, F. Olyslager, A. Buffa, S. Christiansen, and E. Michielssen, "A Multiplicative Calderon Preconditioner for the Electric Field Integral Equation," *IEEE Transactions on Antennas and Propagation*, vol. 56, no. 8, pp. 2398–2412, Aug. 2008.
- [98] S. Yan, J.-M. Jin, and Z. Nie, "EFIE Analysis of Low-Frequency Problems With Loop-Star Decomposition and Calderón Multiplicative Preconditioner," *IEEE Transactions on Antennas and Propagation*, vol. 58, no. 3, pp. 857–867, Mar. 2010.
- [99] A. Buffa and S. H. Christiansen, "A dual finite element complex on the barycentric refinement," *MATHEMATICS OF COMPUTATION*, vol. 76, no. 260, pp. 1743–1769, 2007.
- [100] R. Ling, W. Wang, and D. Yan, "Fitting sharp features with loop subdivision surfaces," *Computer Graphics Forum*, vol. 27, no. 5, pp. 1383–1391, 2008.
- [101] D. Colton and R. Kress, *Integral Equation Methods in Scattering Theory*. John Wiley & Sons, 1983.
- [102] J. Song, C.-C. Lu, and W. C. Chew, "Multilevel fast multipole algorithm for electromagnetic scattering by large complex objects," *IEEE Transactions on Antennas and Propagation*, vol. 45, no. 10, pp. 1488–1493, Oct 1997.

- [103] F. Vico, M. Ferrando, L. Greengard, and Z. Gimbutas, "The decoupled potential integral equation for time-harmonic electromagnetic scattering," *Communications on Pure and Applied Mathematics*, vol. 69, no. 4, pp. 771–812, 2016.
- [104] Z. G. Qian and W. C. Chew, "A quantitative study on the low frequency breakdown of efie," *Microwave and Optical Technology Letters*, vol. 50, no. 5, pp. 1159–1162, 2008.
- [105] J. S. Zhao and W. C. Chew, "Integral equation solution of Maxwell's equations from zero frequency to microwave frequencies," *IEEE Trans. Antennas Propag.*, vol. 48, no. 10, pp. 1635–1645, 2000.
- [106] N. V. Nair and B. Shanker, "Generalized method of moments: A novel discretization technique for integral equations," *IEEE Trans. Antennas Propag.*, vol. 59, no. 6 PART 2, pp. 2280–2293, 2011.
- [107] J. R. Mautz and R. F. Harrington, "H-field, e-field, and combined field solutions for bodies of revolution," DTIC Document, Tech. Rep., 1977.
- [108] M. Taskinen and P. Ylä-Oijala, "Current and charge integral equation formulation," *IEEE Trans. Antennas Propag.*, vol. 54, no. 1, pp. 58–67, 2006.
- [109] H. Bagci, F. P. Andriulli, K. Cools, F. Olyslager, and E. Michielssen, "A calderon multiplicative preconditioner for the combined field integral equation," *IEEE Transactions on Antennas and Propagation*, vol. 57, no. 10, pp. 3387–3392, Oct 2009.
- [110] F. P. Andriulli, K. Cools, I. Bogaert, and E. Michielssen, "On a well-conditioned electric field integral operator for multiply connected geometries," *IEEE Transactions on Antennas and Propagation*, vol. 61, no. 4, pp. 2077–2087, April 2013.
- [111] R. E. Kleinman and P. A. Martin, "On single integral equations for the transmission problem of acoustics," *SIAM Journal on Applied Mathematics*, vol. 48, no. 2, pp. 307–325, 1988.
- [112] C. L. Epstein, L. Greengard, and M. O'Neil, "Debye sources and the numerical solution of the time harmonic maxwell equations ii," *Communications on Pure and Applied Mathematics*, vol. 66, no. 5, pp. 753–789, 2013.
- [113] E. V. Chernokozhin and A. Boag, "Method of generalized debye sources for the analysis of electromagnetic scattering by perfectly conducting bodies with piecewise smooth boundaries," *IEEE Trans. Antennas Propag.*, vol. 61, no. 4, pp. 2108–2115, 2013.
- [114] F. Vico, M. Ferrando-Bataller, T. Jiménez, and A. Berenguer, "A high order locally corrected Nyström implementation of the Decoupled Potential Integral Equation," in 2015 9th European Conference on Antennas and Propagation (EuCAP), May 2015, pp. 1–4.
- [115] X. Fu, J. Li, L. J. Jiang, and B. Shanker, "Generalized debye sources-based effe solver on subdivision surfaces," *IEEE Transactions on Antennas and Propagation*, vol. 65, no. 10, pp. 5376–5386, Oct 2017.

- [116] Z. Peng, K. H. Lim, and J. F. Lee, "A discontinuous galerkin surface integral equation method for electromagnetic wave scattering from nonpenetrable targets," *IEEE Transactions on Antennas and Propagation*, vol. 61, no. 7, pp. 3617–3628, July 2013.
- [117] A. Buffa, G. Sangalli, and R. Vázquez, "Isogeometric methods for computational electromagnetics: B-spline and t-spline discretizations," *Journal of Computational Physics*, vol. 257, Part B, pp. 1291 1320, 2014.
- [118] Y. BAZILEVS, L. BEIRÃO DA VEIGA, J. A. COTTRELL, T. J. R. HUGHES, and G. SANGALLI, "Isogeometric analysis: Approximation, stability and error estimates for h-refined meshes," *Mathematical Models and Methods in Applied Sciences*, vol. 16, no. 07, pp. 1031–1090, 2006.
- [119] B. Juttler, A. Mantzaflaris, R. Perl, and M. Rumpf, "On numerical integration in isogeometric subdivision methods for pde on surfaces," *Computer Methods in Applied Mechanics and Engineering*, vol. 302, pp. 131 146, 2016.
- [120] M. Costabel, E. Darrigrand, and E. Kone, "Volume and surface integral equations for electromagnetic scattering by a dielectric body," *Journal of Computational and Applied Mathematics*, vol. 234, no. 6, pp. 1817–1825, 2010.
- [121] A. J. Poggio and E. K. Miller, Integral equation solutions of three-dimensional scattering problems. MB Assoc., 1970.
- [122] C. Müller, Foundations of the Mathematical Theory of Electromagnetic Waves. Springer-Verlag Berlin Heidelberg, 1969.
- [123] K. Cools, F. P. Andriulli, F. Olyslager, and E. Michielssen, "Time domain calderon identities and their application to the integral equation analysis of scattering by pec objects part i: Preconditioning," *IEEE Transactions on Antennas and Propagation*, vol. 57, no. 8, pp. 2352–2364, Aug 2009.
- [124] —, "Nullspaces of mfie and calderon preconditioned efie operators applied to toroidal surfaces," *IEEE Transactions on Antennas and Propagation*, vol. 57, no. 10, pp. 3205–3215, Oct 2009.
- [125] R. J. Adams, "Physical and analytical properties of a stabilized electric field integral equation," *IEEE Transactions on Antennas and Propagation*, vol. 52, no. 2, pp. 362–372, Feb 2004.
- [126] Z. G. Qian and W. C. Chew, "An augmented electric field integral equation for high-speed interconnect analysis," *Microwave and Optical Technology Letters*, vol. 50, no. 10, pp. 2658–2662, 2008.
- [127] J. Cheng, R. J. Adams, J. C. Young, and M. A. Khayat, "Augmented effe with normally constrained magnetic field and static charge extraction," *IEEE Transactions on Antennas and Propagation*, vol. 63, no. 11, pp. 4952–4963, 2015.

- [128] J. Li, X. Fu, and B. Shanker, "Formulation and Iso-geometric Analysis of Scalar Integral Equations for Electromagnetic Scattering," *IEEE Transactions on Antennas and Propagation*, submitted.
- [129] J. Cheng and R. J. Adams, "Electric Field-Based Surface Integral Constraints for Helmholtz Decompositions of the Current on a Conductor," *IEEE Transactions on Antennas and Propagation*, vol. 61, no. 9, pp. 4632–4640, Sep. 2013.
- [130] W. C. Chew, "Vector Potential Electromagnetics with Generalized Gauge for Inhomogeneous Media: Formulation," *Progress In Electromagnetics Research*, vol. 149, pp. 69–84, 2014.
- [131] Q. S. Liu, S. Sun, and W. C. Chew, "An integral equation method based on vector and scalar potential formulations," in 2015 IEEE International Symposium on Antennas and Propagation USNC/URSI National Radio Science Meeting, July 2015, pp. 744–745.
- [132] F. Vico, L. Greengard, and M. Ferrando, "Decoupled field integral equations for electromagnetic scattering from homogeneous penetrable obstacles," *arxiv*, Apr 2017.
- [133] R. F. Harrington, "Boundary integral formulations for homogeneous material bodies," Journal of Electromagnetic Waves and Applications, vol. 3, no. 1, pp. 1–15, 1989.
- [134] A. Stewart, "Role of the nonlocality of the vector potential in the aharonov-bohm effect," *Canadian Journal of Physics*, vol. 91, no. 5, pp. 373–377, 2013.
- [135] G. Trammel, "Aharonov-bohm paradox," *Physical Review*, vol. 134, no. 5B, p. B1183, 1964.
- [136] A. Burton and G. Miller, "The application of integral equation methods to the numerical solution of some exterior boundary-value problems," in *Proceedings of the Royal Society of London A: Mathematical, Physical and Engineering Sciences*, vol. 323, no. 1553. The Royal Society, 1971, pp. 201–210.
- [137] K. Chen, "An analysis of sparse approximate inverse preconditioners for boundary integral equations," SIAM Journal on Matrix Analysis and Applications, vol. 22, no. 4, pp. 1058–1078, 2001.
- [138] A. Bunse-Gerstner and I. Gutiérrez-Cañas, "A preconditioned gmres for complex dense linear systems from electromagnetic wave scattering problems," *Linear algebra and its applications*, vol. 416, no. 1, pp. 135–147, 2006.
- [139] B. Carpentieri, I. S. Duff, L. Giraud, and G. Sylvand, "Combining fast multipole techniques and an approximate inverse preconditioner for large electromagnetism calculations," *SIAM Journal on Scientific Computing*, vol. 27, no. 3, pp. 774–792, 2005.